Aerodynamic Interaction Effects Between a Propeller Slipstream and Flap Boundary Layer

A numerical study

J.C. Plijter

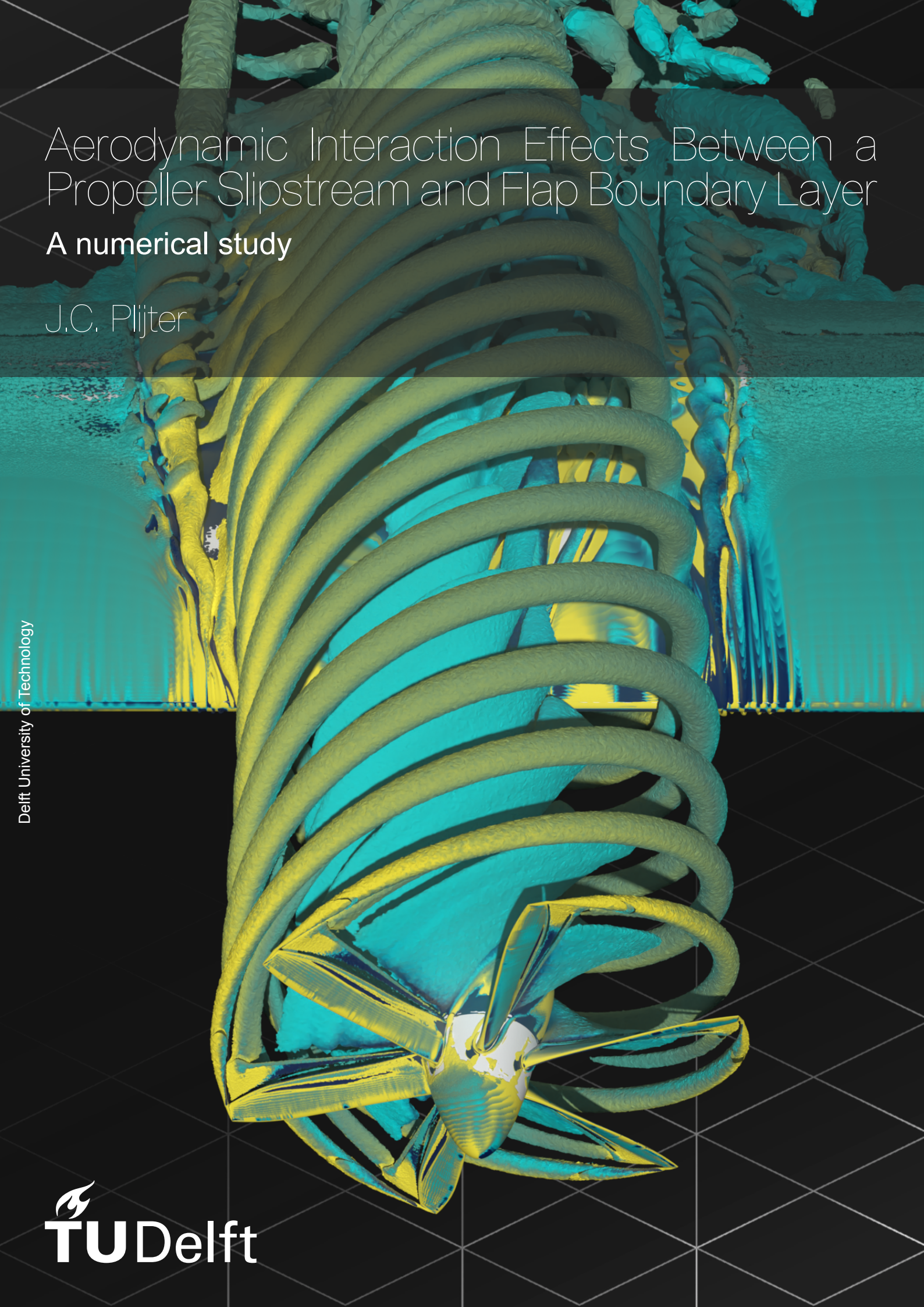

Delft University of Technology

TU Delft

This page intentionally left blank

Aerodynamic Interaction Effects Between a Propeller Slipstream and Flap Boundary Layer

A numerical study

by

J.C. Plijter

to obtain the degree of

Master of Science
in Aerospace Engineering at Delft University of Technology

to be defended publicly on December 22, 2023

Student Name:	Jurriën Christiaan Plijter
Student number:	4137345
Daily supervisor:	ir. R.R. Duivenvoorden, TU Delft
Responsible instructor:	dr. ir. T. Sinnige, TU Delft
Project Duration:	November 1, 2022 - December 22, 2023
Department:	Flight Performance and Propulsion, faculty of Aerospace Engineering, TU Delft

TU Delft

This page intentionally left blank

Preface

At the age of 14 I started flying among the dunes of Castricum, at a local glider club. During the same years I was also spending countless days tuning radio-controlled aircraft models. The combination of piloting and my fascination with its scientific aspects has consistently defined my professional journey so far. During my Bachelor's study, I spend my free days getting my PPL and in 2018, during my military helicopter pilot training in the USA, I followed online courses in aerospace engineering. It was that moment that my wife Chiara convinced me to look for a way to combine the full-time MSc. study Aerospace Engineering at TU Delft with my soon-to-be job at the military.

Thank you, Chiara, for your unconditional support - now and in the future -, the countless healthy meals you prepped if I was to busy to take care of my own, and for keeping me believe in myself.

Current thesis is the result of almost 4 years of hard work. When I started this study I would not have believed it if somebody told me I would be performing CFD simulations taking 100.000's of CPU hours. The resources provided by TU Delft for students are truly remarkable.
Thank you, Ramon, for your critical view of my work and for facilitating the flexible conditions for this thesis. Working on this thesis next to my work often led to planning concerns, but due to your open attitude this was never a reason for stress. Finally, we both did not really foresee up front the amount of computational resources required of current work. In that regard, I thank you for letting me go my own way on the TUD workstation and HPC, contacting your colleagues for their common CFD practices, and for the quick troubleshoots whenever the TUD workstation was once again misbehaving.

I don't think there are many other students who worked at their study at places ranging from Texas in the middle of summer heat up to crowded group shelters during a rainy military exercise in Germany. Yet this combination made the study so much fun. I will definitely miss it. (My colleagues might disagree... thanks all.)

J.C. Plijter
Delft, December 2023

This page intentionally left blank

Contents

Summary

Increased interest for aircraft with propeller propulsion has stimulated research in the aerodynamics of propeller-wing systems. One driven factor is the potential introduction of distributed electric propulsion (DEP) as it is shown to improve high-lift performance compared to conventional tractor propeller-wing-flap configurations. The complex flow dynamics involve the diffusing and deflecting propeller slipstream, coupled with the time-dependent interaction of the propeller wake with the main wing boundary layer, creating a time-varying flow field extending downstream to the flap region. As of today, not all flow phenomena that occur in a propeller-wing-flap system are fully understood. The research on flap flow, in particular, is often overlooked, while a thorough understanding of the flap flow field is required to further improve powered high-lift performance.

In current work an unsteady RANS simulation of a tractor propeller-wing-flap system is performed at high-lift, high propeller disk loading conditions in order to examine flap boundary layer characteristics under the influence of a propeller slipstream. The flow field of the high resolution hybrid grid of 190 million polyhedral cells is solved by using the Spalart-Allmaras turbulence model at an angle of attack of $8.3°$, fowler flap deflection angle of $15°$ and propeller advance ratio of 0.765, leading to a thrust coefficient T_c of 1.267. The chord based Reynolds number is 2 million.

Quantitative validation data of the full setup is very limited. Therefore a wing-flap setup is used to validate the CFD approach with Boermans experimental data. The nacelle-wing-flap and full propeller-wing-flap setups show good qualitative agreement with experimental results of Duivenvoorden.

First the propeller-nacelle-main wing flow field is discussed as interactions between its components shape the flow field that the flap experiences. The overall trend is a propeller slipstream shift to the propeller blade-down side at the wing upper surface, and opposite on the lower surface. Propeller tip vortices are seen to stretch around the wing leading edge, leading to slipstream divergence. A strong vortex system is identified above the surface of the wing suction side near the nacelle centerline, originating from the blade-up side propeller root sections. This vortex imposes a spanwise flow component to the blade-up side on the wing surface. From the slipstream-leading edge intersection additional vortices appear. These vortices are believed to accelerate flow separation just outside of the propeller slipstream affected area.
The spanwise lift distribution shows variations up to +/- 7.4% RMSE in lift, especially near the slipstream edges. In general, flow fluctuations on the pressure side (exceeding 100% C_p RMSE) exceed those on the wing suction side (≈ 10% Cp RMSE). This is attributed to the various vortex systems being in closer proximity to the pressure due to the high angle of attack.

It is proven that the overall flap surface flow field is dominated by the main wing pressure side flow field. Propeller tip vortex structures are not seen to reach the flap upper surface and vortices originating from the main wing leading edge pass well over it. They do approach close to the lower surface, maintaining high flow fluctuations at the flap pressure side. In general, the high momentum pressure-side slipstream flow improves flap stall characteristics. A small flow separation region however occurs near the nacelle centerline, reducing flap lift by an estimated 0.15%. This flow originates from a vortex system on the main wing pressure side. Viscosity in the vortex core reduces the local flow momentum, inducing flap flow separation. A large flow separation region occurs at the blade-down side slipstream edge of the flap and originates from the propeller slipstream edge. Near the separated flow region an inboard spanwise pressure gradient exists, next to the overall slipstream shift to the blade-up side. The vortex systems originating from the main wing suction side has several favorable effects on the flap, next to the high momentum flow of the propeller slipstream. However, the flap boundary layer still separates, underlining that the flap boundary layer is dominated by the main wing pressure side flow field and spanwise flow variations imposed by the slipstream deformation, affecting flap performance.

This page intentionally left blank

List of Figures

List of Tables

This page intentionally left blank

Nomenclature

Abbreviations

Abbreviation	Definition
AIAA	American Institute of Aeronautics and Astronautics
BEM	Blade element momentum
CBL	Confluent boundary layer
CFD	Computational Fluid Dynamics
DEP	Distributed Electric Propulsion
DES	Detached Eddy Simulation
EVM	Eddy Viscosity Model
LDV	Laser Doppler Velocimetry
LES	Large Eddy Simulation
PIV	Particle Image Velocimetry
PW	Propeller-Wing
PWF	Propeller-Wing-Flap
RPM	Revolutions Per Minute
RSM	Reynolds Stress Model
RST	Reynolds Stress Transport
S-A	Spalart-Allamaras
SGS	Sub-Grid Scale
SST	Shear Stress Transport
(U)RANS	(Unsteady) Reynolds Averaged Navier-Stokes
VLES	Very Large LES
WF	Wing-Flap
ZEF	Zone of Established Flow
ZFE	Zone of Flow Establishment

Symbols

Symbol	Definition		Unit
A	propeller disk area		[m^2]
C_D	wing drag coefficient		[-]
C_L	wing lift coefficient		[-]
C_T	propeller thrust coefficient	$C_T = T/(\rho n^2 {D_p}^4)$	[-]
C_d	airfoil drag coefficient		[-]
C_f	skin friction coefficient	$C_f = \tau_w/q_\infty$	[-]
C_l	airfoil lift coefficient		[-]
C_p	pressure coefficient	$C_p = (p - p_\infty)/q_\infty$	[-]
C_{p_t}	total pressure coefficient	$C_{p_t} = (p_t - p_\infty)/q_\infty$	[-]
D	drag		[N]
D_n	nacelle diameter		[m]
D_p	propeller diameter		[m]
J	propeller advance ratio	$J = U_\infty/(n \cdot D_P)$	[-]
L	lift		[N]
M	mach number		[-]
R	propeller tip radius		[m]

Symbol	Definition		Unit
R_p	propeller radius		[m]
R_s	slipstream radius		[m]
Re	Reynolds number		[-]
T	thrust		[N]
T_C	propeller thrust coefficient	$T_C = T/(0.5\rho U_\infty^2 A)$	[-]
U	velocity		[m/s]
U_∞	freestream velocity		[m/s]
$\bar{U}$	mean velocity		[m/s]
U'	RMSE of velocity		[m/s]
a	axial induction factor		[-]
a'	tangential induction factor		[-]
b	wing span		[-]
c	wing chord		[m]
h	helicity		[m/s^2]
h_n	normalized helicity		[-]
l	length		[m]
$\dot{m}$	massflow		[kg/s]
n	revolutions per second		[1/s]
p	static pressure		[Pa]
p_t	total pressure		[Pa]
p_∞	freestream static pressure		[Pa]
q	dynamic pressure	$q = 0.5\rho_\infty U_\infty^2$	[Pa]
q_∞	freestream dynamic pressure		[Pa]
r	propeller blade radial position		[m]
r_n	nacelle radius		[m]
r_p	propeller radius		[m]
t	time		[s]
$\bar{u}$	mean flow solution		[-]
u'	flow fluctuation		[-]
v_a	local blade axial velocity		[m/s]
v_t	local blade tangential velocity		[m/s]
v_t	eddy viscosity factor		[-]
y^+	non-dimensional distance		[-]
Δ	LES filter size		[-]
Ω	propeller rotational velocity		[rad/s]
α	angle of attack		[deg]
β	pitch angle		[deg]
δ	boundary layer thickness		[m]
δ_f	flap deflection angle		[deg]
δ_s	slat deflection angle		[deg]
$\lambda 2$	Lambda-2 criterion		[-]
μ	viscosity		[Pa]
μ_t	turbulence viscosity		[Pa]
ρ	density		[kg/m^3]
τ	Reynolds stresses		[-]
τ_c	LES time scale		[-]
τ_w	wall shear stress		[Pa]
ϕ	inflow angle		[deg]
ω	vorticity		[1/s]

1

Introduction

Renewed interest in propeller-driven aircraft has boosted research in propeller-wing aerodynamics. Not only are turboprop aircraft expected to increase in number due to the increasing demand for short-range aircraft and their higher propulsive efficiency compared to turbofan engines for the short-range mission profile [21], also the potential introduction of distributed electric propulsion (DEP) has led to increased interest in better understanding the aerodynamic interactions of propeller, nacelle, wing, and flap systems. In a DEP system, multiple electrical driven propellers are placed along the aircraft wing span. Current DEP projects are, for example, the NASA LEAPtech (Leading Edge Asynchronous Propeller Technology) aircraft [22], and Airbus SynergIE aircraft in cooperation with DLR shown in Figure 1.1 [1].

An advantage of DEP is its ability to improve high-lift capabilities compared to a wing with a single propeller. A recent example that demonstrates the high-lift potential of a DEP system is the research of Keller et al. [2], who performed CFD simulations of a propeller aircraft in which 12 adjacent propellers are placed along the wing span (see Figure 1.1). The high lift potential is clearly illustrated by the upward shift of the lift curve when comparing the 2-prop configuration with the 12-prop configuration in Figure 1.2.

Figure 1.1: Top:Conventional 2-propeller aircraft. **Bottom**: SynergIE DEP-12 preliminary aircraft design [1]

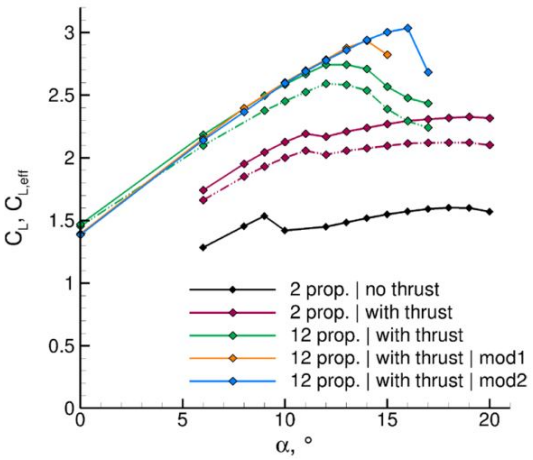

Figure 1.2: Comparison of lift curves of 2-propeller aircraft versus a 12-propeller setup. Solid lines ($C_{L,eff}$) includes lift-forces of propeller, while dashed lines (C_L) only consider nacelle and wing lift forces. [2]

While the results of Keller look promising, as of today, not all flow phenomena that occur in a propeller-wing-flap system are fully understood. However, a thorough understanding of the flap flow field is

required to further improve powered high-lift performance, as explicitly stated by DLR [23]. High-lift conditions occur at both take-off and landing, the latter in case of a go-around of an aircraft in which full thrust is applied while flaps are still configured for landing.

Previous experiments by Duivenvoorden [10] show a complex flow field at the flap of the experimental propeller-wing-flap setup, but the corresponding results alone do not lend themselves for a conclusive statement on the origin of observed flap flow phenomena. In fact, most publications that add a flap to a propeller-wing setup spare little attention to the flap flow but rather discuss overall high-lift performance, such as the research of Roosenboom [12,24,25]. And although propeller-wing-flap CFD results of Bongen [26] show good qualitative agreement with experimental measurements, the employed actuator disk approach is unable to resolve the inherent unsteadiness of the slipstream. Bölk [27] however chose to model the full propeller geometry and apply an unsteady RANS approach instead to identify the time-dependent position of flow separation of an over-the-wing PWF setup with success, but a similar approach to identify unsteady flap flow stall characteristics for a conventional tractor configuration was not found in literature.

The objective of the current study is to provide insight into unsteady flap flow phenomena within the boundary layer of a slotted flap, subjected to a propeller slipstream at high-lift and high propeller disk loading conditions by performing an unsteady RANS simulation of a 2.5D propeller-wing-flap system.

This report is structured as follows: the theoretical background and current state-of-the art of propeller-wing-flap aerodynamics is further elaborated upon in Chapter 2. Computational methods of propeller-wing-flap simulations and CFD turbulence modelling are briefly reviewed in Chapter 3. An interim conclusion is given in Chapter 4. Based on the identified knowledge-gap, Chapter 5 presents the research question of this thesis. Chapters 6 and 7 present the set-up, verification and validation respectively of the chosen unsteady RANS CFD approach with Spalart-Allmaras turbulence model to research propeller-wing-flap aerodynamic interaction effects, after which the results are presented in Chapter 9. This report is finalized with a conclusion and recommendations in Chapter 10.

Part I

Background

2

Review of Propeller-Wing-Flap Aerodynamics

To research propeller-wing-flap (PWF) aerodynamics in tractor configuration first the subparts of such a system must be fully understood due to mutual interaction effects. A logical division is to start with an overview of theory, wind tunnel experiments and CFD simulations on wing-flap aerodynamics in Section 2.1, followed by isolated propeller aerodynamics in Section 2.2. Next, the mutual aerodynamic interaction between a propeller and wing is discussed in Section 2.3. The endpoint of this chapter is to present an overview of flow phenomena of a PWF system in Section 2.4.

2.1. Wing-flap aerodynamics

The concept of increasing lift by flaps as a separate airfoil, attached with a hinge to the main airfoil, aiming to increase the wing camber and/or chord, has been subject of research as early as 1914 when the British Advisory Committee for Aeronautics (1909-1979) performed experiments on *'Aerofoil having a hinged rear portion'* [28]. In 1953 one of the first extensive theoretical reports explaining flap aerodynamics was published by Young [29], already effectively discussing the performance of multiple flap designs still seen in current operational aircraft. In 1975 Smith published his paper "High-Lift Aerodynamics" [3]. Smith identified 5 main effects to explain the 2D interaction of multi-element airfoils:

1. **Slat effect** By simulating the slat as a vortex and considering the main wing leading edge, the induced slat vortex velocities are opposite to the induced velocities of the main element vortex. This reduces the main wing pressure peak and protects for leading edge stall while also reducing the adverse pressure gradient which in turn delays trailing edge stall. As a result the main wing lift coefficient reduces but this is compensated for by the slat vortex. The total lift coefficient therefor increases.

2. **Circulation effect** Apply the same principle as the slat effect, but now place a vortex at the flap location. This vortex now increases the main wing circulation, increasing main wing lift coefficient and total lift coefficient.

   More general, one should use the terms 'upstream element' and 'downstream element'. The circulation effect can also be applied to the main wing and slat: the main wing (downstream element), enhances the circulation of the slat (the upstream element). The origin of the slat and circulation effect is illustrated in Figure 2.1.

3. **Dumping effect** The vortex of a downstream element increases tangential velocities of an upstream element. For example when considering a main wing with a single flap: the main wing boundary layer at the main wing trailing edge is 'dumped' in a region of velocity higher than freestream velocity. This is favorable for the boundary layer, as it relieves the pressure rise In

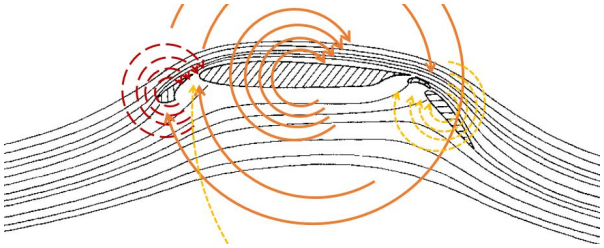

Figure 2.1: Illustration of slat effect and circulation effect.
Black indicates streamlines, red indicates slat circulation, orange indicates main element circulation, yellow indicates flap circulation. [3] (edited)

.

the boundary layer and mitigates separation.

4. **Off-the-surface pressure recovery** Consider the attached boundary layer of the main wing element. At some point there shall be a pressure recovery to ambient conditions. The flap prevents ambient conditions at the main wing element trailing edge. After separation at the trailing edge, this pressure recovery continues in the wake of the main wing element. The deceleration of the wake continues off the surface. Wakes can withstand a higher adverse pressure gradient compared to surface-attached boundary layers, and thus the risk of flow reversal in the wake is reduced. With this in mind, one can conclude that multi-element airfoils can realize lower velocity ratios, hence much lower leading edge pressure coefficients, compared to single-element airfoils, because of the off-the-surface flow deceleration.

5. **Fresh-boundary-layer effect** The fact that each element starts with a new boundary layer results in thinner boundary layers when comparing a single element airfoil with a multi-element airfoil of the same total length. Thinner boundary layers can withstand higher adverse pressure according to Stratford's separation criterium, which assesses if a turbulent boundary layer is prone to separation [30]. Yet the boundary layers of individual elements can merge together downstream, called a confluent boundary-layer (CBL), which reduces maximum lift because of early separation due to the thicker boundary layer when compared to the boundary layer thickness of the main element alone.

A large flap deflection might cause wake bursting [3], i.e. off-the-surface separation while flow on the element surface is still attached. Wake bursting is the result of a strong adverse pressure gradient in the wake, e.g. due to a large flap deflection angle which forces the wake of the main element to thicken. Wake bursting increases drag and reduces the maximum lift coefficient and can be predicted by Gartshore's criterion [3, 31, 32].

The slat and circulation effects can be clearly identified in common 2D chordwise pressure distribution graphs by noting suppression or increasing of the corresponding element suction peak in both CFD and wind tunnel experiments (e.g. [3]), while effects that involve the boundary layer require high-resolution experimental measurements in a 2D plane or a high-resolution CFD grid with an appropriate turbulence model.

2.2. Propeller aerodynamics

The propeller imposes a total pressure jump at the propeller disk plane. The corresponding axial flow acceleration can be expressed by an axial induction factor. Thrust is the forward component of the resultant aerodynamic forces on the blades. Vice versa can the effect of the torque that the propeller imposes on the flow, resulting in propeller swirl as shown in Figure 2.2a, be expressed by a tangential induction factor. Both induction factors depend on the radial position of the considered blade element. When considering a blade of a propeller as a rotating wing one can identify the following velocities, angles and forces at a blade element of the propeller in Figure 2.2b:

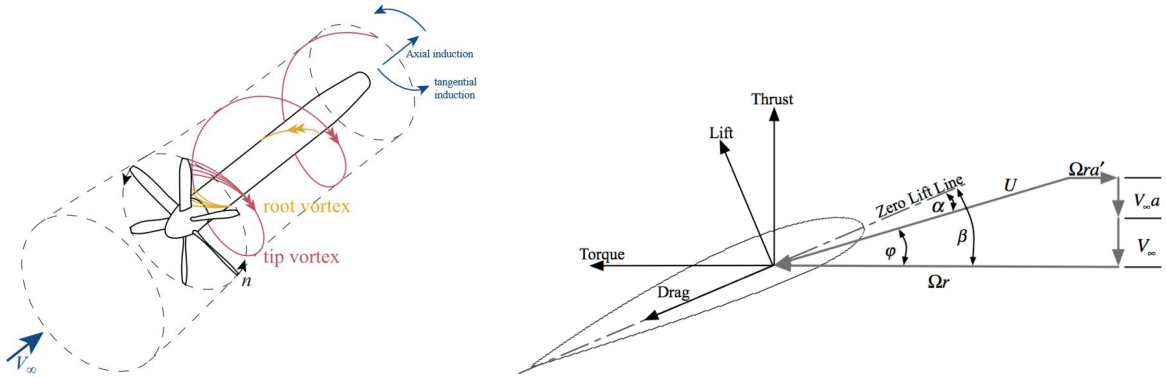

(a) Propeller streamtube and vortex system [33] (edited)

(b) Velocity diagram of a blade element [34]

Figure 2.2: The propeller system and blade element definitions.

In which V_∞ is the freestream velocity. This is added with a term $V_\infty a$ in which a is the axial induction factor due to axial induced velocity. The total tangential velocity consists of the local velocity due to blade rotation Ωr subtracted with a component $\Omega r a'$ in which a' is the tangential induction factor due to tangential induced velocity. The effective velocity U is the velocity the blade element experiences. ϕ is the blade inflow angle, α the local angle of attack and β the pitch angle.

2.2.1. Flow quantities of a propeller slipstream

The often cited work of Veldhuis [5] presents an excellent overview of propeller and slipstream aerodynamics. Veldhuis identified 7 flow quantities to describe the propeller slipstream:

1. Axial velocity profile
2. Swirl velocity profile
3. Total pressure distribution
4. Static pressure distribution
5. Vorticity
6. Helicity
7. Contraction

Axial and swirl velocity profiles

The origin of the axial induction factor can be simply derived from Rankine's basic actuator disk theory when considering the continuity, momentum and energy equations applied to assumed steady, inviscid, incompressible and constant internal energy flow. The thrust T is generated by a pressure jump over the propeller (actuator) disk: $T = A\Delta p$, in which A is the disk area. At the same time, according to conservation of linear momentum for steady flow, the thrust generated by the actuator disk can also be calculated as $T = \dot{m}(V_{up} - V_{down})$, in which $\dot{m}$ is the air mass flow and V_{up} and V_{down} indicate the air velocity far upstream and far downstream of the actuator disk. Hence, to generate thrust, air must be accelerated and the air velocity at the actuator disk is $V_{disk} = (V_{up} - V_{down})/2 = V_\infty(1 + a)$, and $V_{up} = V_\infty$ and $V_{down} = V_\infty(1+2a)$ which also implies streamtube contraction in downstream correction to adhere to conservation of mass; e.g. $(\rho V A)_{up} = (\rho V A)_{down}$ as also sketched in Figure 2.2a.
The classical actuator disk theory of Rankine only considers flow in the axial direction and is therefore not able to explain the tangential induction factor a'. For this the Prandtl lifting-line model,1918, is considered. An operating propeller will shed a helical vortex sheet. Based on this model and taking into account the influence of all vortex segments, it is possible to calculate the influence of each vortex on the blade from which the axial, tangential but also the radial induced velocities are derived, although the latter are often neglected. From the orientation of the vortices the tangential induced velocity is in the direction of the blade movement as shown in Figure 2.2b by the term $\Omega r a'$. An example of the radial distribution of the axial and tangential velocities is shown in Figure 2.3a, although this heavily depends on the blade design.

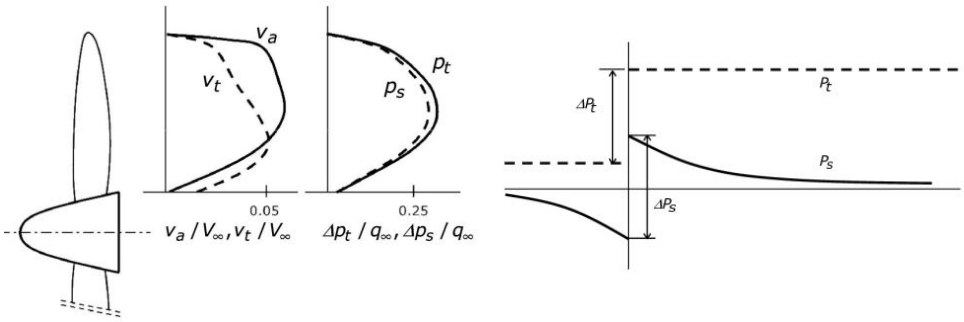

(a) Radial distribution of axial v_a and tangential velocities v_t (left) and total P_t and static pressure P_s (right) directly behind lightly loaded propeller [5]

(b) Streamwise pressure development [5]

Figure 2.3: Radial and streamwise propeller flow properties

Total and static pressure distributions

The static pressure reduces in front of the propeller disk due to the already contracting slipstream. At the disk the static pressure suddenly increases above the freestream static pressure, after which it reduces again to the freestream value. The total pressure is constant in front of the disk. At the disk the total pressure increases and remains constant behind the disk. Figure 2.3a shows that the increase in total pressure exceeds the increase in static pressure due to *"the rotational motion imparted to the slipstream by the reaction of the torque"*. The derivation can be found in Veldhuis his Ph.D. disseration and concludes to $p - p_{t_\infty} = \Delta p + \frac{1}{2}\rho {v_t}^2$, in which $v_t = f(r)$.

Vorticity and helicity

Vorticity ω is the curl of the flowfield: $\vec{\omega} = \nabla \times \vec{V} = (\omega_x, \omega_y, \omega_z)$. Each blade sheds a continues vortex sheet. The radial distribution of the vorticity depends on the spanwise loading distribution, including the effect of blade position when a nonuniform flowfield is considered. Just like steady wings, vorticity is mainly created at the blade tips and root sections; regions with a high spanwise loading distribution gradient. The vorticity in streamwise direction, ω_x, can be considered symmetrical in the rotating axis thus independent of azimuth angle of the respective blade, while ω_y and ω_z are not symmetrical. One way to visualize vorticity is by applying the concept of helicity.

The application of helicity for external aerodynamics analysis has been introduced in 1990 by Levy et al. [35] as a tool to visualize concentrated vortices with the increasing computational power at the time Levy et al. describe the added value of helicity to *"emphasize the complex parts of the flowfield, identify the vortices, differentiate between primary and secondary vortices, indicate the sense of the swirling motion, locate singular points in the flow, and trace the vortex-core streamlines that emanate from them"*. The normalized helicity is defined as:

$$h_n = \frac{\omega \cdot V}{|\omega|\,|V|} \tag{2.1}$$

which implies that if $h_n = 1$ the vorticity vector is aligned with the velocity vector and thus indicative for a vortex core. The application of helicity to identify vortex cores is rather limited in current literature. More often used are the Q- and $\lambda 2$-criterion's. The Q-criterion quantifies the local rotation and strain rates, and regions with positive Q-values indicate vortical structures. The $\lambda 2$ criterion assesses the second-largest eigenvalue of the velocity gradient tensor, and regions where $\lambda 2$ is negative indicate the presence of vortices. An overview of both methods is provided by Liu et al. [36].

Contraction

From the conservation of mass and increased velocities due to the propeller it follows that the streamtube should contract to preserve the mass flow. Veldhuis derived a rather simple expression of the slipstream contraction ratio when considering a propeller-only setup (excluding the nacelle) by assuming inviscid and incompressible flow and the assumptions that the axial components dominate the slipstream geometry and a constant axial force over the propeller disk, shown in eq. 2.2:

$$\frac{R_s(x)}{R} = \sqrt{\frac{1+a}{1+a(1+\frac{x}{\sqrt{R^2+x^2}})}} \tag{2.2}$$

in which the axial induction factor is defined as $a = v_a/V_\infty$, R the propeller radius and $R_s(x)$ the radius of the slipstream at longitudinal position x. This equation predicts a final contraction ratio of $R_s(x)/R = 0.95$ but does not include diffusion and hence expansion of the slipstream in the far-field downstream region of the propeller plane. The actual slipstream development of an isolated propeller is shown in Figure 2.4, in which the Efflux plane, indicating the transition from slipstream contraction to expansion, is located at $x_0/D_p = 0.764$, based on wind-tunnel experiments on UAV propellers [4]. In that case, especially for small propellers as in DEP systems, flaps are subjected to an expanding slipstream while the main wing leading edge experiences a contracting slipstream.

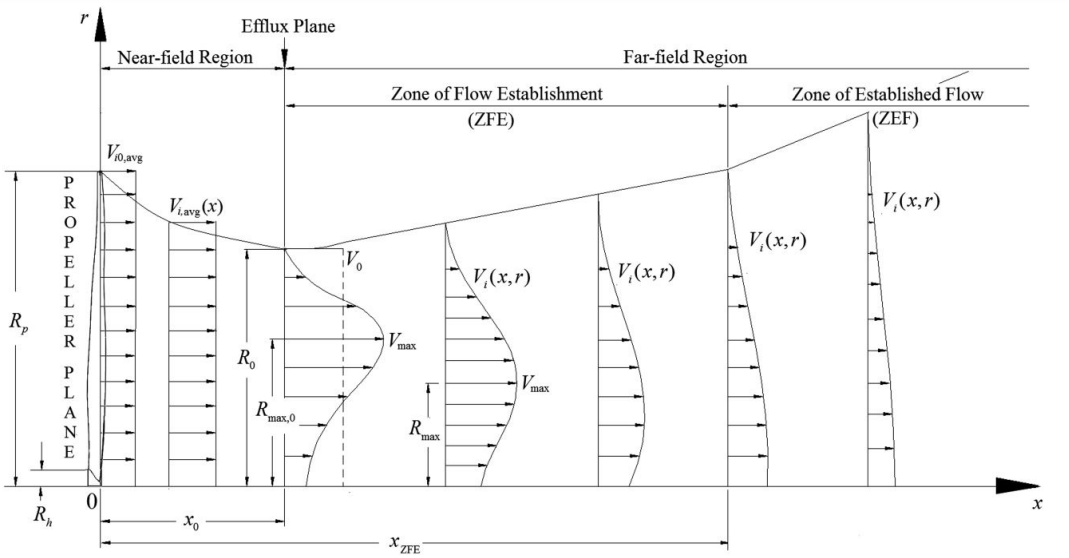

Figure 2.4: Propeller slipstream model showing near-field, far-field and efflux plane. Isolated propeller only. [4]

It is clear that the 7 flow quantities of Veldhuis can not be seen as independent flow properties. To analyse propeller aerodynamics one should determine the vortex shedding of the propeller blade. The quantity helicity is nothing more than a mathematical property; a tool to visualize the vortex cores. The induced velocities of the vortex system gives the axial and swirl velocity profiles, followed by the total and static pressure distributions and contracting slipstream due to the conservation of mass.

Himmelskamp effect

The Himmelskamp effect [37] causes stall delay due to rotational effects, enhancing lift. The boundary layer of a propeller blade is influenced by centrifugal forces, pushing the boundary layer outboard towards the tip. The resulting Coriolis force pulls the boundary layer to the trailing edge, in fact acting as a favorable pressure gradient. The boundary layer of a rotating blade can therefore withstand higher adverse pressure gradients and separation occurs more aft of the airfoil section compared to steady blades. The work of Goyal [38] shows a propeller RANS CFD simulation in which the Himmelskamp effect can be clearly identified.

2.2.2. Propeller in non-uniform flow field

All propeller blades encounter the same conditions, independent on the azimuthal position, if the propeller operates at zero angle of attack, leading to axis-symmetric blade loading. A propeller subject to a non-uniform flow field, e.g. due to a slip angle β, incidence angle or angle of attack α, will experience an azimuthal variation of inflow conditions and thus blade loading.

For example, consider the propeller disk subject to an incidence angle. The down going blade experiences a larger increase in angle of attack than the reduction of angle of attack for the up going blade

as shown in Figure 2.5, resulting in increased thrust compared to no incidence angle [5, 39]. This will also lead to unsteady blade loading and in-plane forces and moments. These and other propeller-wing interaction effects will be discussed in Section 2.3 next.

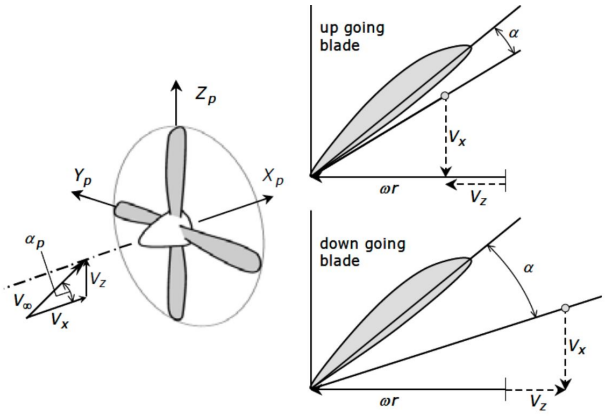

Figure 2.5: Blade angle of attack variation due to propeller incidence angle [5]

2.3. Propeller-wing interaction

This section will discuss the interaction between the propeller and the wing. Many effects in this interaction are due to interacting individual vortex systems, as such most significant phenomena can be explained by superimposing the induced velocities from respective vortex systems. Still, also boundary layer interactions take place, for example due to the nacelle and propeller tip vortex interaction with the wing boundary layer.

2.3.1. Effects of the nacelle

The interaction of the propeller vortices with the nacelle leads to an underestimation of the earlier discussed contraction ratio of the propeller slipstream (eq. 2.2) [5]. This is also due to the blockage effect of the nacelle, which imposes a non-uniform axial velocity increase leading to a further contraction of the slipstream.

The nacelle-wing junction is susceptible for early separation, because of the merging of the boundary layers of the wing and nacelle, resulting in a thicker and more separation-sensitive boundary layer [10]. At the same time, flow directly behind the nacelle is less likely to separate due to a high pressure region as the nacelle covers the leading edge [6, 10]. This also leads to a steep spanwise pressure gradient. Air in the high pressure region behind the nacelle will tend to extend in spanwise direction, resulting in a divergent flow from the nacelle up to the trailing edge at the wing suction side [10]. This divergent flow also leads to boundary-layer accumulation and low-energy air infusion at the wing itself [6], making wing area's outside of the divergent flow more susceptible for wing stall and reducing the stall angle of attack of the nacelle-wing configuration compared to a wing-only setup.

A last effect is the susceptibility of flow reversal at the leading edge near the nacelle-wing intersection due to a locally increased angle of attack. The effects of the nacelle are illustrated in Figures 2.6 and 2.8 by means of CFD simulations and in Figure 2.7 in an experimental setting.

2.3.2. Effects of the wing on the propeller

The wing induces an upwash at the propeller disk, which is particularly important in this report as the upwash is strongest at high-lift conditions due to the increased circulation at such a condition. In that case the propeller operates in a non-uniform flowfield due to the upwash imposed incidence angle.

Another important effect is the reduction of rotational velocity in the slipstream due to the wing, known as swirl reduction [5, 40]. This is also known as swirl recovery, as the presence of the wing itself 'recovers' some of the otherwise lost swirl energy by an additional thrust component. The upwash of the upgoing

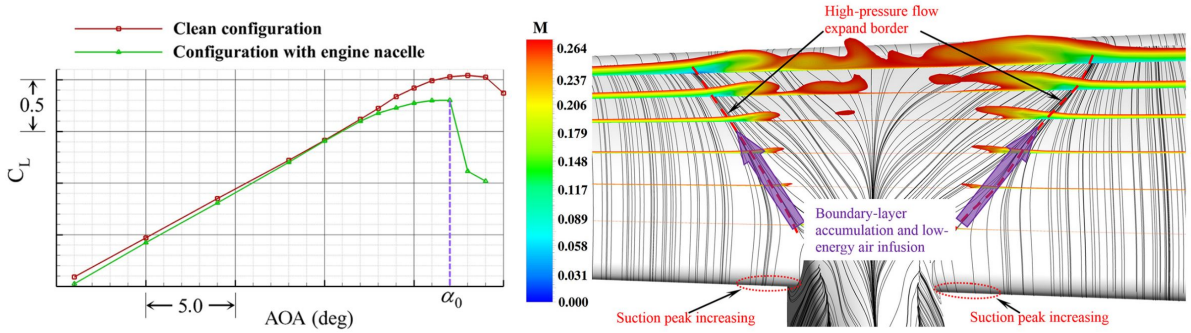

(a) Lift polar of wing-only versus nacelle-wing configuration

(b) Unfavorable effects of nacelle-wing interaction

Figure 2.6: Illustration and effects of unpowered nacelle-wing interaction by CFD at $\alpha_0 = 17°$. [6]

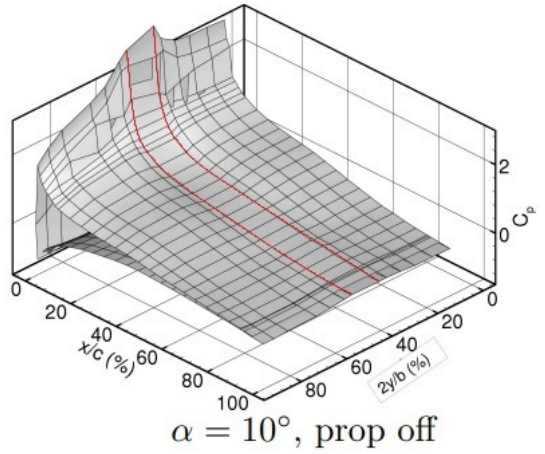

Figure 2.7: Influence of nacelle on surface pressure distribution of PROWIM wind tunnel model. Propeller off condition. The nacelle is positioned between the red lines. [5] (edited)

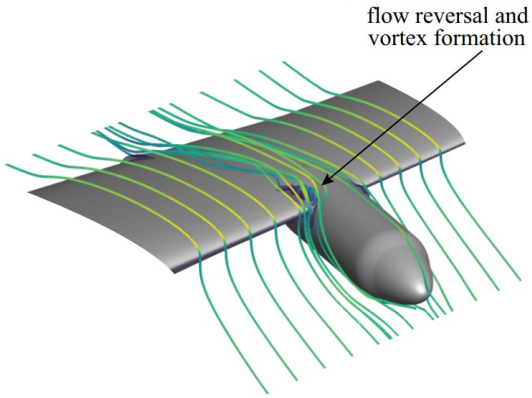

Figure 2.8: Velocity streamlines near nacelle-wing intersection, prop-off, $\alpha = 6°$ [7]

blade increases local angle of attack, resulting in additional lift and leading edge suction, the latter is in fact 'negative drag' or an extra thrust component. Also at the downgoing blade a 'negative drag' or extra thrust exists, although now with negative lift. Concluding, the presence of the wing counteracts the thrust losses due to the propeller rotational flow, which does not add to the thrust contribution when considering the isolated propeller.

2.3.3. Effects of the propeller on the wing

The increase in axial velocity due to the propeller leads to an increase in dynamic pressure thus an increase in local lift forces of the wing portion subjected to the propeller slipstream. This effect is symmetrical in the propeller centerline, while the effects due to the induced tangential velocities are not. The upgoing blade of the propeller increases the local wing angle of attack; the downgoing blade reduces the local wing angle of attack. Therefore the direction of rotation of the propeller dominates the spanwise wing loading distribution [5].

The loading distribution due to axial and tangential induced velocities does not only influence the loading of the wing parts that are located into the contracted propeller slipstream. Outside these regions the wing is also affected due to the *"distorted vorticity sheet that leaves the wing"* according to Veldhuis, as shown in Figure 2.9. I.e., whereas the propeller slipstream delays wing stall for wing portions inside the propeller slipstream [10, 41], parts of the wing outside the propeller slipstream are more sensitive for flow separation when compared to a wing-only configuration.

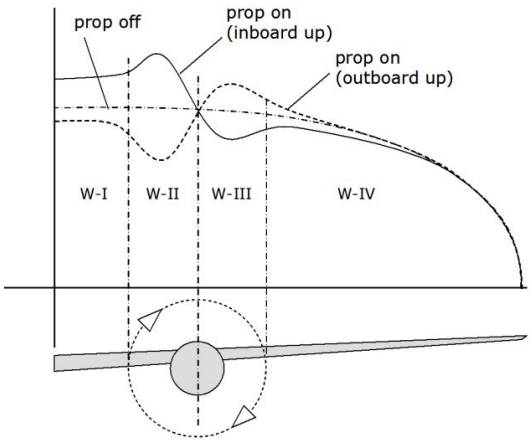

Figure 2.9: Spanwise lift distribution due to propeller effects [5]

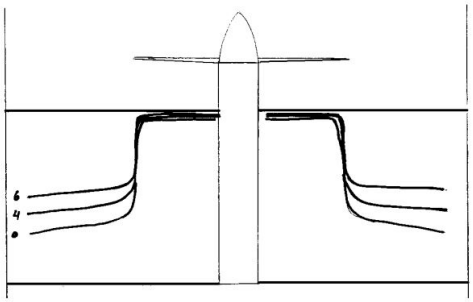

Figure 2.10: Experimental based positions of boundary layer transition [8]

The interaction of propeller tip vortices with the main wing lead to chordwise misalignment and spanwise shear i.e. misalignment of the propeller tip vortices:

Chordwise misalignment is the result of the propeller tip vortex being split at the wing leading edge, after which both halves of the original vortex continue with the local velocity vector. Therefor the upper vortex half will reach the trailing edge prior to the lower half as visualized by Johnston and Sullivan [9].

Spanwise shear increases in severity with angle of attack and can be explained by 1) considering an image vortex and 2) the spanwise wing circulation gradient. The latter explanation is explained by the illustration in Figure 2.11. Consider the spanwise circulation distribution due to the wing and slipstream. The edges of the slipstream indicate a high spanwise loading gradient. By simulating this gradient with discrete vortices, one can see that the slipstream upper and lower halves shift in opposite ways. Johnston [9], Veldhuis [5] and Suard [42] present several wake measurements from propeller-wing experiments in which this effect is clearly seen.

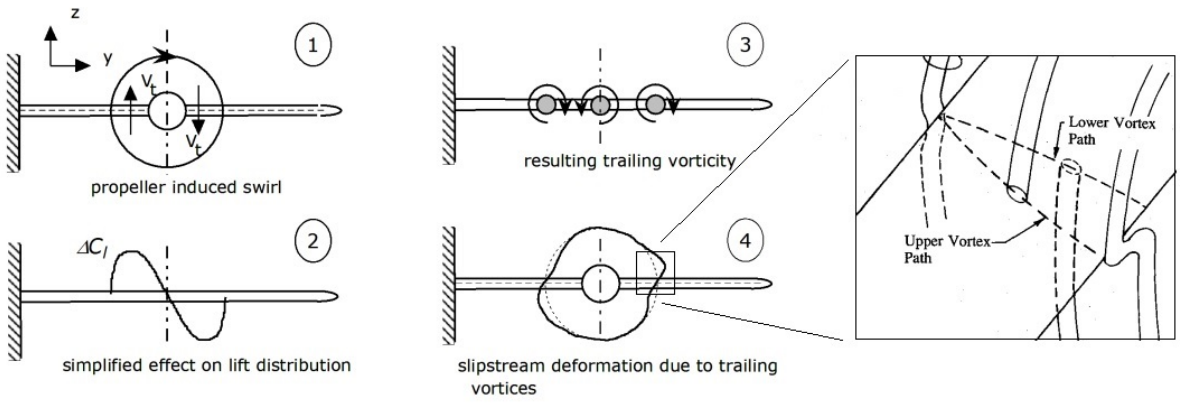

Figure 2.11: The origin of spanwise shear or misalignment of the propeller slipstream [5, 9]

The increase in angle of attack and corresponding lift coefficient at the upgoing propeller blade side leads to more upstream separation when compared to a propeller-off condition, as shown in Figure 2.12 of the experimental PWF setup of Duivenvoorden [10].

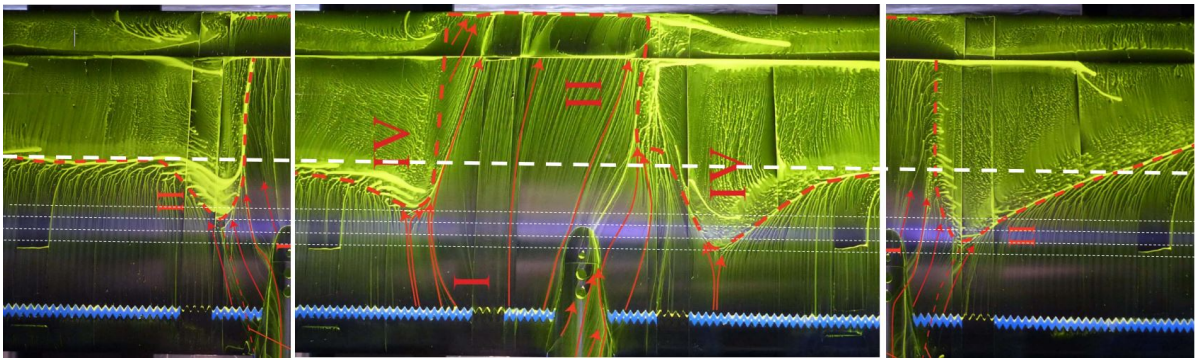

downgoing side upgoing side

Figure 2.12: Comparison of nacelle-wing setup (left and right) with propeller-wing setup (middle). Dashed white lines are reference lines to compare flow separation locations between the two setups. Flap retracted. Propeller advance ratio $J = 0.8$. Wing suction side. $\alpha = 13°$. Edited from Duivenvoorden. [10]

CFD [11,42,43] and wind tunnel experiments [10] of propeller-wing setups also reveal surface flow that moves in opposite direction of the propeller rotation, originating from both the propeller root vortices and the nacelle itself [42]. This flow is clearly visible in Figure 2.13

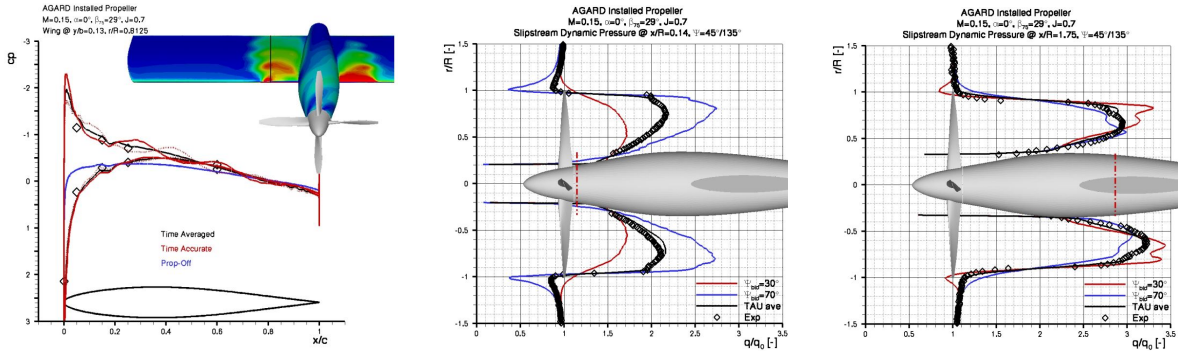

(a) Wing pressure distribution.

(b) Dynamic pressure profiles at $x/R = 0.14$.

(c) Dynamic pressure profiles at $x/R = 1.75$.

Figure 2.13: URANS CFD results of Stuermer et al. [11]

A final effect of the propeller on the wing is the interaction of the unsteady periodic flow originating from the propeller due to the finite number of blades with the wing boundary layer and impingement of turbulent values from the propeller on the wing [5]. Therefore one might expect a constant fully turbulent wing boundary layer due to the fluctuations of the slipstream flow that impose the main wing boundary layer, while in practice it cycles between laminar and turbulent with the blade passing frequency [5]. Other experiments show a full turbulent boundary in the propeller slipstream as sketched in Figure 2.10. Based on the assessed literature it is unclear when the cyclic transition may occur in a wing-flap setup. However, when considering a propeller-wing-flap setup, it is unlikely that the wing boundary layer will cycle as the flap increases the adverse pressure gradient, accelerating transition [44].

2.4. Propeller-wing-flap interaction

The mutual interaction of the 3-part propeller-wing-flap system implies a total of 6-way interactions occurring. Instead of discussing each of these 6 interactions individually, a more overarching approach will be applied in this section. How the addition of a flap to a propeller-wing system influences aforementioned effects of nacelle-wing interaction, slipstream contraction and expansion and boundary layer behavior will be discussed, including how these changes in turn affect the flap flow.

2.4.1. Nacelle-wing-flap interaction

One of the five main effects of high-lift systems is the increase in circulation of the main wing by a flap element as discussed in section 2.1. This further intensifies the divergent flow pattern and spanwise

pressure gradient on the main wing suction side (as earlier shown in Section 2.3.1, Figure 2.6) due to the engine nacelle as shown in Figure 2.14a [10]. Furthermore, vortices can be shed from the nacelle due to separation at high angles of attack. These vortices are facing a high adverse pressure gradient at the main wing and flap during high-lift conditions. The mixing of the low energetic boundary layer near the main wing trailing edge with the nacelle vortices that have experienced significant total pressure losses reduce the flap suction peak or trigger flow separation; hence reducing total propeller-wing-flap lift performance [42, 45].

2.4.2. Flap flow under influence of a propeller slipstream

The combination of a propeller and flap deflect the propeller slipstream, adding an additional lift component in addition to *"lift augmentation"* due to the increased mass flow in the propeller slipstream [46]. The diffusing and deflecting flow of the propeller slipstream and time-dependent interaction of the propeller wake with the main wing boundary layer translates downstream to the flap region. Interaction between the flap flow and mentioned effects can occur in case of confluent boundary layer flow, resulting in a complex flow field. The next paragraphs will discuss the current state of propeller-wing-flap interaction by the publications of Duivenvoorden [10] and Roosenboom [12]. Many other experimental-based publications on propeller-wing-flap setups exist, but those are limited for the use of research on propeller-wing-flap flow structures as they focus on mapping performance coefficients instead of explaining the visualized flow (e.g. [47, 48]), or only contain limited data to explain observed flow phenomena (e.g. [49, 50]).

The earlier mentioned publication of Duivenvoorden [10] includes oil flow visualizations of a propeller-wing-flap system at an angle of attack of $8°$, advance ratio of 0.8 and flap deflection of $30°$. The visualizations are shown in Figures 2.14b and 2.14c. Figure 2.14a shows the flow of a non-propeller nacelle-wing-flap setup, showing an almost full-spanwise laminar separation bubble near the flap leading edge. This bubble has disappeared in section (VII) of Figure 2.14b due to the turbulent propeller slipstream. A quantitative comparison is however difficult due to the difference in angle of attack. The spanwise shear as discussed earlier by Figure 2.11 is clearly visible: the propeller slipstream tends to diverge at the down going blade side, while the slipstream on the upgoing blade side converges to the propeller centerline. Also note, as observed by Duivenvoorden, the offset between section (VII) with the slipstream area of the main wing due to the propeller slipstream path at the main wing pressure side. Sections (V) show signs of being influenced by vortical structures, possibly origination from propeller tip, root and nacelle vortex shedding, but this could not be confirmed on this experimental data alone. Duivenvoorden has performed numerous numerical preliminary simulations to verify the origins of significant flow phenemona. Unfortunately no further details about those simulations are known.

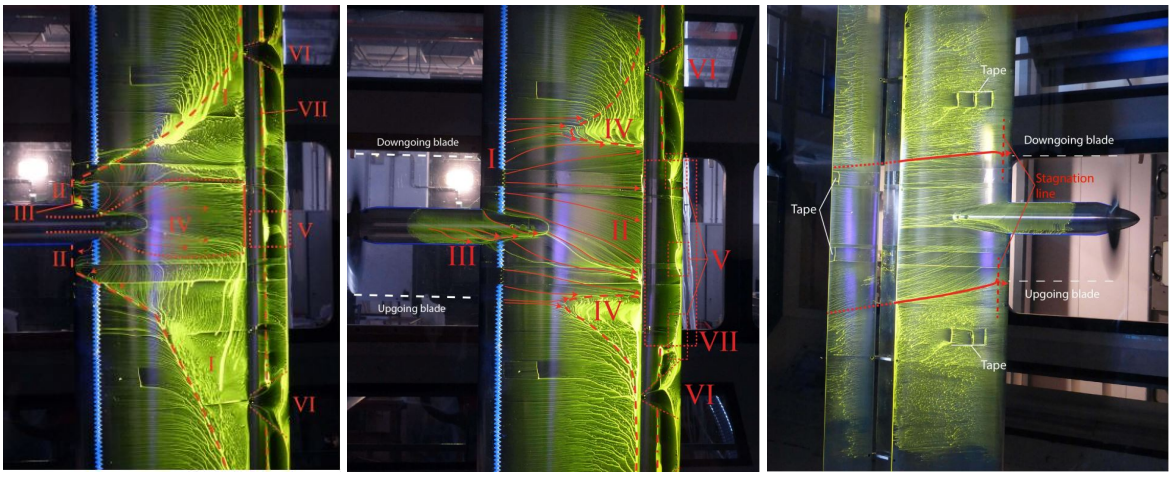

(a) (b) (c)

Figure 2.14: a: Oil flow visualizations of nacelle-wing-flap setup at angle of attack $\alpha = 10°$. flap deflection angle $\delta_f = 30°$. Wing suction side. **b** and **c**: Oil flow visualization at wing suction side resp. pressure side of propeller-wing-flap setup at advance ratio 0.8, angle of attack $8°$ and flap deflection $\delta_f = 30°$. [10]

Roosenboom et al. [12] performed semi-2D (5 side-by-side 2D planes) Particle Image Velocimetry (PIV) measurements of a propeller-wing-flap system, but the PIV-planes in Figure 2.15 only reached from the propeller plane up to the flap leading edge. Roosenboom compared the PIV measurements with unsteady RANS simulations to validate the CFD results, allowing a potential detailed view on the flow field in the flap area, both on the surface of the PWF-geometry as off-the-surface unlike the oil flow visualisations as used by Duivenvoorden, and in 3D, unlike PIV. The CFD results show good qualitative agreement with the PIV measurements, but as the PIV measurements did not include the flap a comparison in this region could not be made and also the CFD flow at the flap is not discussed in further detail.

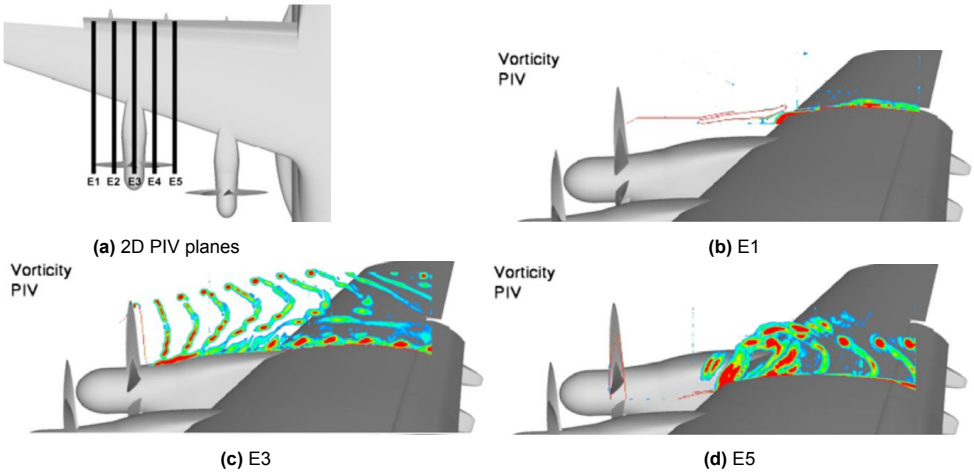

(a) 2D PIV planes **(b)** E1

(c) E3 **(d)** E5

Figure 2.15: PIV vorticity measurements of a 1:17 scale turboprop PWF system at low-speed, high angle of attack conditions. E1-plane is blade-up side. [12]

3

Computational Methods for Propeller-Wing-Flap Simulations

This chapter focuses on the applied computational methods of current literature on aerodynamic interactions between a propeller, wing and flap. The first section discusses CFD methods of wing-flap simulations. Section 3.2 discusses computational methods of propeller simulations. These sections will show that both RANS and URANS simulations are used in current literature. A background knowledge on RANS turbulence modelling is required to correctly interpret CFD results, but also to select an appropriate turbulence model for the use case at hand. Therefore Section 3.3 provides a brief overview of the theory of (unsteady) turbulence modelling while Section 3.4 presents an overview of RANS turbulence models and it's requirements on CFD meshing.

3.1. Wing-Flap CFD simulations

An often used approach to research high-lift aerodynamics are Reynolds-averaged Navier-Stokes (RANS) CFD simulations (e.g. [15–17, 51]), in which all turbulent structures are modelled by turbulence models and only a time-averaged solution is presented. An extension of RANS is the unsteady RANS, or URANS [1], which includes solving slow, large scale, unsteady effects, depending on the spatial- and grid discretization. URANS in general is used when an external time-varying force is present in the simulation setup with periodic vortex shedding, e.g. a transient problem, as is the case in a propeller-wing setup, but it is also applied to wing-flap setups as voted for by Rumsey; Rumsey et al. [15–17, 51] has done continues research in the last decades on wing-flap CFD simulations, focusing on CFD capability, common practices and challenges. Rumsey stresses that *"if a flow field is unsteady, then at the very least the RANS equations must be solved time-accurately: the time scale of any gross unsteady motion should be much greater than the physical time step employed, which in turn should be much greater than the time scales associated with the turbulence"*, implying the necessity of an URANS setup as RANS wing-flap simulations are not able to accurately predict flow separation due to the inherently unsteady structure of these phenomena.

3.2. Isolated and integrated propeller CFD simulations

In general three different approaches to model propellers for RANS CFD simulations are identified from literature: steady actuator disk based approaches, a time dependent actuator line model and full propeller geometry implementation:

- **Actuator disk model** The Actuator disk model is a representation of a propeller as an infinitesimally thin disk of infinite number of blades that 'actuates' the air. The actuator disk model can be implemented in CFD as a boundary condition, which imposes the (in radial direction varying) pressure jumps and flow deviations corresponding to the propeller. The required data can be

[1] Other namings of URANS in literature are transient RANS [52] and very large LES (VLES) [14]

either extracted from isolated propeller wind tunnel experiments or fully resolved blade RANS simulations. This approach is shown to predict propeller-wing interaction *"in good accuracy of the mean flow"* [53], implicitly stating that an actuator disk approach indeed can only be used for a steady solution.

- **Actuator line model** If an unsteady simulation is required, then the actuator line model can be implemented as a computational cheaper option compared to resolving the full propeller geometry. In this approach the actual geometry of the propeller blades is replaced by lines (often positioned at the blade quarter-chord line) consisting of momentum and energy sources, representing the blade loading obtained from isolated propeller data. As such this approach accounts for discrete blade effects and resolving the trailing vorticity in a time-accurate way.

- **Full propeller geometry** One limitation of actuator disk and actuator line models is that they do not include viscous effects. By implementing the full propeller geometry in the CFD setup also the viscous effects of the propeller can be included in the resulting flow field. This requires the implementation of sliding meshes [54] to connect the rotational mesh of the propeller with the stationary reference frame of the propeller and wing.

Stokkermans et al. [13] compares the process and solution of a full propeller geometry with an actuator line and actuator disk modelling approach of a wing tip-mounted propeller geometry with deflected aileron. The computational cost of a full propeller geometry approach increased with 21% compared to the actuator line approach; directly proportional with the mesh cells increase. When the chordwise pressure distribution is considered there is a significant difference between the steady and unsteady solution strategies, but the difference between the actuator line and full propeller geometry solution is only minimal as shown in Figure 3.1.

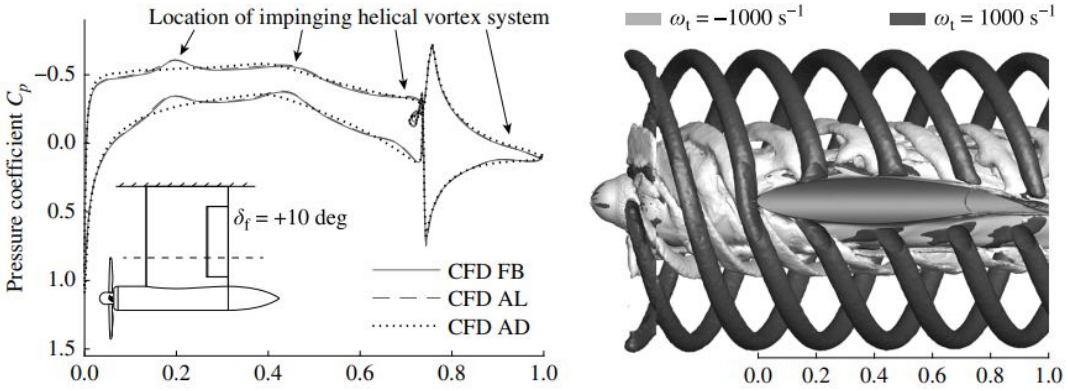

Figure 3.1: URANS S-A simulation of wingtip-mounted propeller with deflected flap by actuator disk (AD), actuator line (AL) and full propeller geometry (FB) approach. [13]

Nevertheless, Stokkermans also notes an important difference between the actuator line and full propeller geometry solution: the solutions of both approaches significantly differ from each other close to the nacelle due the lacking interaction of the blade root and nacelle in the actuator line approach, while propeller-nacelle-wing interaction might result in vortices and flow separation near the main wing trailing edge and flap as will be discussed in Section 2.3 on propeller-wing interaction. For this study a full propeller geometry is preferred over an actuator line approach to research propeller-wing-flap interaction.

Stokkermans also simulated an isolated propeller. Although the full propeller geometry setup was able to accurately resolve the propeller flow field, all three approaches suffer from numerical diffusion. *"Numerical diffusion of the flow quantities in the propeller tip vortices was the only significant source of difference between the FB* [full propeller geometry] *modeling method and the* [isolated propeller] *experiment, resulting also in a reduction in contraction for the FB model."* [13]. An example of this

effect is shown in Figure 3.2a, but also Veldhuis et al. [55] shows a clear example of numerical diffusion of a tip vortex, see Figure 3.2b. Another clear example is shown in the publication of Roosenboom et al. [12]. Main trends to minimize numerical diffusion are the application of higher order numerical solving schemes and/or mesh refinements in the propeller wake area, especially in regions subject to vorticity and boundary layer separation [56].

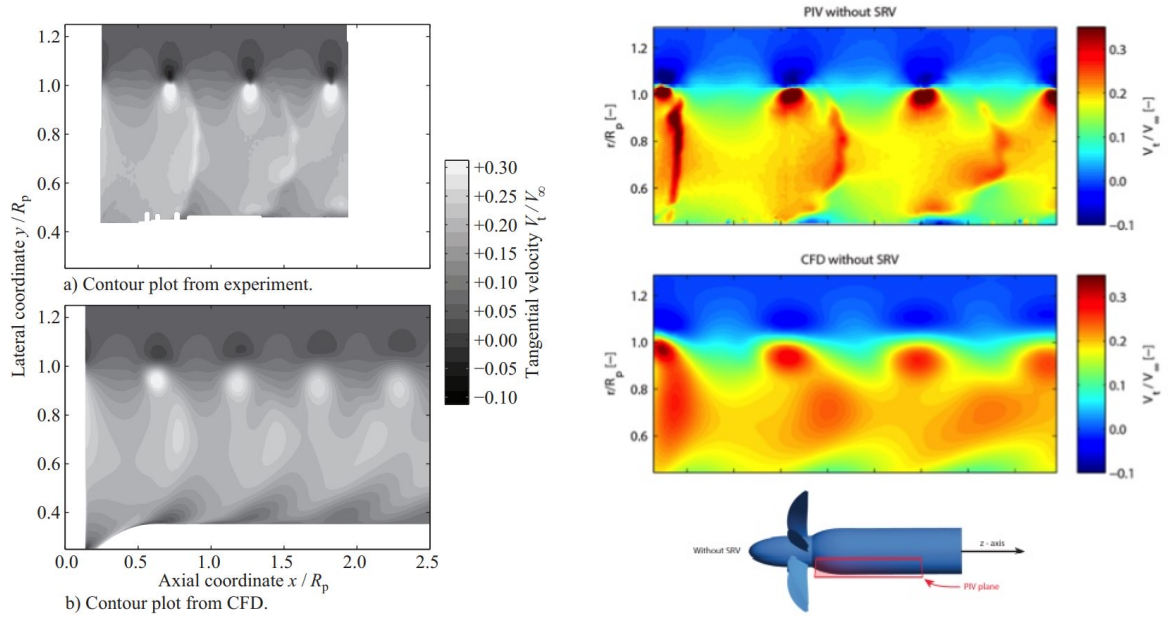

(a) Stokkermans [33]

(b) Veldhuis et al. (edited) [55]

Figure 3.2: Examples of numerical diffusion of a tip vortex. Comparison of propeller slipstream by full propeller geometry CFD versus experimental Particle Image Velocimetry. Both examples used the same propeller (APIAN).

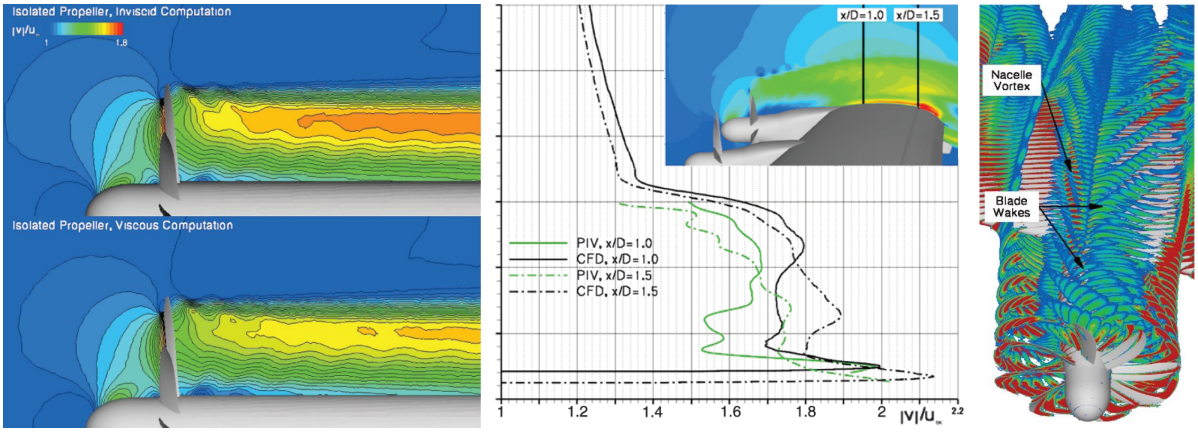

(a) Viscous versus inviscid propeller blade boundary condition

(b) Velocity profiles at two downstream positions, visualizing the effect of inviscid propeller blade modelling.

(c) Vorticity contours of propeller slipstream and other vortex structures.

Figure 3.3: Results of URANS PWF simulation of Roosenboom et al. Exact simulated flight conditions unknown. Note how the propeller tip vortices in Figure **(c)** deviate towards the fuselage due to the swept wing. [12]

In the simulation of Roosenboom et al. [12] The full blade geometry was resolved, but by selecting the blade surface as an inviscid wall in the DLR TAU CFD software. This resulted in, as mentioned by Roosenboom: *"As the inviscid blade modeling does not allow for true viscous wakes to be formed, these vortices cannot be properly represented in the simulation"*. The impact of this decision is shown in Figures 3.3a and 3.3b, in which it is clear that the inviscid modelling over predicts absolute flow velocities when compared to experimental data. Roosenboom stresses on the impact of numerical

dissipation, worsen by the unstructured mesh *and* the selection of the S-A turbulence model that *"tends to overpredict the magnitude of eddy viscosity in vortex cores, contributing to the premature diffusion of these flow structures"*. Yet he identified numerical dissipation as the primary issue w.r.t. propeller-wing-flap system CFD simulations.

3.3. LES vs URANS vs RANS

?? This section presents a brief recap on CFD turbulence modelling. Its goal is not to lecture the reader on the mathematics of this topic, but rather on discussing strengths and weaknesses of different CFD turbulence modelling approaches with respect to the thesis' topic.

Turbulence energy is produced according to the turbulence energy cascade, in which turbulence is produced at the the largest scales, induced by the geometry and boundary conditions of the flow, transferred to medium scale vortices and dissipated by Kolmogorov micro scale vortices in the dissipative range. DNS (Direct Numerical Simulation) fully solves the flow by the Navier-Stokes equations from the largest scales up to the smallest Kolmogorov length and time scales but is not suitable for engineering purposes due to the high computational costs, requiring other approaches to simulate the turbulent structures of a flow field such as LES, RANS or hybrid methods, for example DES (Detached Eddy Simulation).

LES (Large Eddy Simulation) allows for a time-accurate solution and solves the largest turbulent structures, while turbulence structures smaller than a selected filter size are modelled. In RANS (Reynolds-averaged Navier-Stokes) simulations all turbulent structures are modelled by turbulence models and only a time-averaged solution is presented. An extension of RANS is the unsteady RANS, or URANS, which includes solving slow, large scale, unsteady effects. URANS in general is used when an external time-varying force is present with periodic vortex shedding, as is the case in a propeller-wing setup, but is also recommended to improve overall results (prediction of flow separation in general) in a wing-flap setup [51, 57–59]. LES is rarely applied in current literature on propeller-wing interaction due to the too high computational costs. URANS, in contrast, is often chosen for as shown in Chapter 2.

All turbulent structures are modelled in (U)RANS by Reynolds decomposition; the flow solution u is decomposed in a mean flow component $\bar{u}$ and fluctuation u', such that $u_i = \bar{u} + u_i'$. For statistically steady flow simulations the mean flow component $\bar{u}$ is calculated by applying the limit $t \to \infty$, while in URANS simulations ensemble averaging is used instead of time averaging[2] as illustrated in Figure 3.4.

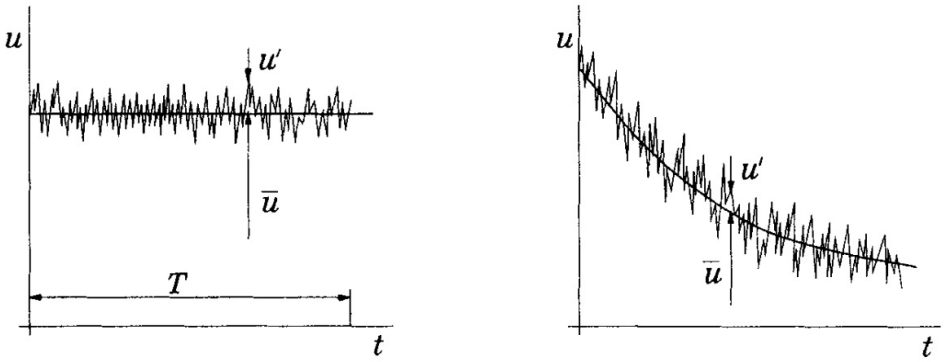

Figure 3.4: Left: time averaging ($\lim_{t\to\infty}$) for statistically steady flow.
Right: ensemble averaging ($\lim_{N\to\infty}$) for unsteady flow. [14]

A full derivation of the RANS equations will not be repeated but can be found in standard CFD textbooks, e.g. [14, 60]. It is however important to discuss how the RANS equations are closed - that is including the influence of turbulence on the flow solution - because this directly affects the final result of the simulation.

[2] For governing equations, see the CFD textbook of Ferziger end Peric [14], chapter 9.4 RANS Models

The fluctuating i.e. turbulent flow components, the latter known as the Reynolds stresses, is defined as $\tau = -\overline{u'v'}$ for 2D cases or more general for 3D applications: $\tau_{ij} = -\overline{u'_i u'_j}$ which exists out of 6 independent elements: the normal stresses $\overline{u'^2}$,$\overline{v'^2}$,$\overline{w'^2}$ and shear stresses $\overline{u'v'}$, $\overline{v'w'}$, $\overline{u'w'}$. Solving the Reynolds stresses closes the RANS equations. This is done by turbulence models that approximate τ_{ij}; based on the the following general notation of the Reynolds Stress Transport equation:

$$\frac{-\partial \tau_{ij}}{\partial t} + \underbrace{K_{ij}}_{\text{Advection}} = \underbrace{P_{ij}}_{\text{Production}} + \underbrace{T_{ij} + D^v_{ij} + D^p_{ij}}_{\substack{\text{Diffusion} \\ \text{turbulent, viscous, pressure}}} + \underbrace{\Phi_{ij}}_{\substack{\text{Pressure strain} \\ \text{correlation}}} - \underbrace{\varepsilon_{ij}}_{\text{Dissipation}} \tag{3.1}$$

3.4. RANS turbulence models

Many RANS turbulence models exist, generally classified as either first- or second-order closure models. Second-order models compute directly the Reynolds stresses by solving all components of the unknown τ_{ij} in Eq. 3.1. These models are known as Reynolds Stress Models (RSM). The terms T_{ij}, Φ_{ij} and ε_{ij} are modelled which is not required for the other terms. RSM give good results for flow with strong streamline curvature, swirl and anisotropic turbulence induced flow structures but are computationally expensive and susceptible for unstable convergence [61].

Mainly first-order models are used to research propeller-wing-flap systems when RANS is selected. First-order closure models are based on the Boussinesq assumption that states that the *"Reynolds* [turbulent shear] *stress components are* [proportional] *connected to the rate of strain with a turbulent viscosity coefficient"* [62], and therefore also known as linear models. This approach is based on determining a proportionality eddy viscosity factor v_t. Therefore first-order models are also known as Eddy Viscosity models (EVM). Widely used first-order models are (modifications of) the 2-equations Jones & Launder $k-\epsilon$ [63] and Wilcox $k-\omega$ [64] models and computationally efficient 1-equation Spalart-Allmaras SA model [65]. Menter proposed a combination of the $k-\epsilon$ and Wilcox $k-\omega$, known as the SST-model [66].

Each turbulence model has its strengths and weaknesses. One slight modification of the geometry or boundary conditions might make an at first good performing model unsuitable:

- $k-\epsilon$ can be applied to exterior flow but results are poor in cases with strong pressure gradient.
- $k-\omega$ gives superior performance for boundary layer flows and is suitable for complex geometries, but separation can be too excessive and too early predicted.
- The SA model has an aeronautic origin and is therefor suitable for airfoils and wings although it performs poorly for free shear flows. It is also robust and computationally cheap.

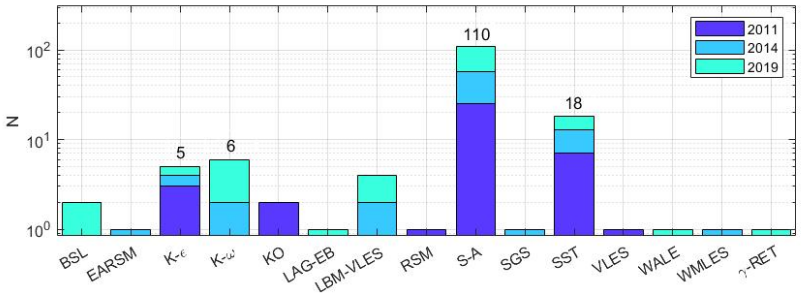

Figure 3.5: Selection of turbulence models (variations not shown) during AIAA high-lift prediction workshops. Own figure, extracted data from Rumsey. [15–17]

The SA model is chosen most often in wing-flap CFD setups as shown in Figure 3.5 due to the reasons above, but also seen in many propeller-wing [11,42,43] and propeller-wing-flap [2,12,26,67] CFD research up to today. The SA model is shown to predict propeller-wing interaction effects accurate when compared to experimental results [12, 43], but the model is prone to numerical dissipation and premature diffusion of vortex cores due to over predicted eddy viscosity's which should be accounted

for [12].

NASA [68] discusses in the order of 20 corrections for the SA model including high-quality references. Two corrections that are often seen in literature are:

- Suppression of the $ft2$ function *" which intends to suppress production of eddy viscosity due to numerical error"* [69], and
- the Rotation Correction, to prevent excessive eddy viscosity in swirling flows [70].

The $k-\epsilon$ model uses a wall-function approach to estimate the boundary layer based on underlying assumptions, while the $k-\omega$ and SA turbulence models resolve the full boundary layer. However, this requires a sufficient mesh resolution of the boundary layer.

From close to the wing surface, or wall, up to the free stream, the boundary layer can be divided in the viscous sublayer ($y^+ < 5$), the buffer layer ($5 < y^+ < 30$) and the logarithmic layer ($30 < y^+ > 300$). In these definitions y^+ is defined as the non-dimensional distance in the boundary layer. The SA turbulence model resolves the full boundary layer, which requires the first mesh cell next to the wall to be of a height of maximum $y^+ = 5$ [71]. Cell sizes succeeding the first wall-bound cell should be gradually increased to successfully resolve the full boundary layer. Turbulence levels should approximate zero in the viscous (laminar) sublayer. The logarithmic layer is fully turbulent which should reduce to low turbulence levels at y^+ values exceeding the order of 300. This build up and diffusion of turbulence in the wall-normal direction can be visualized to determine if the boundary layer is indeed correctly resolved, as is demonstrated in Figure 3.6. In this specific case it is found that the boundary layer was successfully resolved from 25 layers. It also demonstrates that using too few layers (Figure 3.6a) results in a too thick boundary layer, leading to earlier separation. Ansys recommends around 30-40 cells [70].

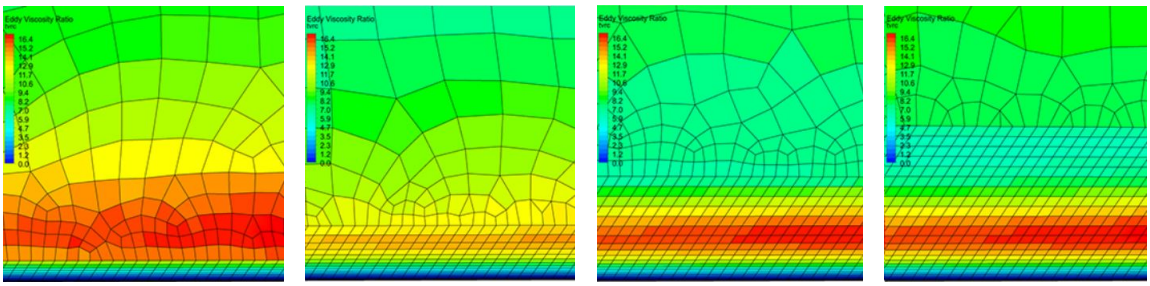

(a) 15 layers **(b)** 20 layers **(c)** 25 layers **(d)** 30 layers

Figure 3.6: Comparison of varying inflation layer heights of unstructured grid of airfoil suction side (racing car front wing). $y^+ = 1$ in all cases. RANS SST. Blue indicates low turbulence levels, red indicates high turbulence levels. [18]

4

Interim Conclusion

High-lift theory describes five 2D main effects from Smith's famous publication: The slat effect, circulation effect, dumping effect, off-the-surface pressure recovery and the fresh-boundary-layer effect. Next to this, wake bursting is explained. One of the dominant effects of standalone propeller aerodynamics is slipstream contraction and expansion. Yet, this effect is overruled by other predominant effects in a full propeller-nacelle-wing-flap systems setup. One of those effects is the divergent pattern of the propeller slipstream on the wing suction side due to suppression of the leading edge suction peak by the nacelle, which is clearly visible in the experimental results of Duivenvoorden. This also reduces the risk of separated flow behind the nacelle, although this region is shifted in spanwise direction to the blade-up side due to the flow structure on the wing pressure side, while another significant propeller-wing interaction effect is the risk of flow separation just outside the propeller slipstream due to disturbances in the spanwise lift distribution. The addition of a flap increases circulation of the main wing, which generally increases the severity of the propeller-wing interaction effects. A nacelle vortex is identified in experimental and CFD setups of Stuermer and Roosenboom, both at propeller-wing and propeller-wing-flap systems. This vortex originates from the nacelle itself and the propeller blade root vortices and moves in opposite direction of the propeller rotation over the nacelle.

Not all flow phenomena of propeller-wing-flap systems are fully understood or researched in detail. Most publications that add a flap to a propeller-wing setup did not focus on the flap flow but rather focus on the overall high-lift performance such as the research of Roosenboom. Although some wind tunnel experiments have focused on the flap aerodynamics of a propeller-wing-flap system, e.g. Duivenvoorden, the corresponding experimental results alone do not lend themselves for a conclusive statement on the origin of observed by oil flow complex flap flow phenomena. CFD simulations can offer a solution by providing insight into off-the-surface flow features to fully understand the flow mechanism at the flap of a propeller-wing-flap system.
Based on the research of Stokkermans and Roosenboom, it is recommended to solve the entire propeller geometry, including viscous effects, to include the root-nacelle interaction of the propeller blade, and obtain the correct magnitudes of axial flow velocity. Yet a high-resolution mesh and higher-order numerical solving scheme are required to minimize numerical diffusion of vorticity.
The flow mechanisms at the flap are of unsteady nature due to the unsteady propeller flow, but unfortunately most of the data in the current literature are presented in time-averaged format, even when URANS is used. The importance of using URANS in high-lift wing-flap only setups due to possible flow separation is voted for by Rumsey. The combination of a propeller and high-lift flow can lead to time-varying flow separation as shown by CFD 'over-the-wing mounted propeller' simulations of Bölk, but publications that researched this subject for conventional tractor-propeller configurations in high-lift setting have not been found.

Concluding, as of today, a knowledge gap exists on a detailed understanding of flap flow in a propeller-wing-flap system, while a thorough understanding of unsteady flap flow behaviour subjected to a propeller slipstream is of interest to maximize high-lift performance in future DEP systems.

5

Research outlook

Most current research focused only limited on the flap flow field, while a thorough understanding of the flap flow field is required to further improve powered high-lift performance. Therefore this chapter presents the current research questions to research the flap flow field of a propeller-wing-flap system at high-lift conditions, i.e. take-off and go-around conditions.

The main research question and its sub-questions are presented in Section 5.1. Limitations and the scope of current thesis is further elaborated upon in Section 5.2.

5.1. Research questions

Literature provides unsatisfactory insight into the details of the flap flow. The diffusing and deflecting flow of the propeller slipstream and time-dependent interaction of the propeller wake with the main wing boundary layer translates downstream to the flap region. Interaction of the flap flow and mentioned effects can occur, resulting in a complex time-varying flow field. Recent experimental oil flow visualisations of Duivenvoorden [10] show the complex flap flow that occurs in a propeller-wing-flap setting, but many of the visualized flow phenomena require further research to investigate their root cause and time-dependent behaviour; oil flow visualisations shows a time-averaged view of the flow field, masking any time-dependent effects. For example, oil flow visualisations do not show the variation of the flow in the boundary layer, i.e. in surface-normal direction which might accelerate or postpone flow separation. Future propeller-wing-flap system development might benefit by filling this identified knowledge gap as flow separation reduces high-lift effectiveness, while increased high-lift performance is one of the benefits of distributed electric propulsion. This leads to the following main research question:

Main research question

What are the flap boundary layer characteristics of a propeller-wing-flap system at high-lift conditions?

An untipped wing is simulated instead of a full wing. Root and tip effects are therefore not included. The high-lift conditions to simulate a take-off or go-around include a single slotted flap deflection angle of 15° with high thrust propeller setting. To answer the main research question, the follow sub-questions are identified:

1. ***what does the flow field of a propeller-wing-flap setup look like at the trailing edge of the main wing and which aerodynamic interactions between the propeller, nacelle and wing shape mentioned flow field?***
   The flow field that the flap experiences is heavily influenced by the propeller, nacelle and wing. This sub-question focuses on describing the flow field prior to the flap in order to determine the start condition of the flap-flow at its leading edge.

2. ***How do propeller root and tip vortices interact with the flap boundary layer flow?***
   The propeller tip and root vortices can interact with the boundary layer flow; directly at the flap surface or indirect via fluctuations at the main wing. Not only on the lifting surfaces suction sides, but on the pressure sides as well.

3. ***How does the flap flow field vary in spanwise direction?***
   Propeller-wing interactions lead to large spanwise variations in lift and drag. The flap flow field will also show spanwise variations due to the already deformed slipstream.

4. ***How does the chordwise position of flow separation at the flap vary within one propeller rotation?***
   Flow separation has a negative effect on lift. Insight in the mechanics of flap flow separation under influence of a propeller slipstream can further improve high-lift performance in future propeller aircraft design.

5.2. Limitations

Literature has shown that interaction effects between a propeller, wing and flap are complex. The SynergIE DEP-12 aircraft that is mentioned in the introduction of this thesis is a complicated aircraft. Considering the current state of knowledge on this subject, this report will focus only on the interactions between a propeller, nacelle, wing and flap by considering a straight, unswept wing, without root and tip effects. It will not aim to fully describe the flow field of a DEP aircraft at take-off or landing. Aerodynamic effects due to, for example, fuselage-wing interaction and wing sweep, that can interfere with the propeller-wing-flap flow field, are not included. Current work will also only consider one operating condition. Trends in aerodynamic effects, i.e. their sensitivity to angle of attack, can therefore not be identified. Furthermore, only a single propeller is considered. Interaction effects between propellers alter the flow field but these effects are not included in this thesis.

Part II

Methods

6

Set-up

This chapter presents the full CFD set-up. The high computational costs of the simulation require a well thought out approach. As such, selected settings are comprehensively motivated. For the (U)RANS simulations a SA turbulence model is used in the selected Fluent software. The motivation for using a CFD approach is elaborated upon in Section 6.1. A brief overview of all relevant settings is presented in Section 6.2. Following sections provide additional background on chosen settings, starting with the physical geometry in Section 6.3. The operating conditions are discussed in Section 5.4. The numerical setup is discussed in Section 6.4. A flowchart of the to be simulated cases is presented in Section 6.6, an introduction of how the strength of CFD to visualize the 3D flowfield is applied in current report is given in Section 6.7. This chapter concludes with limitations of the URANS approach in Section 6.8 and an overview of the used software and hardware in Section 6.9.

6.1. (U)RANS motivation

An URANS approach to answer the research questions is chosen for based on the literature study. Current experimental results do not lend themselves for a conclusive statement of observed complex flap flow phenomena, but also take place at too low Reynolds number at which flow phenomena occur that one does not expect at full scale conditions, for example laminar flow separation bubbles. CFD simulations can offer a solution by providing 3D insight into off-the-surface flow features to fully understand the flow mechanism at the flap of a propeller-wing-flap system while also increasing the setup's Reynolds number to higher values compared to available experimental setups. URANS is highly preferred at high-lift wing-flap simulations already. [15–17, 51]. Steady RANS simulations often converge to a wrong flow field at high angles of attack, while LES simulations are too computational expensive. Furthermore, based on the research of Stokkermans [13, 33] and Roosenboom [12, 24, 72], the full propeller geometry should be modelled to include the root-nacelle interaction of the propeller blade and obtain a real viscous propeller wake, leading to an accurate prediction of the propeller slipstream velocity field.

6.2. Overall settings

The geometry is based on the NLF-MOD22(B) with fowler flap airfoil and TUD-XPROP-S propeller at a Reynolds number of $2 \cdot 10^6$, Mach number M_∞ of 0.15 and spanwise domain equal to $5D_p$. The propeller is placed at approximately $0.85D_p$ upstream of the leading edge. The flap deflection angle is $15°$. Two angles of attack will be simulation for the wing only and prop-off case: $8.3°$ and $11°$, while the prop-on case is only simulated at $8.3°$. The propeller advance ratio is set to 0.765 with an estimated thrust coefficient T_C of 1.2. The simulations are resolved by a second order spacial and temporal discretization with the SIMPLE algorithm. The full propeller geometry is modeled and all walls belonging to the geometry are set to non-slip boundary conditions. The boundary conditions are completed with a velocity inlet, pressure outlet and symmetry-walls at the wing endplanes.

6.3. Physical geometry

The geometric setup of the propeller-wing-flap is scaled w.r.t. Duivenvoorden et al. [10], i.e. the same main NLF-MOD22(B) with fowler flap airfoil and TUD-XPROP-S reference propeller geometry is used. Not only does this allow for a qualitative comparison with results of Duivenvoorden, it also enables validation (Chapter 7) of the CFD setup with experimental results of Boermans and Rutten [20], the creators of corresponding NLF-MOD22(B) airfoil. CAD-files of the wing, flap, nacelle and propeller assembly are provided and used to model the geometry.

6.3.1. Flap setting

A flap deflection angle of 15° is chosen to limit excessive flow separation, as this still remains a hard to predict phenomenon in (U)RANS CFD simulations and the chosen Spalart-Almaras (SA) turbulence model. At $\delta_f = 15^\circ$ [1] the optimal values ($C_l/C_{d,max}$) of dx, flap overlap, and ds, flap gap, are $dx = 8\%c$ and $ds = 2\%c$ and hence applied in current setup [20]. The corresponding airfoil and flap geometry is shown in Figure 6.2.

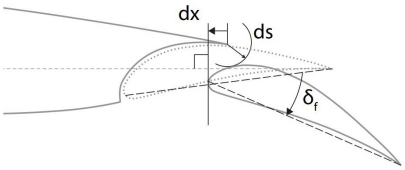

Figure 6.1: Definition of flap overlap $dx[-]$, gap $ds[-]$ - both normalized with chord - and deflection angle $\delta_f[^\circ]$ [10]

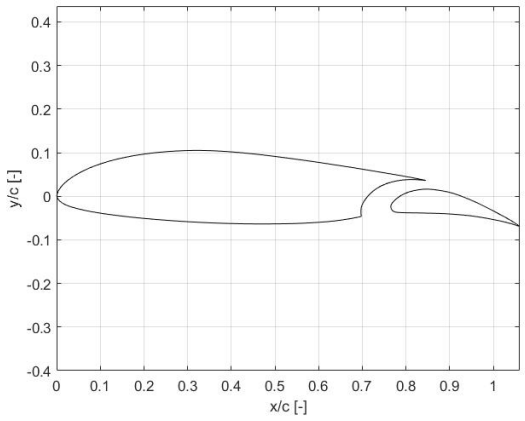

Figure 6.2: Main airfoil and flap geometry of present work $dx = 8\%c$, $ds = 2\%c$ and $\delta_f = 15^\circ$

6.3.2. Spanwise domain sizing

With respect to the spanwise domain sizing it is important to know beforehand how far, relative to the propeller and nacelle centerline, a propeller slipstream influences the wing and flap flow. In this research the focus is on the propeller influence on the flap flow; hence tip and root effects that occur in a finite wing are not considered, nor desired. The spanwise domain sizing of Duivenvoorden can be applied, but at the same time an unnecessary large domain increases computational costs of the already expensive URANS simulations. Therefore, multiple references are considered to select an appropriate spanwise domain size, scaled with respect to the propeller diameter D_p as shown in Figure 6.3 and Table 6.1. In this table, column 3 $(b/2)/D_p$, b is the full aircraft span. This is divided by 2 to obtain the semi-span at which most experiments are performed. column 4 shows at which spanwise distance the propeller had no longer a visual effect, relative to the propeller centerline and normalized with propeller diameter. Based on these findings, a safe $y/D_p = 2.5$ is chosen, leading to a semi-span $b/2$ of $5D_p$. A slight reduction compared to $6.14D_p$ of Duivenvoorden, reducing computational costs.

[1] Note that Duivenvoorden et al. [10] does not contain propeller-wing-flap results at a 15° flap deflection, but unpublished results of this configuration are available for the present study.

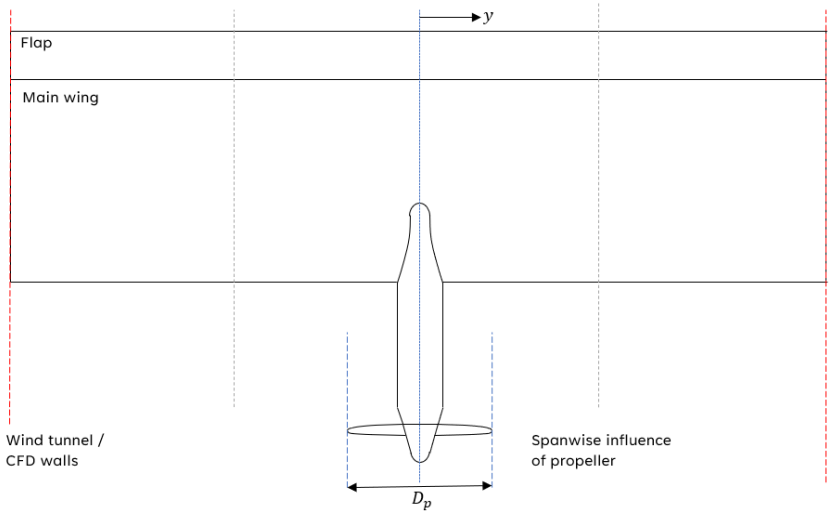

Figure 6.3: Definitions corresponding to Table 6.1

Reference	Propeller-wing (-flap) setup	$\frac{b/2}{D_p}$	Spanwise influence diminished after y/D_p	Based on
Duivenvoorden, 2022 [10]	Exp, 2.5D	6.14	1.5	oil flow visualisations
Keller, 2021 [2]	CFD (RANS AD), 3D	3.18	1.5	spanwise lift distribution
Aref, 2018 [41]	CFD (URANS FB), 3D	4.83	2.2	spanwise lift distribution
Alasdair, 2013 [73]	CFD (URANS FB), 2.5D	3.13	1.5	spanwise lift distribution
Veldhuis, 2005 [5]	Exp, 3D	2.88	>1.4*	spanwise normal force distribution
Moens, 2001 [53]	CFD (Euler), 2.5D	4.13	2.0	spanwise lift distribution

Table 6.1: Spanwise influence of propeller slipstream on wing(-flap) aerodynamics compared to prop-off wing(-flap) flow. 2.5D illustrates the wing clammed between the wind tunnel walls resp. CFD walls. 3D illustrates that at least one wing end is in free-stream conditions to capture tip-effects. AD and FB denotes actuator disk resp. full body geometry to model the propeller. (* The full spanwise domain is influenced by the propeller.)

6.4. Operating conditions

In this section the Reynolds number, mach number, propeller and angle of attack settings are discussed.

6.4.1. Reynolds and Mach number

It is mentioned before that the Boermans data [20] will be used to validate initial wing-flap setup results. Yet as The URANS approach will not include transition modelling, a high enough Reynolds number should be selected at which transition effects are ignorable. Laminar separation bubbles are seen in the results of Duivenvoorden et al. [10] and Lattice-Boltzmann simulations of Ribeiro et al. [74], who both used a Reynolds number of $6 \cdot 10^5$. Transition modelling improved the simulation results of Ribeiro et al. [74]. A Reynolds number of $2 \cdot 10^6$ is high enough to prevent non-occurring full-scale phenomena such as laminar separation bubbles and extensive regions of laminar flow in general [75].
Boermans has performed his experiments at a Reynolds number of $2 \cdot 10^6$. The same Reynolds number is applied in the current research.

A second parameter to consider is the mach-number. Although the flap gap and overlap are non-dimensionalised with the airfoil chord, these parameters are not directly scalable due to the dependency of the boundary layer on the Mach and Reynolds number. The relationship between boundary layer thickness $\delta\ [m]$ and Reynolds number of a flat plate is generally known [75]:

$$\delta_{lam} = 5.2\sqrt{l^2/R_e}$$
$$\delta_{turb} = 0.37l/(R_e)^{1/5}$$

but for the Mach number these relations are less known. For example, higher speeds, hence higher M_∞, increase drag and therefore heat generated, which will lower the local air density and increase the

boundary layer thickness. [76]. Viscosity is also affected through Sutherland's approximation. Therefore, the same Mach number as Boermans is applied, 0.15.

6.4.2. Propeller operating conditions

Typical propeller operating conditions are shown in Table 6.2; high disk loading implies a low advance ratio J and corresponding high T_c. Yet too low advance ratio's might cause stall at large sections of the propeller blades, which also depends on the blade pitch angle. A typical take-off or go-around speed of modern commercial turboprop aircraft is $110kts = 57m/s$, hence freestream $M_\infty = 0.17$ and corresponding $Re_{MAC} = 12 \cdot 10^6$, based on a typical $3m$ mean aerodynamic chord. Scaling the TUD-XPROP-S propeller with a factor 10 (as Duivenvoorden used a chord of $0.3m$), gives a full-scale diameter of $2.032m$. Typical RPM settings of propellers of that size are in the order of 2200, such that the tip mach number is in the order of 0.70 to prevent excessive propeller noise and shock waves.[2] This results in an advance ratio of $J = 0.765$, which will therefore be used in the present research.

Flight phase:	Take-off	Climb	Cruise	Approach
Blade pitch [deg]	20-30	30-45	45-60	< 45
Thrust coefficient T_C	> 0.8	0.2-0.6	0.1-0.4	≈ 0
Propeller efficiency η_p	> 0.8	> 0.8	> 0.8	< 0.6
Advance ratio J	< 1.0	1.5-2.0	2.0-3.0	> 3.0

Table 6.2: Typical propeller operating conditions for turbo-prop aircraft, extracted from [7].

The selected Reynolds number, chord length, advance ratio and propeller diameter add up to a propeller RPM of 9929. The corresponding propeller tip speed is $211.3m/s$, which equals a feasible M_{tip} of 0.616 at zero freestream velocity, or $M_{tip} \approx 0.63$ at $U_\infty = 51.45\ m/s$ (the influence of axial induction factor neglected). Isolated reference data of the TUD-XPROP-S ($D = 0.2032m$) is available (Figure 6.4), so that also a suitable pitch angle can be selected. From this data the most efficient pitch angle at $J = 0.765$ is $30°$, measured at $r/R = 0.7$.

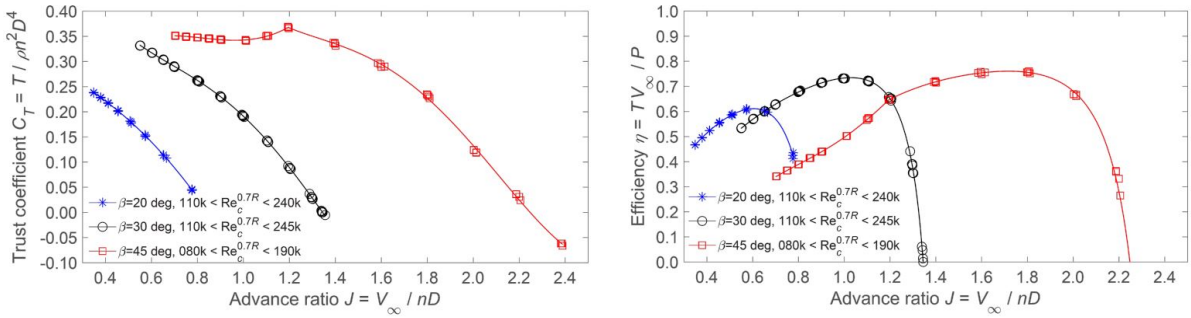

Figure 6.4: TUD-XPROP-S experimental reference data, isolated propeller [19] (unpublished)

6.4.3. Angle of attack setting

The computational expensive URANS simulations do not allow for a full angle of attack sweep; only one angle of attack will be simulated of the full propeller-wing-flap case, so a suitable α at which the research questions can be answered shall be selected beforehand. As the selected Reynolds and Mach numbers are equal to Boermans his experiment, his angle of attack sweeps and pressure-distribution plots of the wing-flap setup are consulted: $C_{Lmax} \approx 2.6$ at $\alpha \approx 14°$.
The results of Duivenvoorden differ from Boermans, among other reasons due to the different Reynolds number; in his research at respective settings $C_{Lmax} \approx 2.25$ at $\alpha \approx 12°$ at prop-off, no nacelle. At full propeller-wing-flap configuration ($J = 0.8$), performance is seen to increase to $C_{Lmax} \approx 2.45$ at $\alpha \approx 11°$,

[2] Propeller RPM scales with the diameter to obtain feasible tip mach numbers. For example, a Fokker 50 propeller has a diameter of $3.66m$ and hence a RPM of only 1200, resulting in a tip mach number of $M_{tip} = 0.67$.

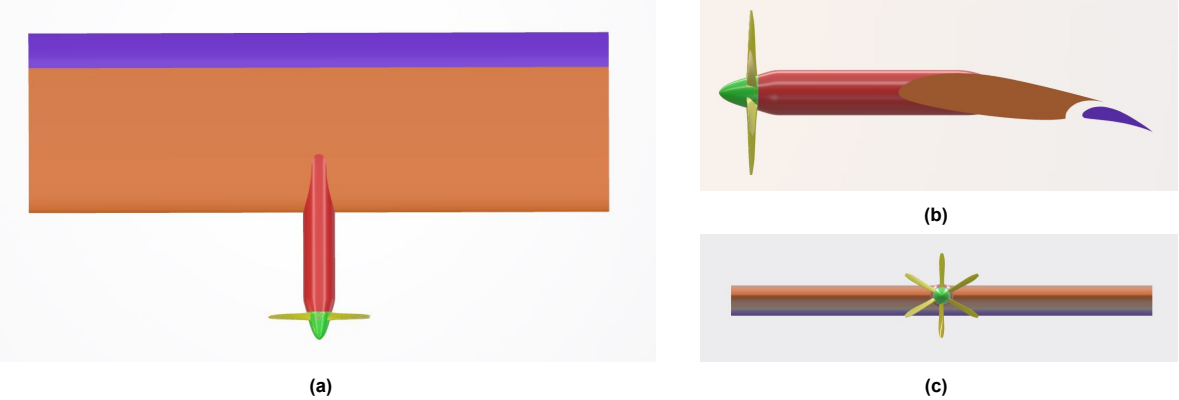

Figure 6.5: Propeller-wing-flap geometry of present research. Top view (a), side view (b) and front view (c).

yet significant areas of separated flow due to nacelle-wing interaction effects start to form $\approx 3^\circ$ prior. Primarily an α of 8.3° is selected to validate the CFD approach with Boermans' available experimental data at 8.3°. This setting is at the start of the non-linear portion of the lift wing-flap lift curve in which areas of separated flow start to shape [10]. Next, interacting effects are profound and 8.3° is a realistic operating conditions of aircraft at take-off, landing and go-around. Secondary, simulations at $\alpha = 11^\circ$ are performed to gain further insight in general trends of flow mechanisms, such as the further development of areas with separated flow and gain experience in CFD (U)RANS solving strategies for case 1b.
Based on the preliminary results and solver stability it is chosen for to run the propeller-wing-flap simulation at 8.3°. This decision is further elaborated upon in Chapter 7. An overview of the settings of Duivenvoorden, Boermans and the present research are presented in Table 6.3. The propeller-wing-flap geometry is shown in Figure 6.5.

	Boermans (wing-flap)	**Duivenvoorden (propeller-wing-flap)**	**Present Research**
$b/2\ [mm]$	1250	1248	2032
$c\ [mm]$	600	300	600
$\frac{b/2}{D_p}\ [-]$	-	6.14	5
$\delta_f\ [^\circ]$	$0, 15, 30, 40$	$0, 15, 30$	15
$dx\ [mm](\delta_f = 15^\circ)$	$8\%c$	$8\%c$	$8\%c$
$ds\ [mm](\delta_f = 15^\circ)$	$1\%c, 2\%c, 3\%c, 4\%c$ ($2\%c$ optimal setting)	$2\%c$	$2\%c$
$\alpha\ [^\circ]$	$[0 - 16]$	$[-5 - 14]$	$8.3, 11$
$Re\ [-](\delta_f = 15^\circ)$	$2 \cdot 10^6$	$6 \cdot 10^5$	$2 \cdot 10^6$
$M_\infty\ [-](\delta_f = 15^\circ)$	0.15	0.088	0.15
$U_\infty\ [m/s](\delta_f = 15^\circ)$	51.45	30.2	51.45
$D_p\ [mm]$	-	203.2	406.4
$J\ [-]$	-	$0.8, 1.0$	0.765
$V_{tip}\ [m/s]$	-	$236\ (J = 0.8)$	211
$T_c\ [-]$	-	$1.05\ (J = 0.8)$	≈ 1.05
$C_T\ [-]$	-	$0.33\ (J = 0.8)$	≈ 0.33

Table 6.3: Boermans [20] versus Duivenvoorden [10] versus present research setup

6.5. Numerical setup

The computational domain, boundary conditions and Fluent solver settings directly affect the CFD solution. Well-motivated choices should be made to obtain an accurate flow field. This section will discuss the setup of the computational domain to represent free stream conditions and how this matches with the velocity inlet, pressure outlet and no-slip walls boundary conditions. Also relevant solver settings are discussed, followed by meshing and discretization settings

6.5.1. Domain

A bullet-shaped side-view domain is set up such that the curved surface can be used as inlet, while the downstream surface can be used as outlet, as recommended by Ansys [71, 77]. Based on the same reference the domain shall be shaped in such a way that the domain extents at least 50 body lengths in all directions. A side-view of the domain is shown in Figure 6.6, which also includes various meshing and significant regions (body of influences, sliding interface), that will be elaborated upon in Section **??**. Yet, to simplify the implementation of the sliding mesh the propeller is placed perpendicular to the domain x-axis, which implies that the wing is placed at a 5° angle of attack in the domain reference frame by default. The corners of 75° between the velocity inlet and pressure outlet ensures that the full velocity inlet boundary condition imposes a positive mass flow into the domain at the selected angle of attack along the whole boundary condition.

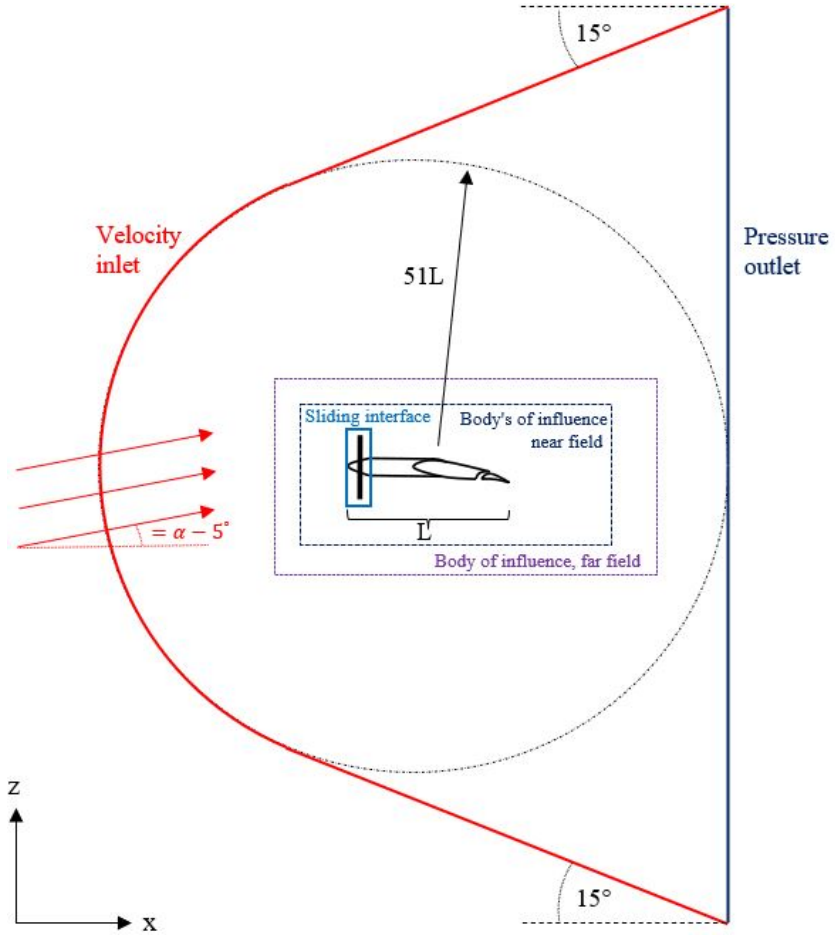

Figure 6.6: Schematic sketch of CFD domain sizing, boundary conditions and meshing regions. Not to scale.

The inlet is set to a velocity of $51.45 m/s$ with a turbulent viscosity ratio of 5 [77, 78]. An operating (reference) static pressure of $1013.25\ hPa$ is defined. A constant pressure boundary condition is applied to the outlet, equal to the operating static pressure by selecting a static gauge pressure (which is defined relative to the operating static pressure) at the outlet of $0\ hPa$. A no-slip boundary condition is applied at the full propeller geometry, wing and flap. The side-walls of the domain are defined as symmetry planes [70, 71, 79–81].

6.5.2. Solver settings

The pressure-based solver in Fluent is selected. The pressure-based solver is recommended for low-speed aircraft aerodynamics, as the density-based solver is inefficient at low mach numbers hence (almost) incompressible flows [77]. Furthermore, the pressure-based solver has an up to a factor 2

lower memory consumption. Density is calculated by the ideal-gas law. Air dynamic viscosity is calculated in Fluent by Sutherland's Law.
The suppression of the $ft2$ function and the Rotation Correction of the SA turbulence model are turned on, according to the motivation in Section **??**. No other adjustments to the turbulence model are made.

6.5.3. Meshing

A hybrid-grid is implemented, consisting of an unstructured far-field with semi-structured inflation layers near the walls. While the unstructured grid increases numerical diffusion, a full structured grid was considered infeasible due to the complex geometry. A Polyhedral mesh is selected in the Fluent software due to its lower RAM requirements and reduced convergence time when compared to default tetrahedral meshing, while accuracy is not adversely affected (e.g. [82].)
The meshing can be divided in multiple 'regions': The far-field, the body-of-influences, the sliding (rotating) mesh and the boundary layers. The body-of-influences are refinement-regions, consisting of relative small cells when compared to the far-field, and is required to gradually transition from the small inflation-layer cells to larger far-field cells. The body-of-influences will also ensure that the wake-mesh is sufficiently refined to minimize numerical diffusion of vortex cores as recommended by Roosenboom [12] and ability to resolve general system-interaction flow structures.
An unsteady RANS simulation of a propeller, in Fluent named as a transient RANS simulation, requires the propeller and its hub to actually rotate. As such, the mesh around the propeller and hub should rotate as well. The rotating mesh and the stationary mesh connect to each other by an 'interface zone', where both mesh-regions meet, as depicted in Figure 6.6

The boundary layers are fully resolved, requiring a y^+ of ≈ 1 as discussed in Section **??**. Due to the high Reynolds number flow, this requires a small initial cell height. The associated surface sizing should be sufficient to prevent bad quality cells due to the boundary layer sizing, next to the fact that the surface sizing should also be appropriate to capture the curvature of the geometry. It is aimed for to discretize all surfaces by at least 100 cells in chordwise (or curvature in general) direction [77]. Yet leading and trailing edges require a higher resolution discretization in the order of 0.1% chord length.

Table 6.4 shows the mesh-settings of all simulated cases, see Figure 6.7, to adhere to discussed practices.

6.5.4. Temporal discretization

The temporal discretization, hence the time-stepping of the URANS simulations, is based on the CFL or Courant number. The Courant number indicates the number of mesh cells a fluid particle crosses between two time-steps of a transient simulation. The maximum Courant number is generally smaller than 1 and the mesh and time-step should allow this condition to be adhered to. When stable, one can gradually increase the time step. A time-step equal to a propeller rotation of 2° is aimed for.

6.5.5. Solver solution methods

In Fluent varying solution schemes exist; numerical algorithms to solve the Navier-Stokes equations. The difference between each algorithm is how the coupling between the pressure-momentum system is handled. The most common algorithms are SIMPLE (Semi-Implicit-Method-Of-Pressure-Linked-Equations) and PISO (Pressure-Implicit-of-Split-Operations). Both can be used in transient simulations where Ansys recommends the use of PISO for transient flow calculations [71]. Yet, PISO is more prone to unstable convergence in case of bad-quality meshes when compared to SIMPLE due to its under-relaxation factors of 1.0. This can be solved by reducing its under-relaxation factors below 1.0, but then one looses the main benefit of PISO: it's ability to converge in 1 iteration (at a slightly higer cost compared to one SIMPLE iteration). Due to the large mesh-dependency of PISO, for this report SIMPLE is used.

			Applicable to case:	1a	1b	2
Body of influence cell sizes $[m]$	Far field		0.05	✓	✓	✓
	Near field		0.01	✓	✓	✓
	Wing wake refinement region		0.005	✓	✓	✓
	Propeller and nacelle wake refinement region		0.0025		✓	✓
Surface face sizes $[m]$	Propeller blades (curvature size function is used)		$5e$-5 up to 0.001			✓
	Propeller hub and nacelle		0.001		✓	✓
	main wing	leading edge	0.001	✓	✓	✓
		mid section	0.0015	✓	✓	✓
		trailing edge	0.004	✓	✓	✓
	flap	leading edge	0.00088	✓	✓	✓
		mid section	0.00177	✓	✓	✓
		trailing edge	0.0002	✓	✓	✓
Inflation layer settings	Propeller blades	First layer height $[m]$	$6e$-6			✓
		Growth rate	1.15			✓
		Number of layers	36			✓
	Propeller hub and nacelle	First layer height $[m]$	$6e$-6		✓	✓
		Growth rate	1.15		✓	✓
		Number of layers	36		✓	✓
	main wing	First layer height $[m]$	$6e$-6	✓	✓	✓
		Growth rate	1.15	✓	✓	✓
		Number of layers	36	✓	✓	✓
	flap	First layer height $[m]$	$6e$-6	✓	✓	✓
		Growth rate	1.15	✓	✓	✓
		Number of layers	36	✓	✓	✓

Table 6.4: Key mesh settings

6.6. Cases

At this stage it is clear that the propeller-wing-flap CFD setup is complex. Therefore a building-block philosophy is applied [83], starting with a benchmark case before transitioning to a subsystem case and the complete system with increasing complex flow features.

The benchmark case is a relative simple RANS wing-flap setup (Case 1a in Figure 6.7) to ensure that the simulation correctly resolves the boundary layer. General quantities such as C_L, C_D and chord-wise pressure distributions will be validated by Boermans his experiment in Chapter 7. Next a nacelle (including spinner) is included in Case 1b (RANS), focusing on correct solving the general flow field as predicted in Chapter 2 but more specific by comparing qualitative results with the research of Duivenvoorden [10] and the MSc thesis of Suard [42]. Indeed, Case 1a and 1b use a RANS setup. The usage of RANS instead of URANS is chosen for in these 2 cases due to the significant shorter solving time while the corresponding accuracy of the flow is expected to be sufficient for the goals of these 2 cases. Yet an URANS run will be performed at case 1b to familiarize with transient RANS simulations. Results of case 1a and 1b are discussed in Chapter 7, while the results of case 2 are discussed in Chapter 9. The geometries of all cases are shown in Figure 6.8. The mesh is kept as much as equal between all cases to minimise effects of any mesh dependency, including the rotating sliding mesh in Case 1a and 1b.

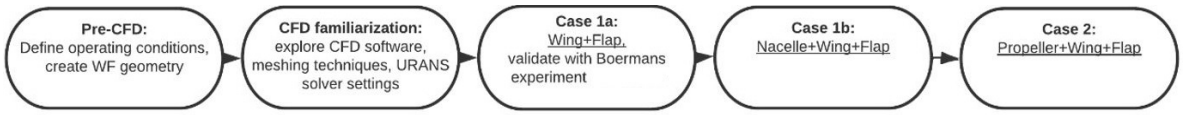

Figure 6.7: Flowchart of the CFD setups

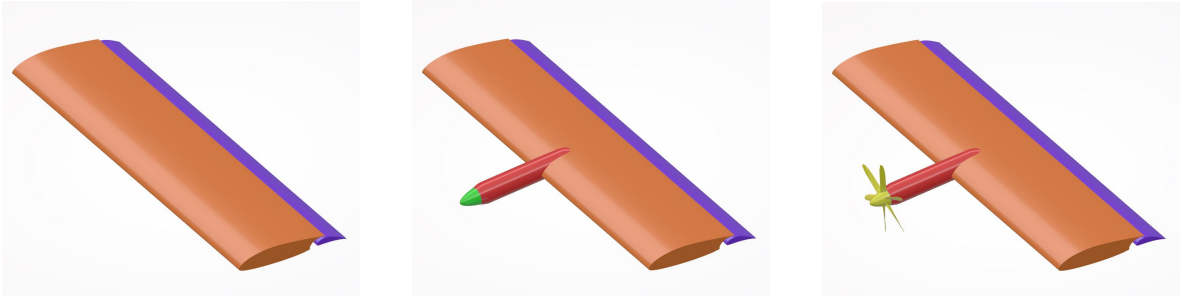

(a) Case 1a **(b)** Case 1b **(c)** Case 2

Figure 6.8: Overview of geometries of CFD setups

6.7. Results and their relevance

One of the benefits of CFD is its ability to visualize the 3D flow field. This report will heavily focus on 3D flow field visualisations (e.g. but not limited to velocity streamlines, total pressure coefficient planes, Q-criterion iso-surfaces) to gain insight in the complex flow field of current setup. Findings of the 3D flow field will be coupled to its influence on 2D surface results, for example surface shear lines, pressure coefficients etc, but also to the experimental oil flow visualisations of Duivenvoorden [10] to obtain a full dimensional understanding of occurring flow phenomena. Unsteady effects will be quantified by visualising spanwise time-dependent variations in lift, surface shear stresses and skin friction coefficients and surface-normal variations in flow velocity.
To conclude, the results will provide the reader with an in-depth view on propeller-wing-flap flow phenomena in general, and time-dependent flap boundary layer flow behaviour more specifically to increase our understanding on propeller-wing-flap high-lift performance.

6.8. Limitations

The unsteady RANS approach directly leads to limitations that shall be discussed beforehand due to its importance and kept in mind when interpreting the results.

- (Unsteady) RANS simulations struggle with solving flows undergoing large adverse pressure gradients [15–17, 84], which will occur in present research due to the high-lift setting. The accuracy of corresponding flow phenomena, such as separated flow, can therefore be questionable, next to the limitations of RANS turbulence models discussed in Chapter 3 (i.e. vortex core premature diffusion).
- The high computational costs of the PWF URANS simulation do not allow for continues re-meshing, solving and post-processing. Considering the time span of this thesis, this concludes that no mesh dependency study can be included in this report. Due to the large setup, the results will be influenced by the mesh resolution which unfortunately can not be quantified.
- An unsteady RANS simulation can solve slow, large scale, unsteady flow if an appropriate small time step is chosen. The flap (and main wing) boundary layer is expected to show time varying flow due to its interaction with the propeller slipstream and corresponding vortex shedding. An actual isolated wing boundary layer subjected to an adverse pressure gradient shows turbulent structures at its outermost area [85, 86]. Such high frequency fluctuations will not be captured by an unsteady RANS simulation.
- (Experimental) validation data is very limited and its applicability to current propeller-wing-flap setup as well, for example due to a different Reynolds number. Some qualitative comparison shall be performed, but quantitative validation is extremely limited for the full setup.

6.9. Software and hardware

The following main software and hardware items are used:

Software

CATIA 3DEXPERIENCE and Ansys have been chosen as they are the common CAD and CFD software tools used at the FPP-department of AE TU Delft.

- **CATIA 3DEXPERIENCE** to modify provided CAD-files of the wing, flap, nacelle and propeller assembly such that they can be used for CFD purposes. This includes scaling of the models and defeaturing, i.e. removing protrusions and holes in the CAD models, as given CAD-models are used to manufacture the actual wind tunnel model and therefore contain too much detail that is not required, nor desired, for proposed CFD analysis.
- **Ansys** Workbench, Design Modeler and Ansys Fluent are used to setup the CFD workflow of each case, import the defeatured CAD-files, calculate the mesh and setup the boundary conditions and general solver settings. Ansys CFD Post, Ansys Fluent and Ansys EnSight are used to visualize and analyse results. Ansys distribution 2020 R2 is used.

Hardware

- A regular **Windows 10 laptop** is used for CATIA 3DEXPERIENCE. (Intel® Core™ i7-7700HQ 8 cores 2.80GHz CPU, 16 GB RAM, NVIDEA GeForce GTX 1050 Ti 4 GB VRAM GPU.)
- The **TUD1002979 workstation** is used for meshing, setting up the Ansys case files and post-processing. A user can login to the Windows 10 environment by a remote desktop connection. This workstation is equipped with an Intel® Xeon® Gold 6248R 48 cores 3.00GHz CPU. A total of 800 GB RAM is available, as Fluent case and data files can easily reach sizes of $\approx$ 80 GB. A fair-use policy is in place for students to use a maximum of $\approx$20% of available resources.
- **TU Delft HPC cluster**: TU Delft research groups have access to a total of 10 High Performance Computer (HPC) clusters. The AE-faculty HPC cluster has a total of 1536 multi-core CPU's. A fraction of this ($\approx$ 320-1000 cores) will be used to solve the CFD cases. The cluster has a Linux CentOS 7 operating system and communication with the cluster is command-based. For detailed information on the HPC cluster, see: hpcwiki.tudelft.nl/index.php/Main_Page.

7

Verification and Validation of CFD setup

In this chapter the verification and validation results of the three CFD setups are discussed.

Case 1a is primarily validated by the experimental results of Boermans [20] quantitatively. Ribeiro et al. [74] has recently performed Lattice-Boltzmann simulations of the same geometry and setup as Duivenvoorden, including a wing-flap setup, and will therefore be used as a secondary verification and validation source for the presented CFD results. Furthermore, case 1a is also used to verify if the mesh is sufficient to capture the boundary layer and confirming overall sufficient spatial discretization.

No validation data is available for case 1b and case 2. The CFD results are qualitative compared with the experimental results of Duivenvoorden et al. [10] and Lattic-Boltzmann CFD simulations of Ribeiro et al. [74]. The comparison primarily focuses on confirming correct trends of the flow field instead of a quantitative validation approach.

7.1. Case 1a, Wing-Flap

Case 1a has been solved at two angles of attack: $8.3°$ to validate with Boermans and $11°$. Both simulations successfully converged below a RMS error of $1e$-6, see Figures 7.1 and 7.2 The mesh and results are discussed in the following paragraphs.

7.1.1. Assessment of mesh quality

A polyhedral mesh was created, shown in Figure 7.3. The y^+ values are sufficient; the maximum y^+ of 1.6 occurs at the leading edge of the main wing. The average y^+ of the main element is 0.4. At the flap a maximum y^+ of 1.0 is found at the leading edge with an average value of 0.5. A further reduction of the height of the first cell in the inflation layer was found to be infeasible to also keep y^+ at the leading edge of the main wing below 1 due to the significant increase in mesh size to keep orthogonal quality above 0.05.
A sufficient y^+ is not an overall indication of a mesh that is able to successfully resolve the boundary layer flow. Equally, a sufficient resolution of the inflation layers is key to correctly model the boundary layer flow, and the inflation layer and surface face sizing settings should be sufficient to allow a smooth transition from the inflation layers to the bulk mesh. A challenging factor in the meshing process is the gap between the flap upper surface and the main wing trailing edge, which houses the inflation layers of both surfaces; thus limiting the maximum height of both inflation layers. A trade-off had to be made between a sufficient resolution of the inflation layers and the smoothness of the transition to the bulk mesh. Within the available computational resources, it was considered infeasible to further refine the surface mesh of the wing and flap, resulting in a relatively coarse transition from the last inflation layer cell to the bulk mesh, as shown in Figure 7.3d. The coarse transition however does not seem to adversely affect the results and in general good agreement is found with the experimental results of Boermans as shown in Table 7.1.

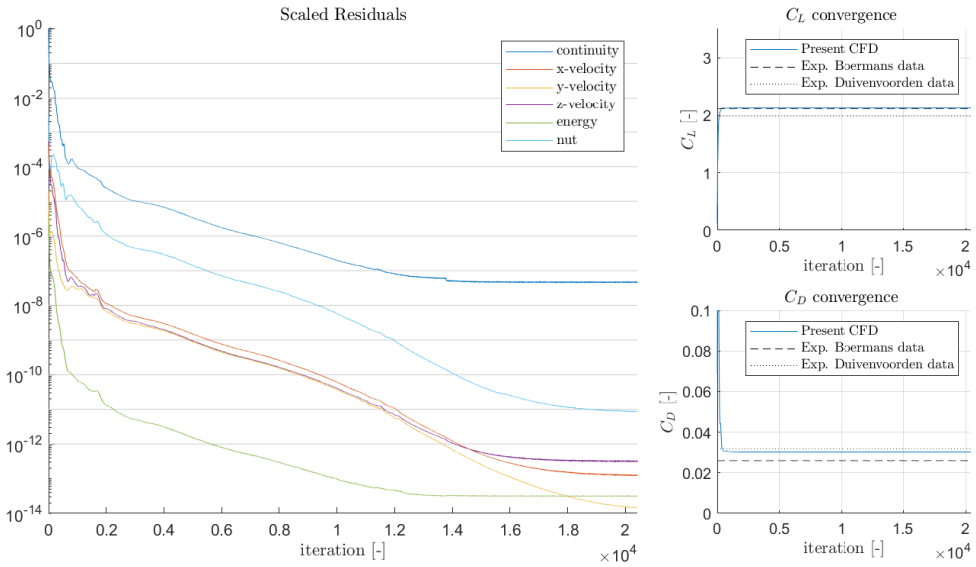

Figure 7.1: Convergence history, $\alpha = 8.3°$

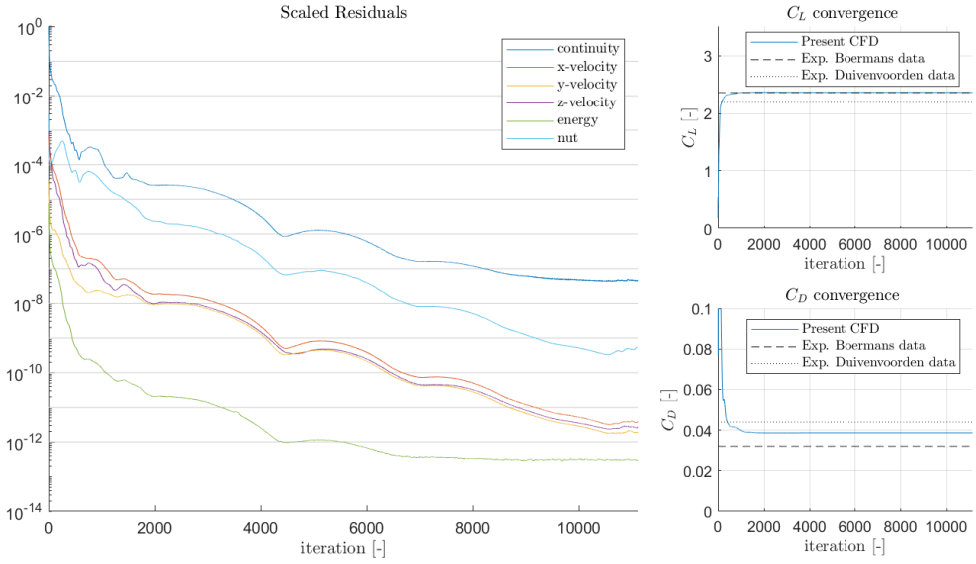

Figure 7.2: Convergence history, $\alpha = 11°$

		Present research (Difference w.r.t. Boermans)	Boermans	Duivenvoorden
$\alpha = 8.3°$	C_L	2.12 $(+0.47\%)$	2.11	1.98
	C_D	$3.02 \cdot 10^{-2}$ $(+16.2\%)$	$2.60 \cdot 10^{-2}$	$3.18 \cdot 10^{-2}$
$\alpha = 11°$	C_L	2.37 $(+0.42\%)$	2.36	2.19
	C_D	$3.87 \cdot 10^{-2}$ $(+20.9\%)$	$3.20 \cdot 10^{-2}$	$4.40 \cdot 10^{-2}$

Table 7.1: Comparison in C_L and C_D of present research

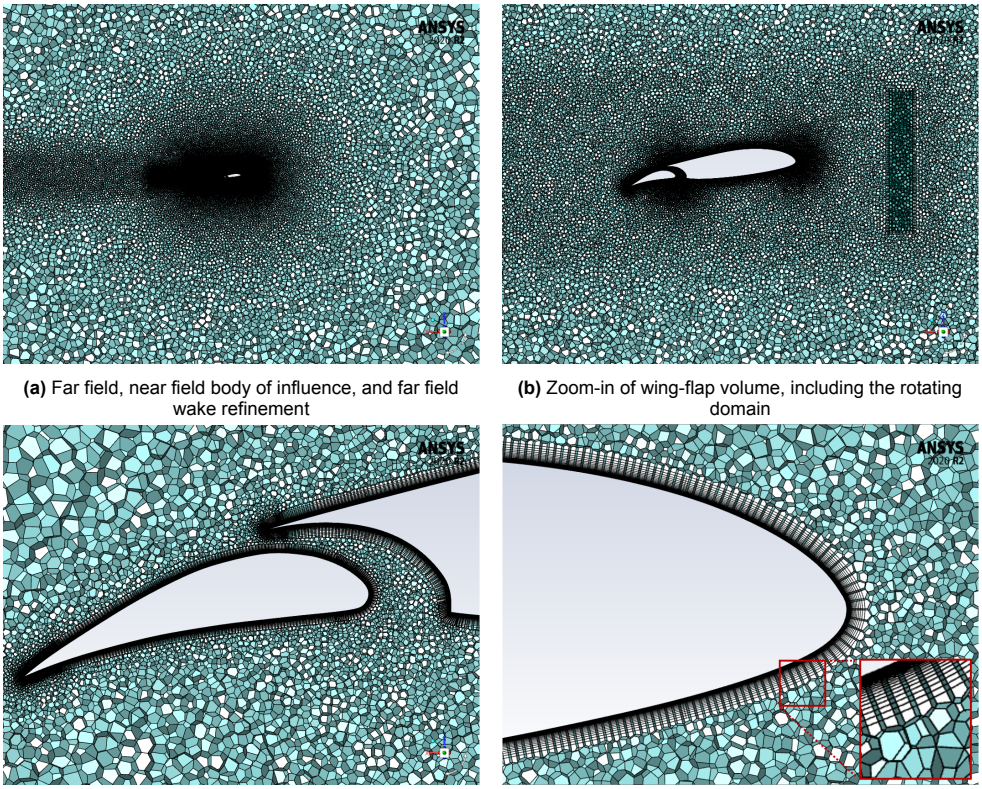

(a) Far field, near field body of influence, and far field wake refinement

(b) Zoom-in of wing-flap volume, including the rotating domain

(c) Zoom-in of main wing trailing edge, flap and cove area.

(d) Zoom-in at main wing leading edge inflation layers

Figure 7.3: Meshing of case 1a, cut-plane at mid-span position. Total of 117 million polyhedral cells.

7.1.2. Obtained lift, drag and chordwise pressure coefficient distribution

Table 7.1 shows good agreement of C_L with the experimental results of Boermans, which is also represented by a sufficient match of the experimental obtained chordwise C_P distribution with the CFD results of present study, shown in Figure 7.4. Yet two clear differences are visible:

1. The trailing edge pressure distribution of the main element does not represent the extrapolated data of Boermans. The Boermans extrapolation seems to represent rear loading of a single-element airfoil, likely due to the cove shape. Yet the CFD results do represent typical multi-element pressure distributions (e.g. [3, 87]); the flap circulation increases flow velocities in the cove area, reducing the main element trailing edge C_P. The trailing edge pressure distribution by CFD is therefore deemed physical, next to matching with the results of Ribeiro. [74].
2. The dips in the flap suction-side pressure distribution at 80.5% and 89.5% x/c. Those dips originate from the separated flow of the main wing element's cove area, interacting with the pressure distribution near the flap surface. Similar structures and under-resolvement of the extremes in these regions are seen in the research of Ribeiro when assuming fully turbulent flow, yet better matching CFD results were obtained when transition was included in their setup. It is therefore concluded that the mismatch between experimental and present CFD results is caused by the fully-turbulent RANS assumption of the present setup.

A significant error in C_D is observed up to 20.9% compared to Boermans. This error did not reduce with

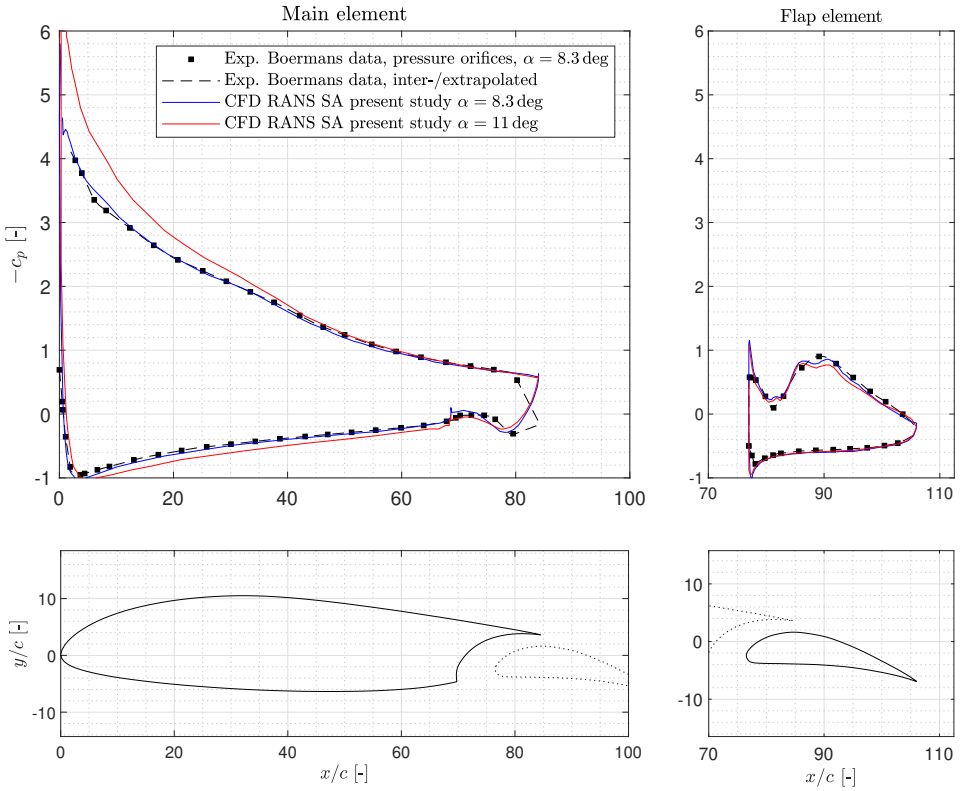

Figure 7.4: CFD results at angles of attack $8.3°$ and $11°$ of case 1a compared to experimental Boermans wind tunnel data [20]. The inter-/extrapolation of the experimental data is performed by Boermans.

further mesh refinements and can explained by the full turbulent flow assumption of RANS. Boermans did not apply forced transition in his setup while laminar separation bubbles are observed. In fact, the NLF-Mod22 airfoil is designed to postpone transition, reducing drag by maintaining laminar flow as long as possible.

To further place the CFD in context, also the experimental results are included in Table 7.1. The C_L of Duivenvoorden is under predicted due to Reynolds effects, mach number effects and application of forced boundary layer transition [10]. The C_D values exceed the Boermans results, even though they only include pressure drag. The C_D values of present CFD simulation are in between Duivenvoorden and Boermans results. The C_L and C_D of the CFD simulation are overall acceptable considering the goal of case 1a.

7.1.3. Assessment of boundary layer solving by velocity and turbulence intensity profiles

A main goal of case 1a is to confirm if the mesh is sufficient to capture the boundary layer. For this, the build up and diffusion of turbulence is visualized by contour plots in Figures 7.5a and 7.5b and further quantified in Figure 7.6. Station 1 and 2 in the latter figure show typical velocity distributions, with an increased suction peak at $11°$ compared to $8.3°$ as expected. The velocity profile at station 2 shows a typical trend with a slightly thicker boundary layer at $11°$ compared to $8.3°$ due to the increased adverse pressure gradient [76]. The velocity profiles show a smooth transition from the inflation layer mesh to the bulk mesh. An equally smooth transition is seen for the turbulence viscosity ratio, while Figures 7.5a and 7.5b show that the main wing inflation layer does not extend far enough to include the peak of turbulence viscosity ratio at the trailing edge.

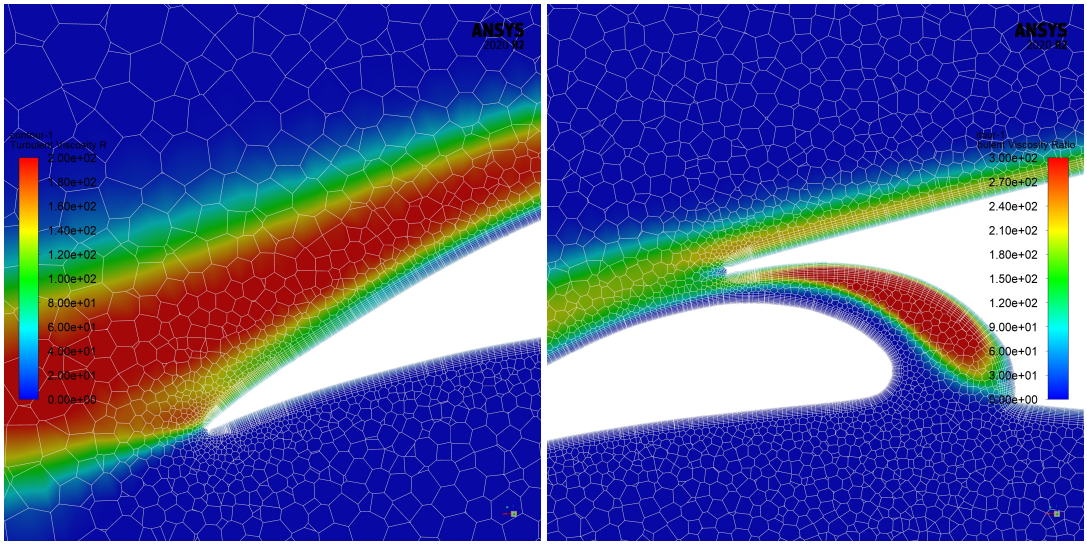

(a) Turbulence viscosity ratio μ_t/μ (clipped to 300) at mid-span, flap trailing edge

(b) Turbulence viscosity ratio μ_t/μ (clipped to 200) at mid-span, cove area.

Figure 7.5: Turbulence viscosity ratio to visualize boundary layer solving of case 1a, $8.3°$.

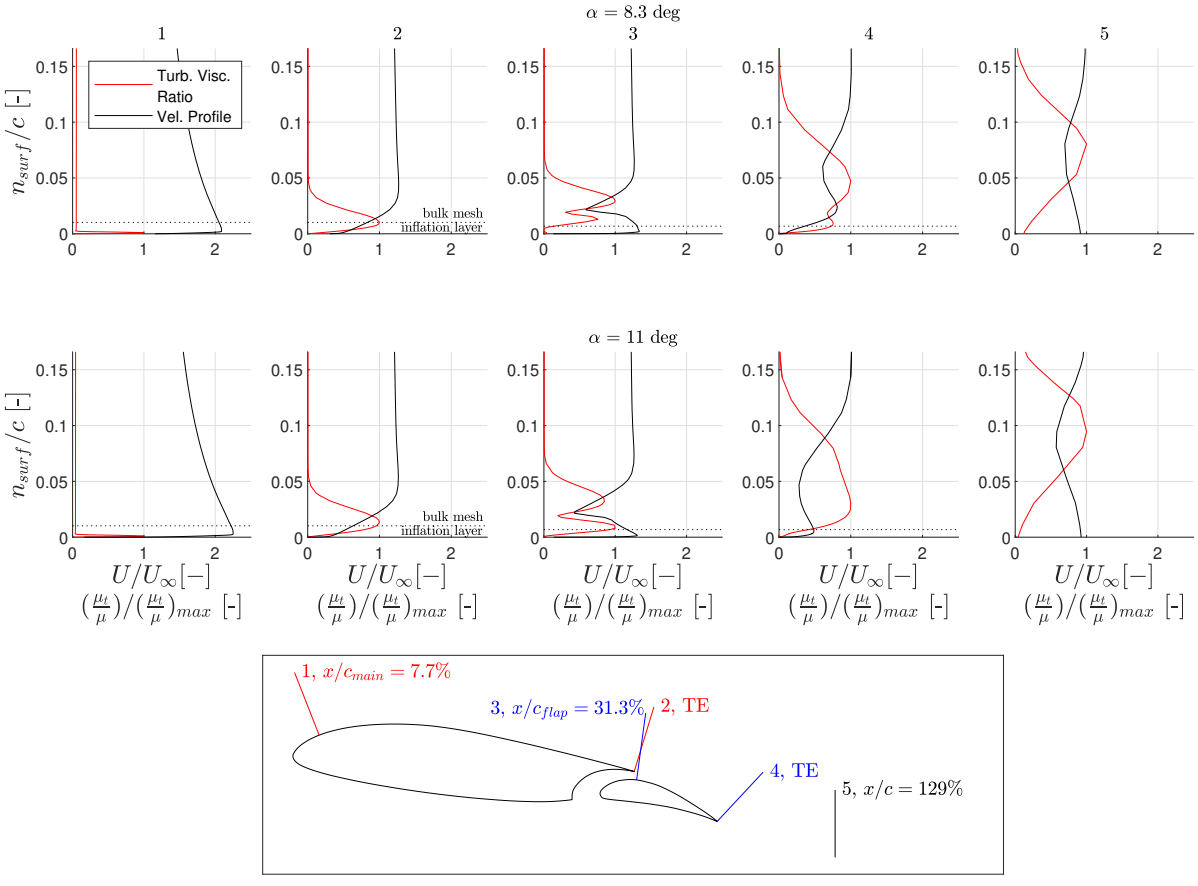

Figure 7.6: Velocity and turbulence viscosity ratio profiles at various stations of case 1a. Velocity is scaled w.r.t. U_∞, while turbulence viscosity ratio is scaled with the max turbulence viscosity ratio at respective station.

At stations 2 and 3 the diffusion of turbulence to free-stream values extends a bit further than the boundary layer. A similar trend is seen in experimental literature [88, 89]. Station 4 shows clear boundary layer confluence of the main element and flap. The boundary layer of the flap at $11°$ is earlier influ-

enced by the main element wake compared to $8.3°$. The reduced flap velocity at $11°$ compared to $8.3°$ shows that the flap flow is approaching flow reversal hence separation. The turbulence intensity is also more profound. The wake-flow at station 5 shows lower minimum velocities and a larger wake at $11°$ compared to $8.3°$. The profiles match trends of the *Ansys best practices guide* by Menter [70].
To conclude, the well matching values of C_L with Boermans' experiment, the reasonable C_D when considering the assumptions made in the CFD setup and general trends of the velocity and turbulence intensity profiles in the main element and flap boundary layers give sufficient confidence in applied meshing techniques to continue with case 1b.

7.2. Case 1b, Nacelle-Wing-Flap

In case 1b a nacelle and hub are added to the geometry of case 1a. The same meshing settings are applied, but the fluid region downstream of the nacelle required additional refinement by a body of influence to successfully resolve nacelle-wing interaction flow phenomena. The solution at $\alpha = 8.3°$ converged, as shown in Figure 7.7, yet only to a maximum $1e\text{-}4$ residual. Solving the flow at $\alpha = 11°$ subsequently required an URANS setup.

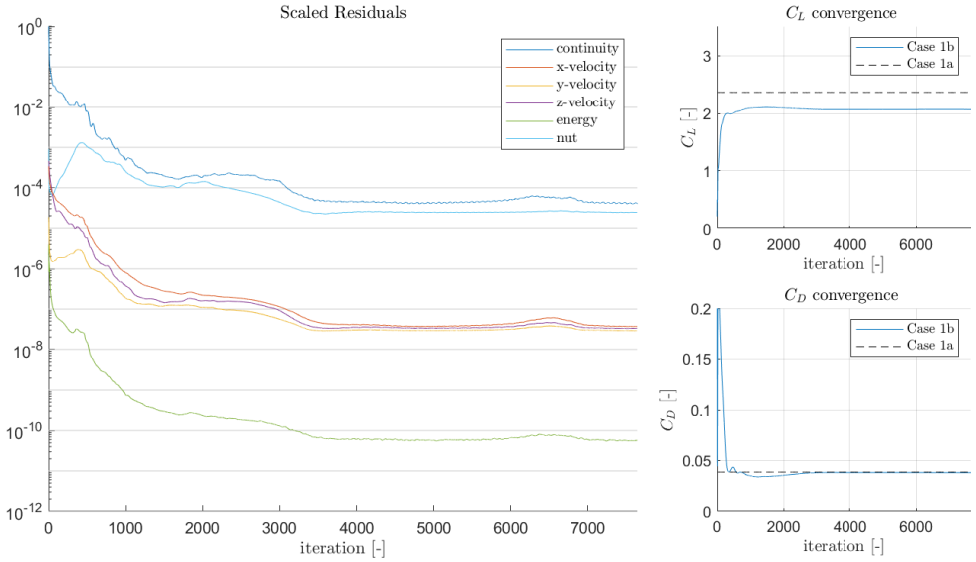

Figure 7.7: Convergence history (RANS), $\alpha = 8.3°$ of case 1b.

In the next section the results of case 1b at $\alpha = 8.3°$ are discussed, including a comparison of the surface flow field with the experimental results of Duivenvoorden and extensive 3D visualisations of the volume flow field. Section 7.2.2 discusses the results at $\alpha = 11°$.

7.2.1. Angle of attack 8.3 deg

Figure 7.8 shows the mesh, sliced through the middle of the spanwise domain. The obtained C_L and C_D are shown in Table 7.2.
Most important, Duivenvoorden's lift and pressure drag measurements are based on two rows of pressure tabs only at spanwise locations $y = \pm 0.35 D_p$ relative to the nacelle centerline, in close vicinity of the predicted suction peak as is visible in the chordwise C_p distribution in Figure 7.10. At $8.3°$, the C_L has slightly reduced from 2.12, case 1a, to 2.06. A reduction in C_L of approximately the same magnitude is seen in the results of Duivenvoorden. A large discrepancy is seen in the C_D value at $8.3°$. The present study shows a rise in C_D, while Duivenvoorden shows a large reduction to a negative -pressure drag only- C_d value. Duivenvoorden relates this *"to the suction peak at the leading edge of the main element due to the blockage of the nacelle"*, reducing pressure drag. The experimental results show a rapidly changing C_{dpress} with α overall, from slightly negative at $\alpha = 8.3°$ up to $C_{dpress} = 0.25$ at $\alpha = 12°$. The present CFD simulation shows an overall pressure drag increase from $C_{Dpress} = 2.16 \cdot 10^{-2}$ of case

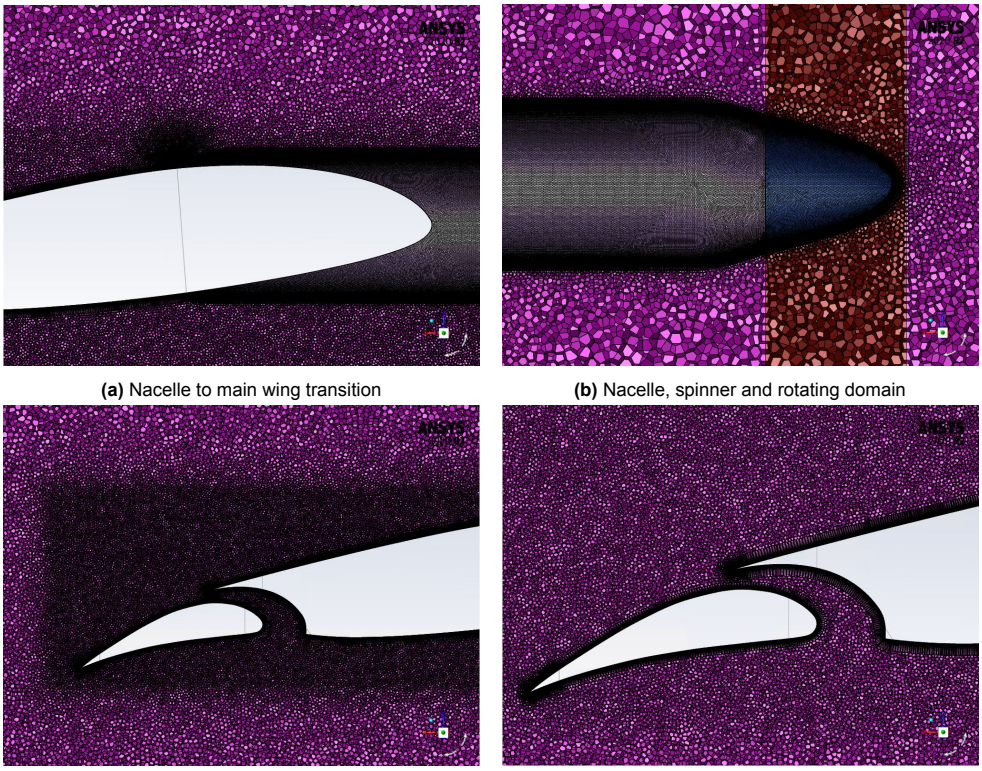

(a) Nacelle to main wing transition

(b) Nacelle, spinner and rotating domain

(c) Body-of-influence to capture nacelle-wing-flap interaction effects

(d) Zoom-in of wing-flap volume of interest. Notice the difference in growth rate and cell size of the near-field to capture nacelle interaction effects compared to Figure 7.3c

Figure 7.8: Cut-plane of mesh at mid-span position. Total of 155 million polyhedral cells.

		Present research	Duivenvoorden(*)
$\alpha = 8.3°$	C_L	Case 1b: 2.06	Case 1b: 1.90
		Case 1a: 2.12	Case 1a: 1.98
	C_D	Case 1b: $3.82 \cdot 10^{-2}$	Case 1b: $-6.71 \cdot 10^{-3}$
		Case 1a: $3.02 \cdot 10^{-2}$	Case 1a: $3.18 \cdot 10^{-2}$
$\alpha = 11°$	C_L	Case 1b: 1.73 (RANS)	
		Case 1b: 2.17 (URANS)	Case 1b: 1.99
		Case 1a: 2.37	Case 1a: 2.19
	C_D	Case 1b: $1.61 \cdot 10^{-1}$ (RANS)	
		Case 1b: $1.05 \cdot 10^{-1}$ (URANS)	Case 1b: $8.2 \cdot 10^{-2}$
		Case 1a: $3.87 \cdot 10^{-2}$	Case 1a: $4.40 \cdot 10^{-2}$

Table 7.2: Comparison in C_L and C_D of Case 1b to experimental Duivenvoorden data and case 1a. URANS results are not fully converged, see Section 7.2.2. (* Duivenvoorden results are measured at two spanwise locations (average is shown) and only pressure drag is measured.)

1a to a $C_{Dpress} = 2.88 \cdot 10^{-2}$ at case 1b. Figure 7.9 shows a sectional reduction of $C_{d,press}$ to negative values in the nacelle vicinity due to the increased suction peak near the wing-nacelle intersection. A $C_{d,press}$ of $-1.44 \cdot 10^{-2}$ is found, versus $-6.71 \cdot 10^{-3}$ of Duivenvoorden. This is considered sufficient given the complex flow and RANS setup.

Present results are compared with oil flow visualisations of Duivenvoorden by Figure 7.11. In general, the CFD surface shear lines show similar trends as Duivenvoorden his flow visualisations. The experiment shows slightly increased flap trailing edge stall, downstream of the nacelle. Signs of this are also seen in the CFD results. The maximum spanwise extend of flow separation in the CFD results is marked by the red-dotted line, and resembles the extend of the experimental $8°$ result reasonably well. Duivenvoorden however does not show reversed flow at the nacelle-wing intersection at $8°$. The lower

experimental Reynolds number and given that the leading edge separation bubble occurs upstream of the trip-strip are expected to contribute to this discrepancy. A leading edge separation bubble is however clearly present at the 10° setting.

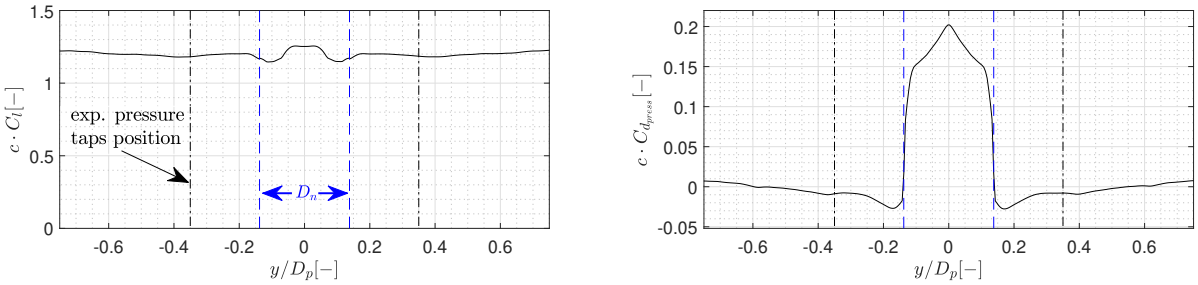

Figure 7.9: Spanwise lift and pressure drag of case 1b at $\alpha = 8.3^\circ$. Dotted blue lines indicate diameter of nacelle D_n. Dotted black lines indicate location of pressure tabs of Duivenvoorden [10].
Left: spanwise sectional $c \cdot C_l$ **Right:** spanwise sectional $c \cdot C_{d,press}$

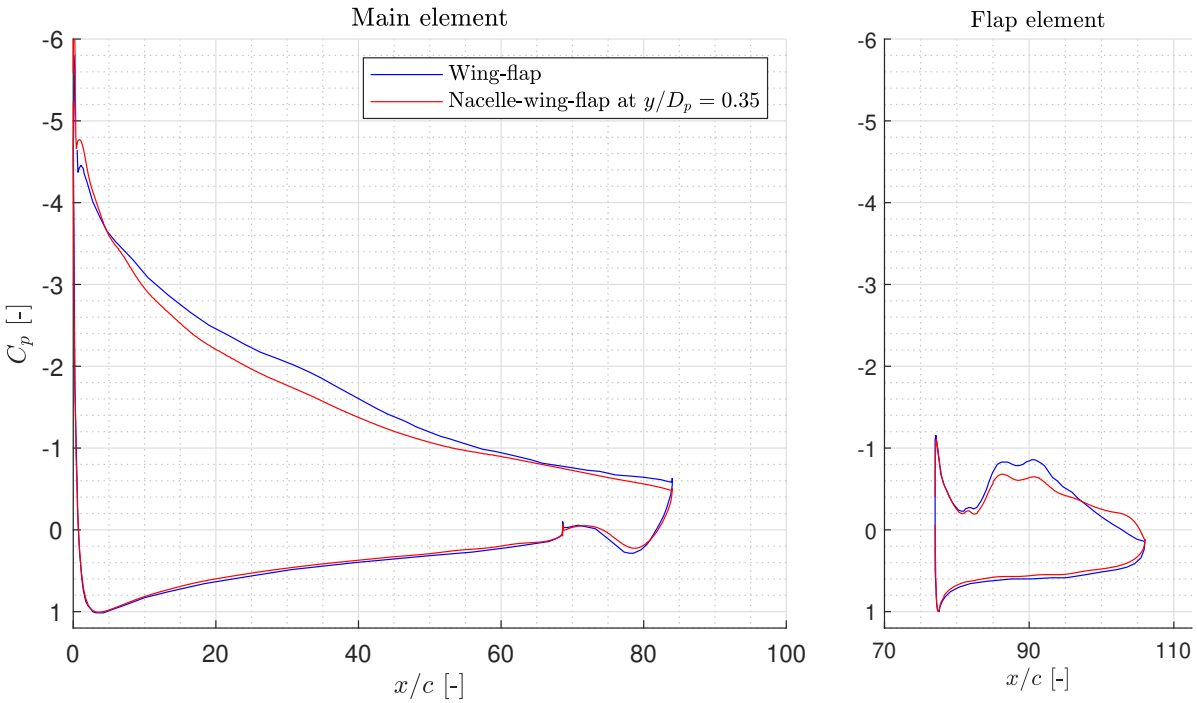

Figure 7.10: Chordwise pressure coefficient at $y/D_p = 0.35$ from nacelle centerline of Case 1b vs Case 1a at $\alpha = 8.3^\circ$.

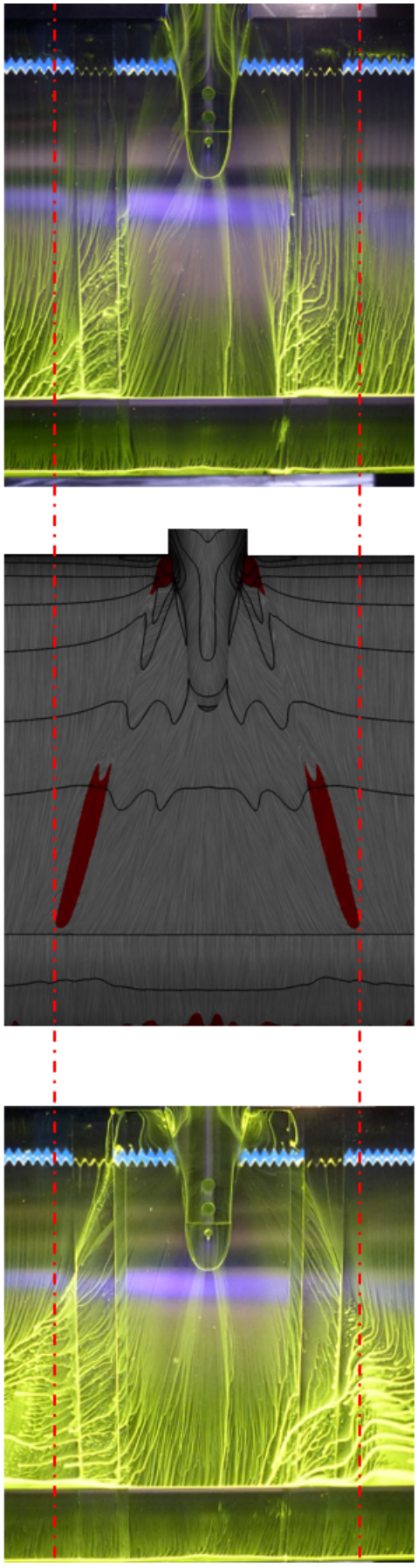

Figure 7.11: Case 1b, red dashed lines are reference lines. **Top:** Duivenvoorden result of nacelle-wing-flap setup at $\alpha = 8°$. **Middle:** present CFD, LIC in which red indicates shear in upstream direction at $\alpha = 8.3°$ **Bottom** Duivenvoorden [10] (unpublished result) of nacelle-wing-flap setup at $\alpha = 10°$.

7.2.2. Angle of attack 11 deg

Case 1b at $\alpha = 11°$ is solved by RANS and URANS. The RANS solution showed insufficient convergence and a nonphysical high-lift flow field, including fully separated flow downstream of the nacelle which is not seen in the experimental setups of Duivenvoorden and Suard [42] and also not expected by literature. This is further attested by the under prediction of C_L and over prediction of C_D in Table 7.2 of the RANS solution. An unsteady RANS simulation is therefore performed.
The usage of URANS in high-lift, high angle of attack, setups was already voted for by Rumsey as discussed in Section 2.1. Excessive and incorrect flow separation when using RANS did occur during the high-lift workshops, while URANS was capable to simulate correct physical flow in these workshops [17, 70]. The present results agree with this trend.

The URANS solver settings involve a time step of $5e\text{-}5[s]$. A maximum of 50 inner iterations is selected to allow the residuals to reduce to maximum order $1e\text{-}6$ at each time step. A total of 8000 time steps is solved in 388,664 iterations by at average 480 cpu cores in 28 days (322,560 CPU hours), for a total flow time of $0.4[s]$, equaling a flow distance traveled of $51.45 \cdot 0.4 = 20.58[m]$. Characteristic flow phenomena are successfully formed and resolved after $0.4[s]$, yet it is seen in Figure 7.12 that the flow forces have not been converged yet after this time period. Extending the flow simulation is not chosen for due to the high computational costs, but it is believed that the flow should fully converge within an additional $\approx 0.2[s]$ due to the parabolic behaviour of the The C_L and C_D convergence.

The $\alpha = 11°$ URANS C_L (2.17, extrapolated 2.18, +0.5%) and C_D ($1.05 \cdot 10^{-1}$, extrapolated $1.02 \cdot 10^{-1}$, -2.8%) results follow the same trend as Duivenvoorden compared to $\alpha = 8.3°$ in Table 7.2.

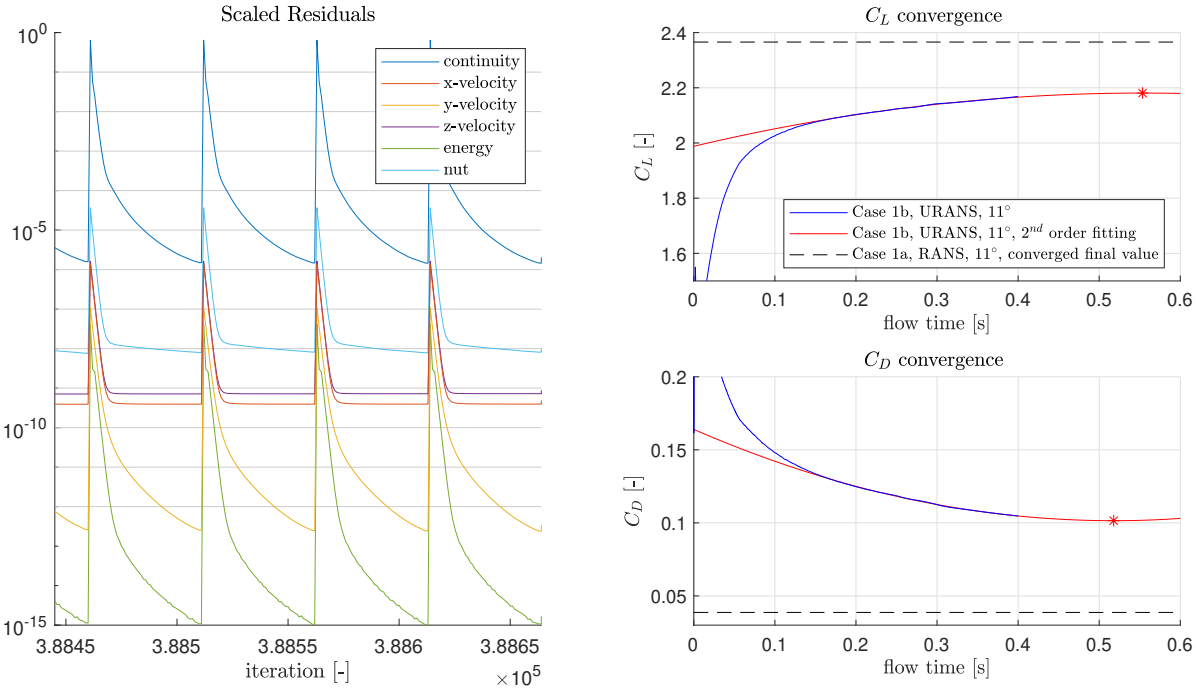

Figure 7.12: Convergence history (URANS) of case 1b $\alpha = 11°$. Scaled residuals of the last 4 time steps is shown, next to C_L and C_D convergence. Red stars denote expected final value, based on second order extrapolation of the last 0.25 $[s]$.

Mean flow quantities of the current URANS solution are sampled in a time interval of $0.015[s]$ from $t = 0.4[s]$ to $t = 0.415[s]$, hence $t \cdot U_\infty = 0.77[m]$ in timesteps of $\Delta t = 2.5e\text{-}4$ such that $\Delta s = 0.013[m]$.

The mean flow field in Figures 7.13b and 7.13d shows a near symmetrical flow field as expected, which is clearly not the case in the time-accurate representations. The nacelle-wing intersection suction peak increased from C_P -8.4 at $8.3°$ to -9.6 at $11°$ mean results. The averaged shear contours shows the wedge-shaped separation-critical regions by low shear stresses in x-direction, but the actual regions of negative x wall shear are considerably smaller than the $8.3°$ RANS solution as shown in Figures 7.13c and 7.13d. It is expected that this is due to the averaging of the periodic vorticity shedding. Averaging

the flow could prevent the mean surface shear in downstream direction to reduce below negative values, thus limiting regions of averaged flow reversal. This is further elaborated upon in Chapter 7.

This section has shown the sensitivity of RANS at high-lift conditions and provided some initial training in unsteady RANS simulations. Based on convergence behaviour of case 1b it is decided to continue case 2 at an angle of attack setting of $8.3°$.

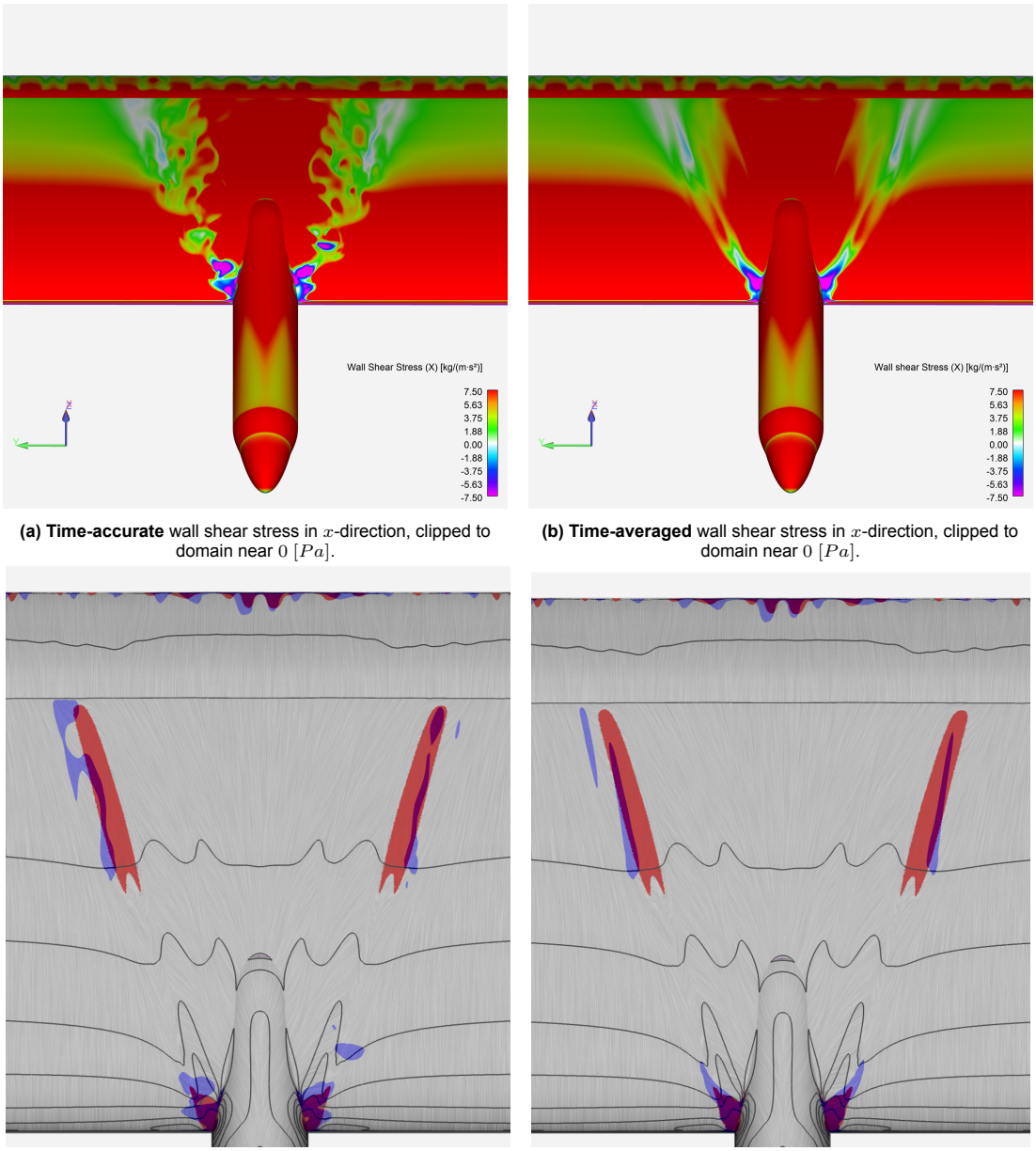

(a) Time-accurate wall shear stress in x-direction, clipped to domain near 0 $[Pa]$.

(b) Time-averaged wall shear stress in x-direction, clipped to domain near 0 $[Pa]$.

(c) Time-accurate flow reversal in blue, overlapped with RANS $8.3°$ flow reversal in red.

(d) Time-averaged flow reversal in blue, overlapped with RANS $8.3°$ flow reversal in red.

Figure 7.13: Vomparison between time-accurate flow field and time-averaged flow field of case 1b at $\alpha = 11°$. Time-accurate flow shown at $t = 0.415[s]$. Time-averaged flow is sampled from $t = 0.4[s]$ to $t = 0.415[s]$ in time steps of $\Delta t = 2.5e\text{-}4$.

7.3. Case 2, Propeller-Wing-Flap

This section compares the results with Duivenvoorden et al. [10] and Ribeiro et al [74]. After a short discussion of the mesh, convergence history and applied settings, the results are firstly validated by chordwise pressure distributions, overall C_L, C_D, thrust coefficients T_C and C_T and downstream total

pressure coefficient. Next the surface and volumetric flow fields of both the lifting surfaces as well as the propeller are visualised by Q-criterion iso-surfaces and wall shear. This sections ends with a comparison of the time-accurate flow field with the time-averaged flow in preparation for the next chapter and research questions in mind.

7.3.1. Simulation convergence and solving strategy

The propeller-wing-flap case is simulated at $\alpha = 8.3°$ by URANS. After an additional mesh refinement of the propeller wake, each of the 4800 time steps converged to a maximum $1e$-6 residual. A total of 60 propeller rotations, $0.36[s]$, are successfully simulated to allow the flow field to establish and converge to a semi-steady solution, similar to the approach of Roosenboom [12]. During the last 3 propeller rotations data sampling is applied to obtain time statistics of the unsteady flow field. The complete simulation required approximately 82,000 CPU hours, much less compared to the case 1b $11°$ simulation, 322,560 hours, due to the better convergence of case 2, significantly reducing the number of iterations per time step, and the application of first-order discretization during the first propeller rotations, allowing larger initial time steps.

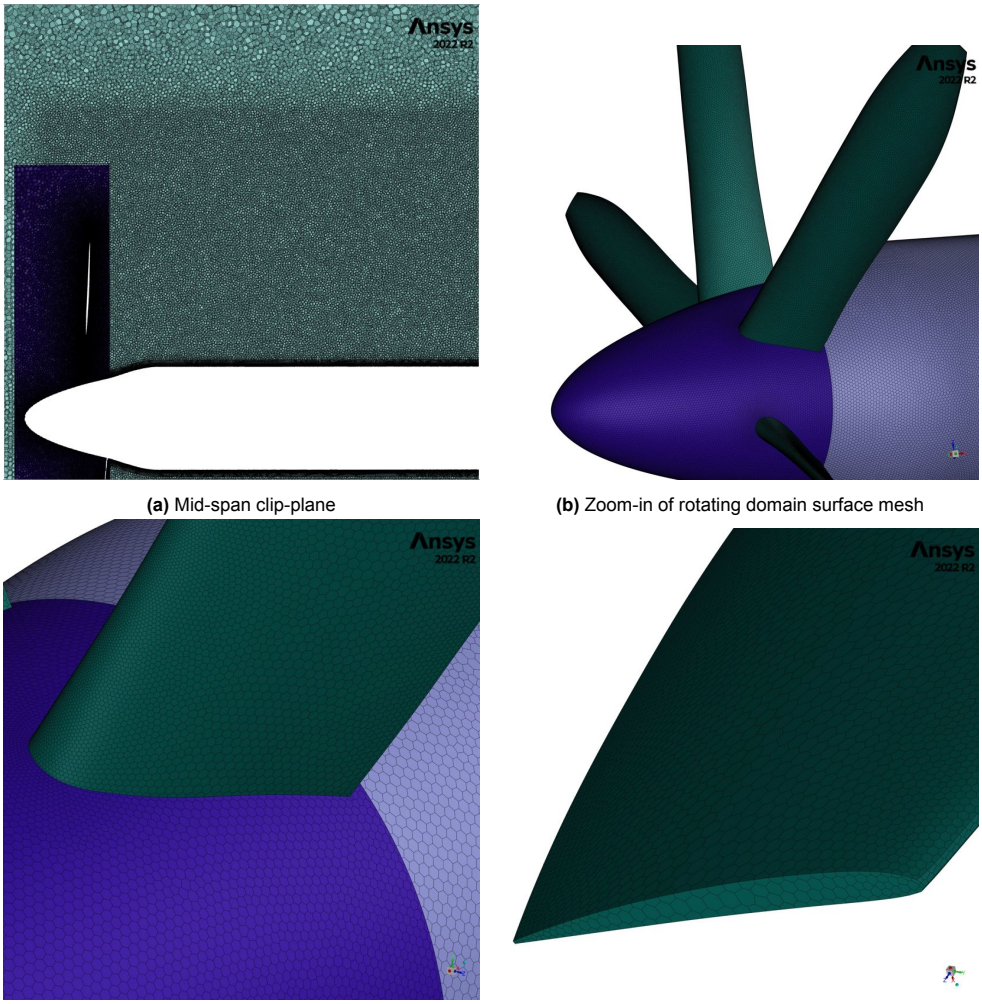

(a) Mid-span clip-plane

(b) Zoom-in of rotating domain surface mesh

(c) Zoom-in of hub-propeller intersection

(d) Zoom-in of propeller tip

Figure 7.14: Meshing of case 2.Total of 190 million polyhedral cells.

The meshing of case 2 is shown in Figure 7.14. The rotating domain consists of 19 million cells, yet the meshing does not capture the propeller blade leading edge curvature accurately in the blade tip regions. Unfortunately further mesh refinements where not possible due to computational resources, yet the marginal mesh in the propeller tip regions does not seem to negatively affect results. All surfaces adhere to the $y^+ \leq 5$ requirement. The convergence history in Figure 7.15 shows 3 timestamps, depicted by the green lines, at which large changes are made in the solving strategy.
The first few propeller rotations are solved with a first-order scheme and small time step starting at $1\text{e}{-8}$ $[s]$, slowly increased to the final time step of $3.5\text{e}{-5}$ $[s]$, equalling $\approx 2°$ propeller rotation. After 4 rotations a second-order scheme is selected for the spatial discretization. Preliminary results after 33 rotations showed excessive numerical diffusion, after which the propeller wake mesh is refinement. After 55 rotations also a second-order scheme for temporal discretization is selected. Earlier selection of this scheme was not possible due to initial RAM limitations. The impact of temporal discretization scheme is visualised in Figure 7.16. It is clear that the second-order result shows much less numerical diffusion compared to the first-order result.

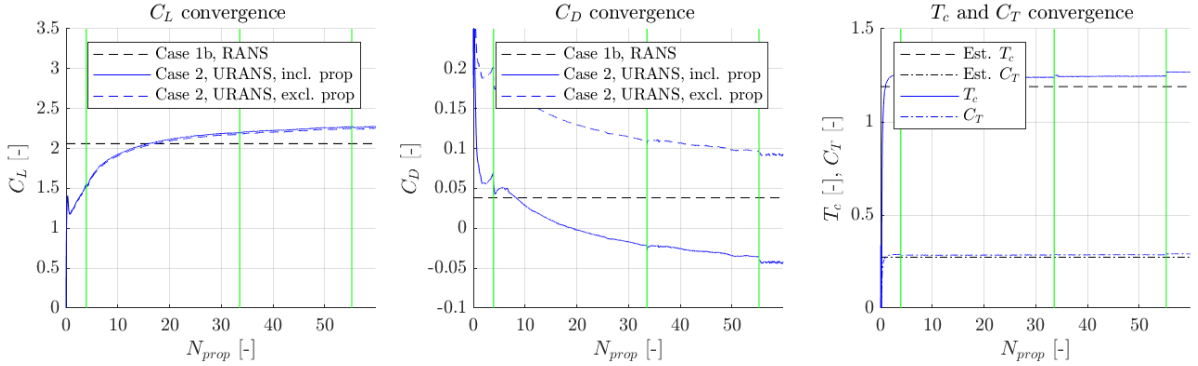

Figure 7.15: Convergence history of case 2. Green lines depict timestamps at which significant changes in mesh or solving settings are made. 'Incl. prop' denotes C_L and C_D of full geometry, 'excl. prop' denotes C_L and C_D from nacelle, wing and flap only. Direct forces of the propeller and hub surfaces are not included in the latter.

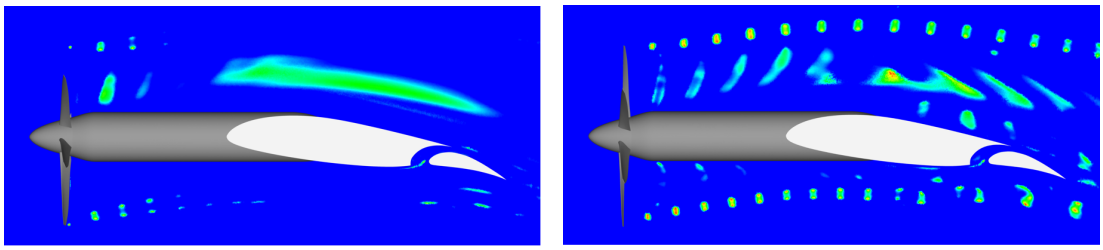

(a) First-order temporal discretization **(b)** Second-order temporal discretization

Figure 7.16: Normalized Q criterion contours to visualize the effect of temporal discretization on numerical diffusion of case 2.

7.3.2. Obtained lift, drag and propeller thrust

The converged values of C_L, C_D, T_C and C_T are shown in Table 7.3 and compared to case 1a and 1b $8.3°$ results and Duivenvoorden. As the convergence history of the obtained C_L, C_D and propeller thrust coefficients shows fluctuations due to the propeller phasing, the average amplitude of those fluctuations is included. Note that Duivenvoorden his advance ratio was set to 0.8 and his C_L values of case 1a and 1b are under predicted w.r.t to Boermans as discussed in Section 7.1. Although the C_L results of case 2 show the same trends at the blade-up and blade-down side as Duivenvoorden, the obtained values are approximately 15% lower, which is unexpected considering the results of case 1a an 1b and the higher thrust setting of current simulation. The obtained C_D values are underestimated to Duivenvoorden but show correct trends. The expected T_C of current simulation at $J = 0.765$ was 1.19 based on isolated propeller experimental measurements, Figure 6.4. The slightly higher obtained

		Present research	Duivenvoorden (*)
Case 1a	C_L	2.12	1.98
	C_D	$3.02 \cdot 10^{-2}$	$3.18 \cdot 10^{-2}$
Case 1b	C_L	2.06	1.90
	C_D	$3.82 \cdot 10^{-2}$	$-6.71 \cdot 10^{3}$
Case 2	C_L	2.27+/-0.005, full geometry	
		2.38, blade-down side	2.74, blade-down side
		2.62, blade-up side	3.06, blade-up side
	C_D	$9.20 \cdot 10^{-2}$+/-$0.02 \cdot 10^{-2}$, full geometry	
		$34.1 \cdot 10^{-2}$, blade-down side, pressure drag only	$42.4 \cdot 10^{-2}$, blade-down side, pressure drag only
		$9.25 \cdot 10^{-2}$, blade-up side, pressure drag only	$17.6 \cdot 10^{-2}$, blade-up side, pressure drag only
	T_C	1.267+/-0.003	1.05 (J=0.8)
	C_T	$2.913 \cdot 10^{-1}$+/-$0.002 \cdot 10^{-1}$	

Table 7.3: Comparison in C_L and C_D of case 2 to experimental Duivenvoorden data and case 1a and 1b. (* Duivenvoorden results are measured at two spanwise locations (average is shown for case 1a en 1b) and only pressure drag is measured.)

value of 1.267 can be explained by the angle of attack setting but also the upwash of the wing on the propeller, both effects increasing propeller thrust as explained in Sections 2.2.2 and 2.3. The obtained T_C, calculated by analysing the forces on the propeller and spinner only, is therefore accepted, but the deviations of C_L and C_D require further validation. The spanwise C_l and $C_{d_{press}}$ distributions are shown in Figure 7.17, showing complex spanwise variations which do not let themselves easily compare with similar distributions from literature due to the complex geometry, applied approach and operating conditions. However, the increase in lift due to the propeller induced increased dynamic pressure is clear, with a dip near the nacelle centerline shifted to the blade-up side. One reason for the relative high $c \cdot C_l$ at the blade-down side is the asymmetric blade loading of the propeller due to the upwash of the wing and high angle of attack, increasing propeller blade effective angle of attack more on the blade-down side compared to the blade-up side. This increases flow velocity on the blade-down side, hence lift on the downstream main wing, compared to the blade-up side, as shown by the axial velocity in Figure 7.19b.
The increased effective angle of attack at the blade-up side, reduced effective angle of attack at the blade-down side and overall asymmetric propeller blade loading are also likely the cause of the large asymmetry in pressure drag. The surface C_p distributions in Figure 7.23 clearly shows an increased suction peak at the blade-up side main wing leading edge, reducing pressure drag, and increased pressure at the blade-down side, increasing pressure drag.

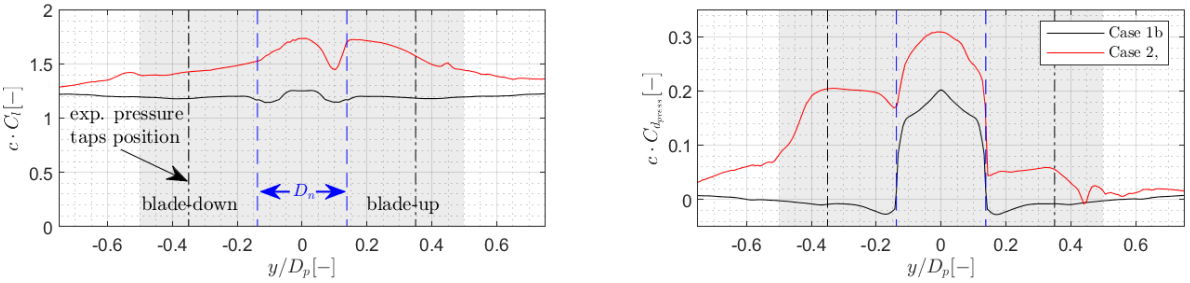

Figure 7.17: Case 2, spanwise lift and pressure drag distribution

7.3.3. Wake total pressure coefficient

To further investigate and validate correct propeller slipstream development, the current results are compared with Duivenvoorden his experimental wake rake measurements, shown in Figure 7.18b, and secondary with Ribeiro his Lattice-Boltzmann simulation results, Figure 7.18a. The total pressure coefficient is visualized, defined as $C_{p_t} = (p_t - p_\infty)/q_\infty[-]$. As a propeller adds energy to the flow, areas of $C_{p_t} > 1$ are indicative of the propeller slipstream and used to validate that current research accurately solves the downstream slipstream deformation. The wake rake is located 1 chordlength downstream of the flap trailing edge. A plane at the same location is implemented during CFD post-

processing.
In general, very good agreement with Duivenvoorden is observed considering the small differences in operating conditions. The slipstream deformation is a direct result of the propeller-wing interaction and therefore a important metric of current work. Yet some observations should be explained. For example, the non-smooth contour lines in Figure 7.18c are a direct result of the relative course mesh downstream of the PWF geometry, yet the general trend is clear. The main difference is the slightly higher total pressure coefficient in the center of the typical inverted T-shaped slipstream due to the lower advance ratio, hence increased thrust coefficient, of the CFD setup. Is is assumed that due to the same reason the bottom half of the slipstream at +/- 1.5 y/R shows a slightly larger deformation in spanwise direction compared to Duivenvoorden, although the slipstream in these regions interacts with the wing wake, challenging the identification of the propeller slipstream edge [10].

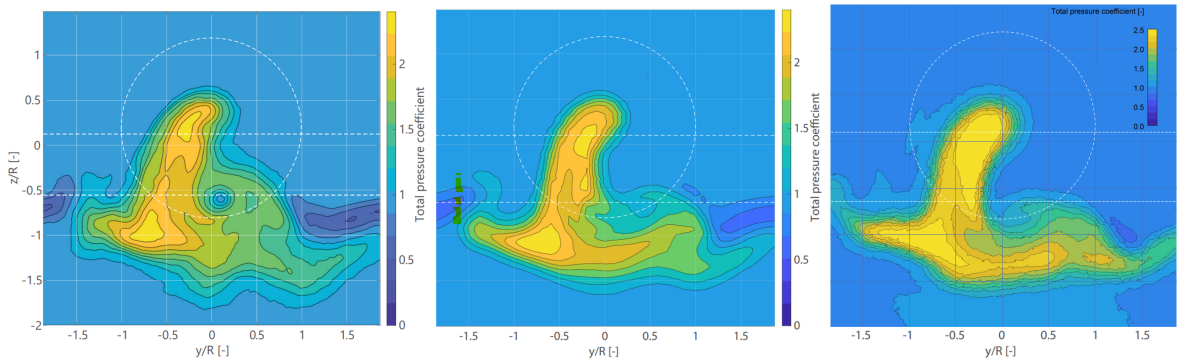

(a) Ribeiro [74] Lattice-Boltzmann CFD results $\alpha = 8.0°$, $J = 0.8$, $\delta_f = 15°$

(b) Duivenvoorden [10] wake rake results $\alpha = 8.0°$, $J = 0.8$, $\delta_f = 15°$

(c) Current research CFD results $\alpha = 8.3°$, $J = 0.765$, $\delta_f = 15°$

Figure 7.18: Total pressure coefficient plane, 1 flap-nested chordlength downstream of flap trailing edge ($x/c = -2$). Dashed lines indicate propeller disk, main wing leading edge and flap trailing edge.

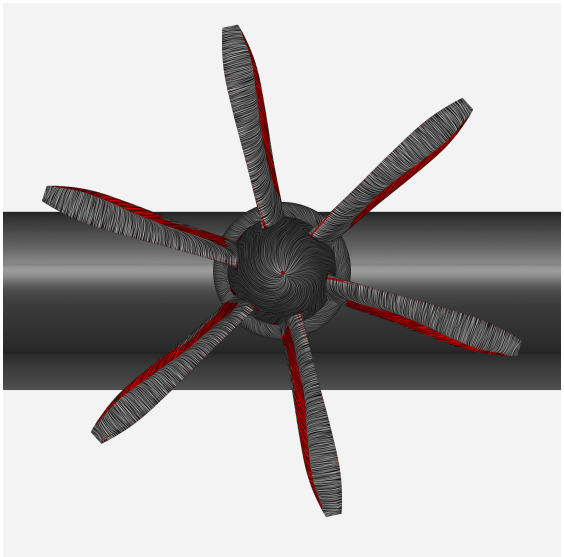

(a) Case 2, zoom in on frontal view of propeller. LIC, colored by surface shear stress in upstream x-direction. Red areas indicates areas of flow reversal.

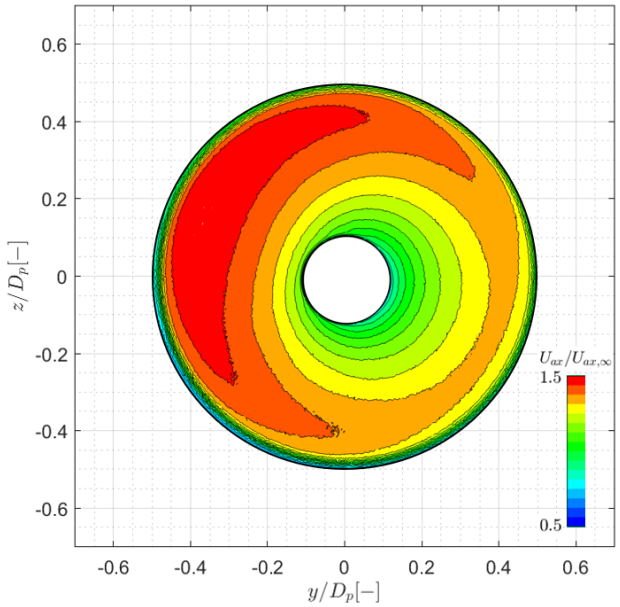

(b) Time-averaged axial velocity profile of propeller

Figure 7.19: Propeller flow field

7.3.4. Propeller surface flow field and axial velocity distribution

The propeller and hub surface flow field is visualised in Figure 7.19a by LIC, with reversed flow regions colored in red. The centrifugal forces due to the propeller rotation pushes the boundary layer to the

tip regions. The corresponding Himmelskamp effect, discussed in Section 2.2.1, can unfortunately not prevent the significant regions of flow reversal. These regions are however expected because the selected blade pitch setting and advance ratio do not coincide with optimum propeller efficiency at J=1.0, see Figure 6.4 of the isolated propeller data. For the same pitch angle and free stream velocity, the angle of attack of a propeller blade section increases with reducing advance ratio, accelerating flow separation.

7.3.5. Contours of shear stress and pressure coefficient.

Surface shear stress

Good agreement is observed between the CFD shear stress contours in Figures 7.20a and 7.21 and the oil flow visualisations of Figure 7.20c. The spanwise extend of the propeller slipstream on the wing suction side to the down-going blade side is clearly visible, while the pressure side shows spanwise slipstream displacement to the blade-up side. The cause of this spanwise slipstream shift is explained by considering the spanwise shear distribution, Section 2.3.3. Note how the increase of C_l at the blade-up side is indeed shown in the spanwise lift distribution of the earlier discussed Figure 7.17. The flap leading edge encounters the wing pressure side wake, resulting in the flap region affected by the propeller slipstream shifted to the blade-up side as well.

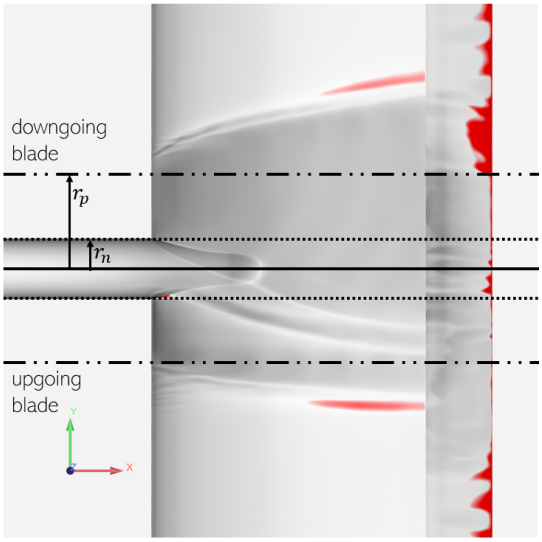

(a) Suction side, colored by x-shear

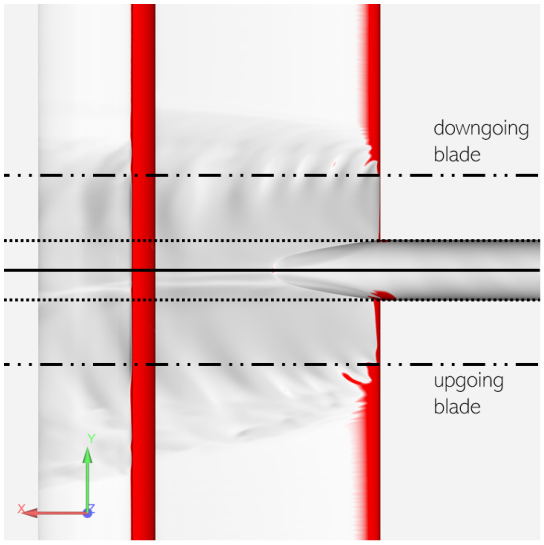

(b) Pressure side, colored by x-shear

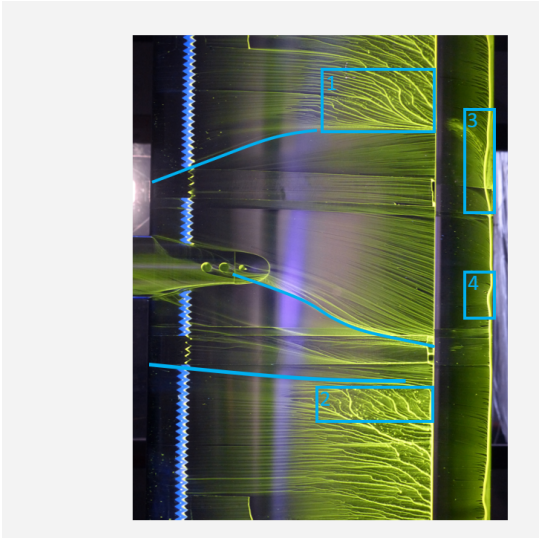

(c) Suction side, edited from Duivenvoorden

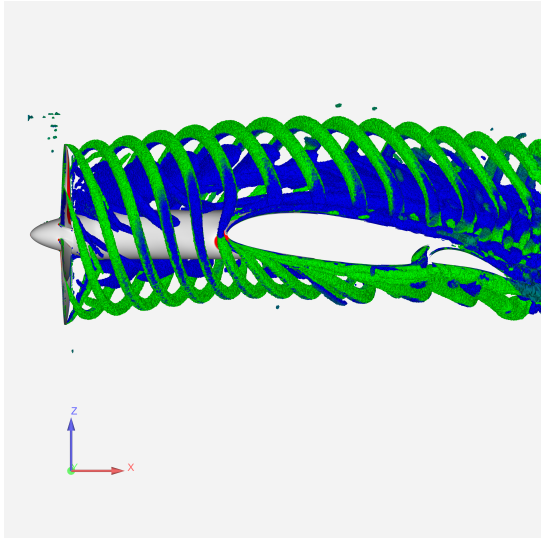

(d) Side view, Q-criterion iso-surface colored by x-vorticity

Figure 7.20: Case 2, various illustrations of surface and volumetric flow field.

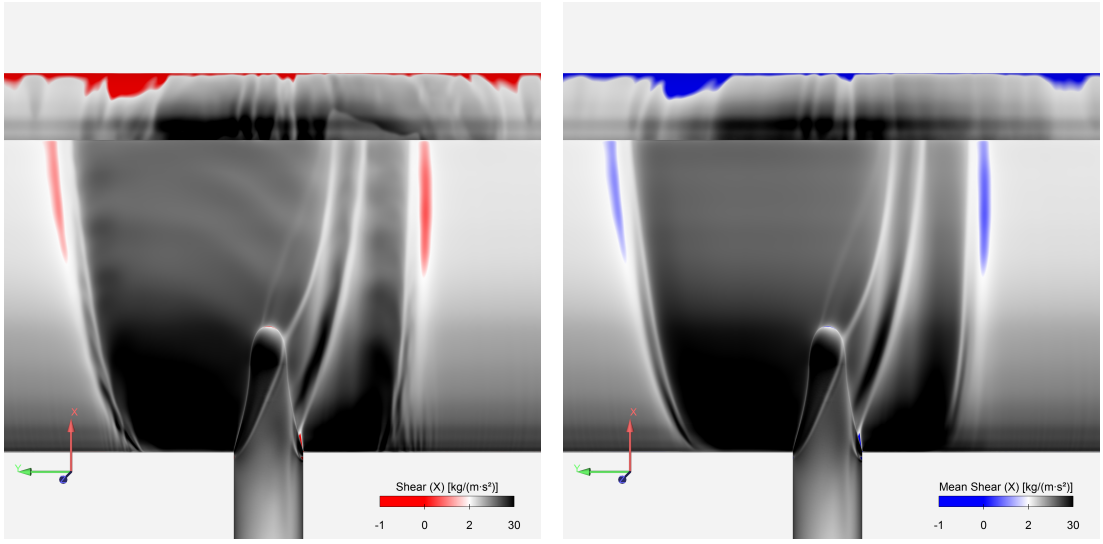

(a) time-accurate, suction side

(b) time-averaged, suction side

Figure 7.21: Case 2, surface shear stresses in x-direction, clipped to domain near 0 $[Pa]$. time-accurate versus time-averaged.

The experimental results of Duivenvoorden shows two regions on the wing suction side that approach stall just outside the propeller slipstream affected area, depicted by numbers 1 and 2 in Figure 7.20c. The experimental results also shows two flow reversal regions on the flap, 3 and 4. The simulation shows areas with increased sensitivity to flow reversal in the same regions, but in a more chaotic pattern.

Time-accurate x-shear results are further compared with time-averaged results in Figure 7.21. The surface x-shear does not show large differences. The flow reversal areas at the flap are slightly less chaotic in the time-averaged representation. Note that at the leading edge-nacelle intersection at the blade-up side a small region of flow reversal exists due to a combination of the nacelle-wing suction peak interaction effects and the increased effective angle of attack at the blade-up side. The reduction of angle of attack at the blade-down side counteracts the angle of attack increase due to the nacelle, preventing flow separation.

The shear stress contours give sufficient confidence in the results. Present CFD results show very similar flow compared to the experimental results, which is quite remarkable given the URANS approach and complex flow phenomena. The Lattice-Boltzmann simulation of Ribeiro [74], for example, did not show the approaching flow separation zones just outside of the propeller slipstream.

Surface pressure coefficient

The biggest difference between the time-accurate and time-averaged chordwise pressure distributions of Figure 7.22 is seen at the pressure side. Trends of the obtained average chordwise C_p distribution nicely agree with the results of Ribeiro. These results are not shown due to the slightly different angle of attack of $8°$, resulting in an offset of the pressure distribution. The large fluctuations at the pressure side are further quantified by the RMSE of C_p in Figures 7.23e and 7.23f. The main reason of these fluctuations is the close proximity of the propeller tip vortices due to the high angle of attack setting, pushing the tip vortices close the the wing surface increasing it's effects on C_p, see Figure 7.20d. Near the wing leading edge, only little distinct propeller tip vortices interactions are seen, denoted with the white arrows in Figure 7.23b. Only relative small normalized RMSE's up to 10% are seen at the wing suction side, while the pressure side shows fluctuations in C_p exceeding 100%. The high RMSE at the the spinner and propeller blades is caused by the asymmetric propeller inflow conditions.

At last, in the simulation of Ribeiro [74] it was identified that the tip vortex of the propeller does not split at the wing leading edge, but stretches around it. The Q-criterion iso-surfaces remain mostly intact in the regions of interest and as such the same stretching of the tip vortex is seen in Figure 7.20d.

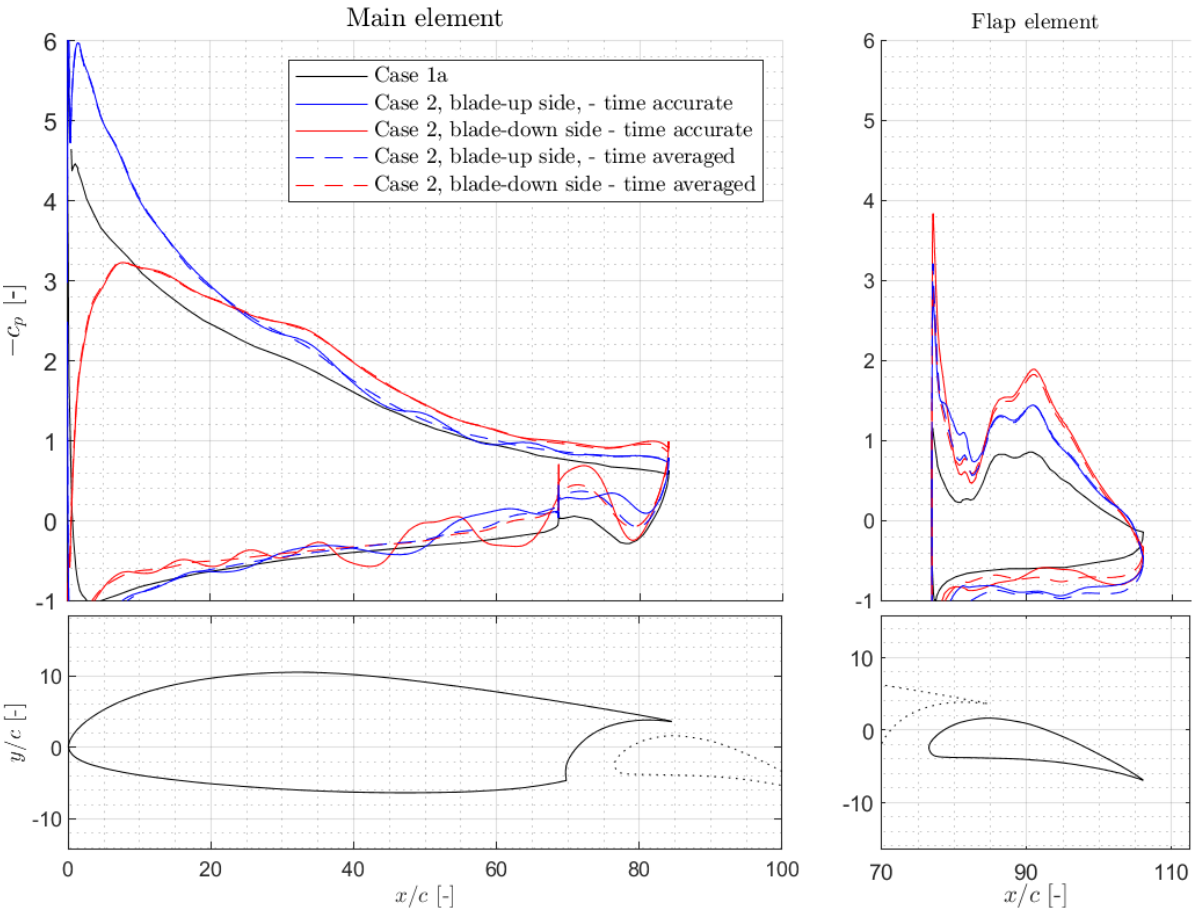

Figure 7.22: Case 2, chordwise pressure coefficient distribution at +/- $0.35D_p$, time-accurate versus time-averaged.

This concludes the verification and validation of case 2. Although the C_L is smaller than expected, overall results agree very well with Duivenvoorden [10] and Ribeiro [74]. Time dependent effects are shown to occur and well sampled in the simulation software. The next section briefly recaps the verification and validation findings of this chapter before further analysing the flow of the propeller-wing-flap setup in Chapter 9.

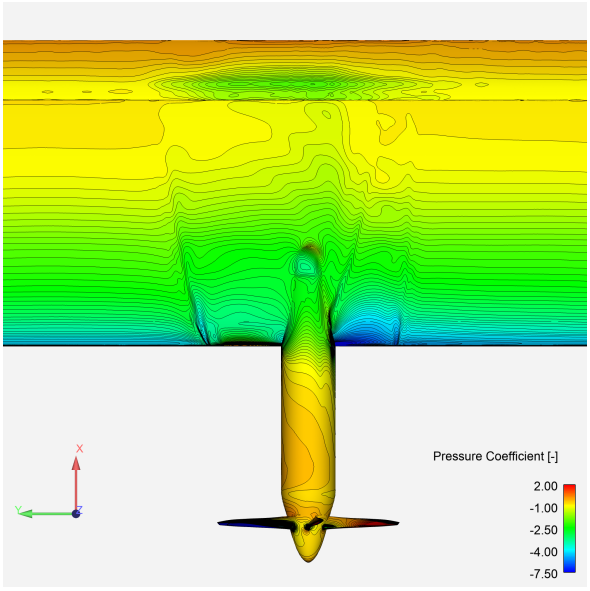

(a) time-accurate C_p [-], suction side

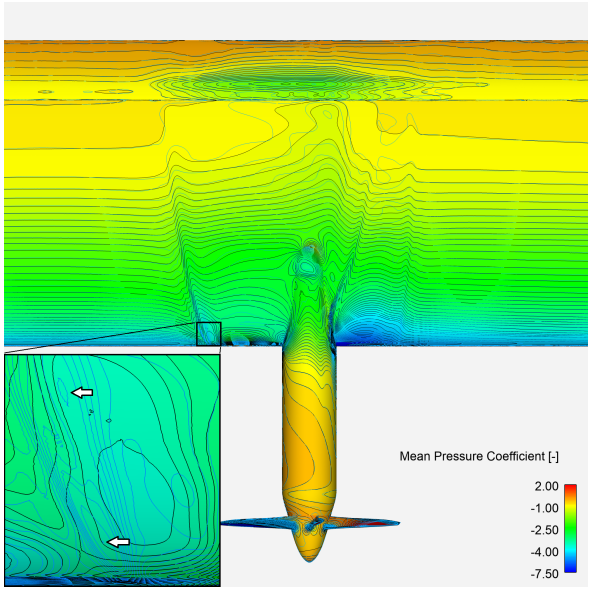

(b) time-averaged C_p [-], suction side, overlapped with blue contours showing time-accurate result.

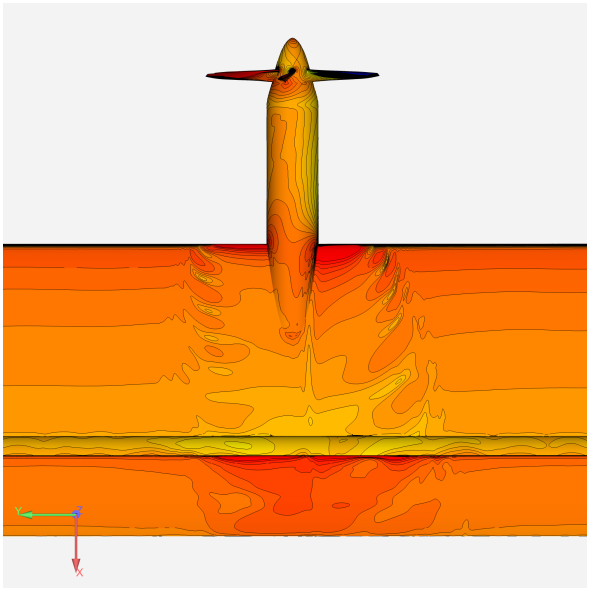

(c) time-accurate C_p, pressure side

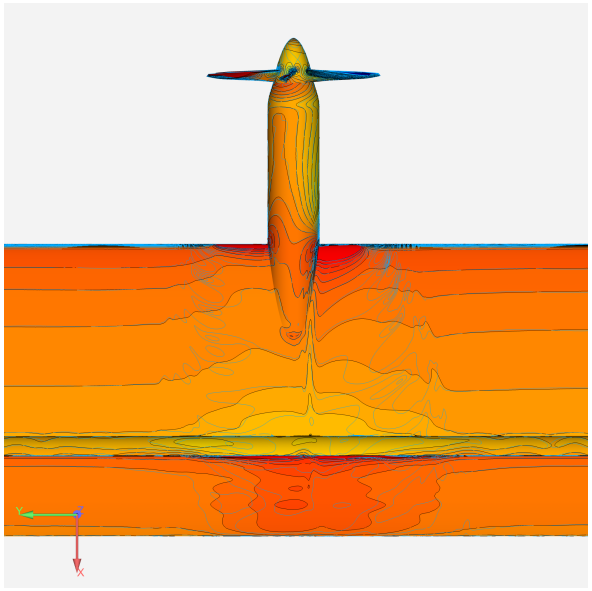

(d) time-averaged C_p [-], pressure side, overlapped with blue contours showing time-accurate result.

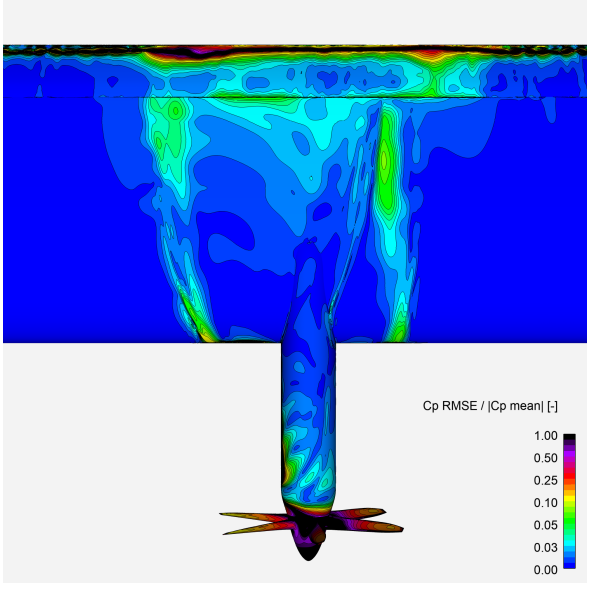

(e) RMSE of C_p [-], non-dimensionalized with $|\bar{C_p}|$ suction side. Note the non-linear scale

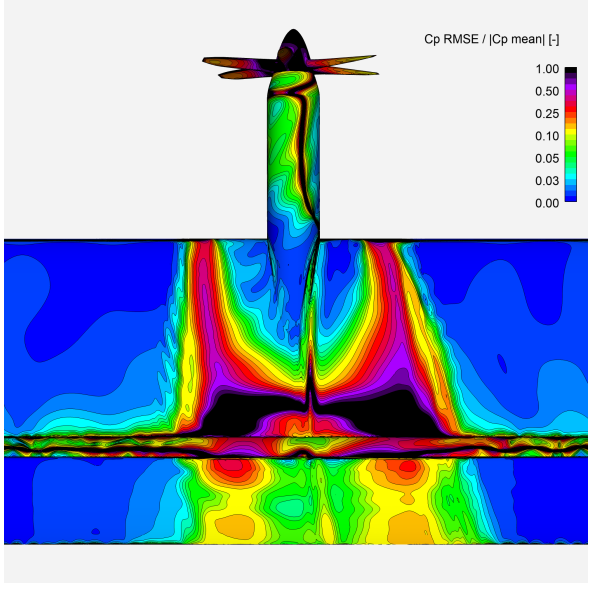

(f) RMSE of C_p [-], non-dimensionalized with $|\bar{C_p}|$ pressure side. Note the non-linear scale

Figure 7.23: Case 2, Surface pressure coefficient distribution, time-accurate versus time-averaged and RMSE.

7.4. Conclusion

In Chapter 7 results of case 1, wing-flap, case 1b, nacelle-wing-flap and case 2, propeller-wing-flap, are discussed in order to:

- **verify** applied meshing and solving techniques, and
- **validate** CFD results with experimental data by a quantitative comparison with Boermans et al. [20], Ribeiro et al. [74] and Duivenvoorden et al. [10] for case 1a, and qualitative comparison with Duivenvoorden [10], Suard, [42], Van Anrhem [90], Qiu et al. [6] and Keller et al. [45] for case 1b. Case 2 has been validated by Duivenvoorden et al. [10], Ribeiro et al. [74] and Keller et al. [2].

All cases are solved by a SIMPLE 2^{nd} order algorithm. The selected SA turbulence model requirement of a y^+ of maximum 5 is adhered to in all cases. Velocity and turbulence profiles of case 1a shows sensible trends and do not seem negatively affected by the large growth rate from the inflation layer to bulk mesh cells. The propeller slipstream is well resolved, despite the marginal mesh in the propeller tip regions.

Case 1a converged to a max $1e$-6 residual at both angle of attacks of $8.3°$ and $11°$. The case 1b RANS solution at $8.3°$ only loosely converged to a max $1e$-4 residual while the $11°$ showed insufficient convergence and a nonphysical solution. The $11°$ 1b case is therefore successfully solved by URANS following the recommendations of Rumsey [51], showing a max order $1e$-6 residual at each time step.

Case 1a shows good agreement with Boermans w.r.t. C_L with a maximum error of $+0.42$% at α=$11°$, which is also represented by the well-matching chordwise C_P distribution. One remarkable difference in the C_P distribution compared to Boermans are dips in the flap suction-side pressure distribution. The same dips are however also seen in the results of Ribeiro as a result of the fully-turbulent flow assumption in the Lattice-Boltzmann simulation. Current RANS simulation also assumes fully-turbulent flow. The solution is therefore accepted.
An error in C_D up to $+20.9$% is found compared to Boermans, which did not reduce with further mesh refinements. A possible reason might be that Boermans did not apply forced transition in his setup, reducing drag due to improved laminar flow.

Case 1b is successfully solved at both angles of attack. The trends in C_L are equal to the trends of Duivenvoorden his results. One interesting result of Duivenvoorden was a negative pressure drag at $8.3°$. The present CFD results have confirmed that this is due to the nacelle suction peak that coincides with the experimental pressure taps. While the pressure drag is negative at this spanwise location, the overall pressure drag is positive. With this in mind, also the C_D results are accepted.

Flow separation is seen at the nacelle-wing intersection, consistent to Duivenvoorden. The maximum spanwise extend of flow separation in the CFD results matches the experimental results for the RANS $8.3°$ solution. Due to the relative difficult convergence of case 1b at $11°$ while no new flow phenomena are revealed, it is decided to run case 2 at $8.3°$ settings. Based on the current results this setting is acceptable to answer the research questions with.

Case 2 is successfully simulated with a second-order discretization scheme for both the temporal as spacial discretization. The obtained overall C_L of 2.27 is lower than expected, but trends in C_L and C_D are correct. Chordwise C_p distributions match well with Ribeiro. The slightly high T_C is explained by the low advance ratio compared to Duivenvoorden and Ribeiro and the angle of attack setting, increasing propeller thrust. Due to the low advance ratio of 0.765 compared to the optimal advance ratio of 1.0 trailing edge flow separation is seen at the propeller by cause of the high angle of attack. Downstream total pressure coefficient contours match great with Duivenvoorden. The same is true for separation-sensitive areas at the lifting surface suction sides. Present results correctly predict flow separation w.r.t. Duivenvoorden his experiment, although the separated areas are slightly chaotic compared to the smooth separation lines seen in the experimental results. Time-dependent flow phenomena are well captured by the simulation, such as time-varying chordwise pressure distributions and surface shear stresses. The current case is well validated to continue with the goal of this report in the next chapter.

Part III

Results

8

Results of the Nacelle-Wing-Flap Case

This chapter offers a detailed examination of the flow phenomena taking place in the nacelle-wing-flap setup. Previous chapter showed a complex surface flow field. In this chapter the volumetric flow field is visualised to enhance understanding of the flow in preparation for the propeller-wing-flap case. This is done by identifying the four unfavorable effects of nacelle-wing interaction as discussed by Qui et al. [6].

Section 8.1 discussed the RANS results at the $8.3°$ angle of attack setting. The URANS results at $11°$ angle of attack is discussed in Section 8.2.

8.1. Angle of attack 8.3 degrees

Qiu et al. [6] (Figure 2.6b) identified four unfavorable effects of nacelle-wing interaction, recapped in Figure 8.1:

1. High-Pressure flow expand effect on upper surface of main wing,
2. Boundary-layer accumulation effect on upper surface of main wing,
3. Local angle of attack increasing effect caused by engine nacelle,
4. Dual-wall surface friction effect at the intersection corner.

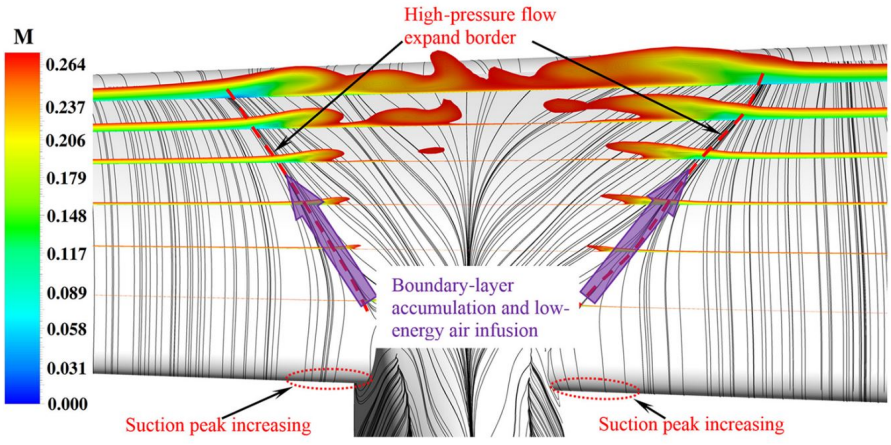

Figure 8.1: Unfavorable effects of nacelle-wing interaction [6]

All four effects are resolved in the present simulation and examined by multiple figures. Figure 8.2, showing surface contours of C_P and volume Mach-contour clip planes, is used to identify the four unfavorable effects while Figure 8.4 further examines the 3D flow field by streamlines.

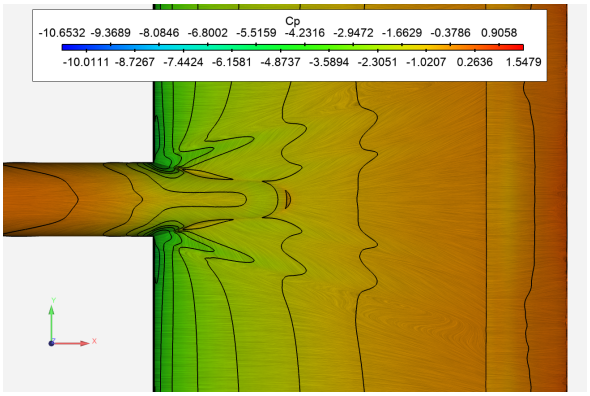

(a) C_p contour with shear stress LIC

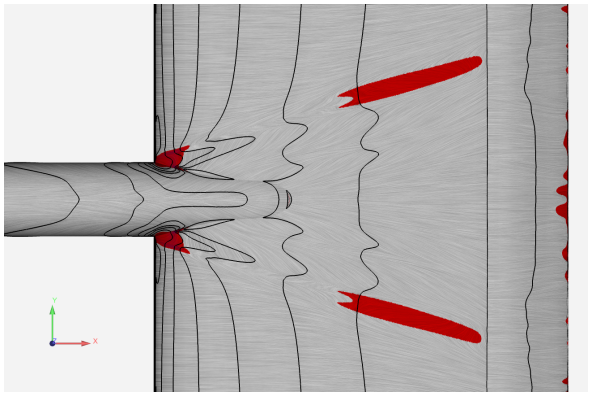

(b) C_p contour with shear stress LIC. Red indicates negative shear in upstream direction, indicating areas of flow separation.

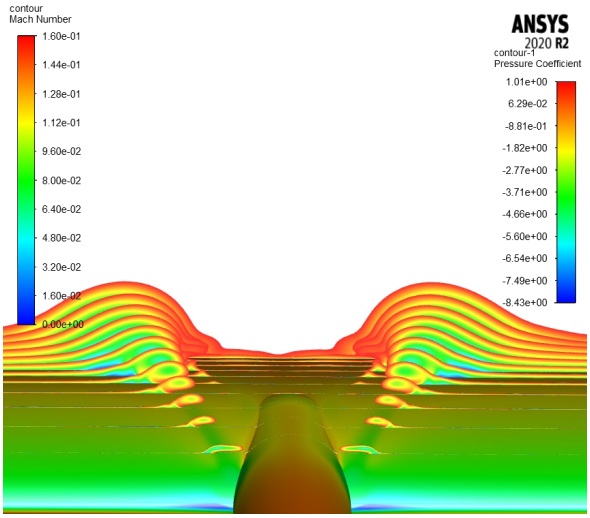

(c) Surface C_p contour with volume contour clip-planes colored by Mach-number, indicating boundary layer thickening.

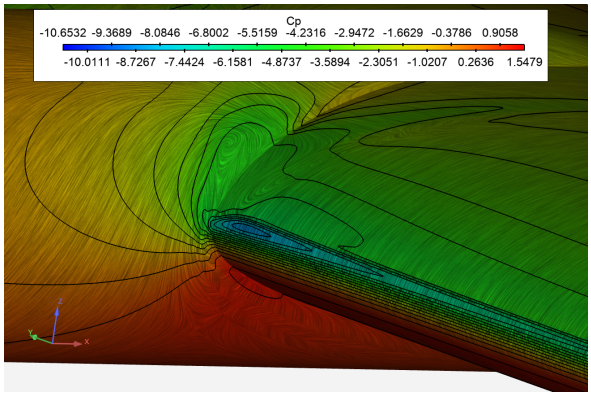

(d) C_p contour with shear stress LIC, close-up of nacelle-wing intersection suction peak.

Figure 8.2: Case 1b, $\alpha = 8.3°$, surface contours of C_p, shear stress and volume Mach-contours.

The first effect of Qiu is clearly visible in Figure 8.2a. The shear stress line integral convolution (LIC) shows the expending flow downstream of the nacelle. The second effect is visualised in Figure 8.2c, in which spanwise mach contour plots are shown, clipped to the free-stream velocity. The nacelle-wing intersection suction peak is visible already in this figure while Figure 8.2d provides a zoomed-in view to further confirm the third effect. The suction peak increased from a minimum C_P of -6.0 in case 1a, to -8.4 in case 1b as shown in Figure 8.3. The fourth effect locally reduces stall performance, clearly shown by the red symmetric reversed-flow areas downstream of the nacelle in Figure 8.2b.

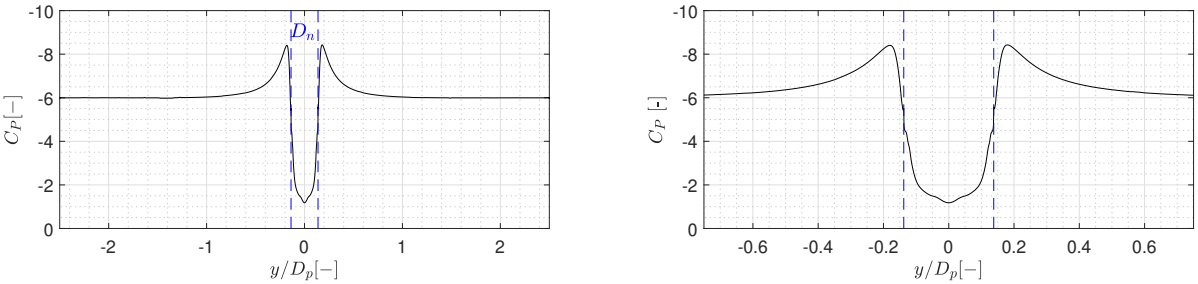

Figure 8.3: Case 1b spanwise distribution of pressure coefficient C_p at main wing leading edge. $\alpha = 8.3°$. Dotted blue lines indicate diameter of nacelle D_n. The C_P between the blue lines shows the nacelle upper-side C_P.
Left: full spanwise domain. **Right:** zoom-in.

Flow separation is also seen at the nacelle-wing intersection, consistent to the experimental oil flow simulations and the leading edge separation bubble described by Qui et al. [6]. This flow separation is further visualized by streamlines in Figures 8.4a and 8.4b, showing a good resemblance with the results of Van Arnhem [7], Figure 2.8. Note how from this separated area vortices escape, following the divergent flow pattern, leading to a reversed flow region above the flap.

Figure 8.4a further illustrates the origin of boundary layer thickening: the nacelle vortex is colored in blue (1) and significantly contributes to the boundary layer thickening. The orientation of the vortex rotation leads to low momentum flow downstream of the nacelle being transported outboard to the upwash side of the vortices, weakening and thickening the boundary layer by this spanwise flow component and expediting flow separation as identified by Keller et al. [45]. Furthermore, the reduced velocity at the position *"of the vortex core is caused by dissipation due to the high shear stresses within the vortex. As the vortex loses its strength and the static pressure within the core begins to rise,the velocity deficit due to the total pressure losses becomes evident"* [45].

A less intense boundary layer thickening is seen closer to the nacelle centerline, originating from the nacelle-only flow colored in red and guided by the slightly concave curvature of the nacelle-wing intersection near 20% chord. Also note that while flow near the surface diverges due to the high pressure region, the yellow (2) streamlines converge back to the nacelle centerline. At the same time it is seen that flow near the surface diverges away from the nacelle centerline due to spanwise pressure gradient. The diverging flow near the surface and the converging flow away from the surface might further increase the vorticity originating from the wing-nacelle intersection.

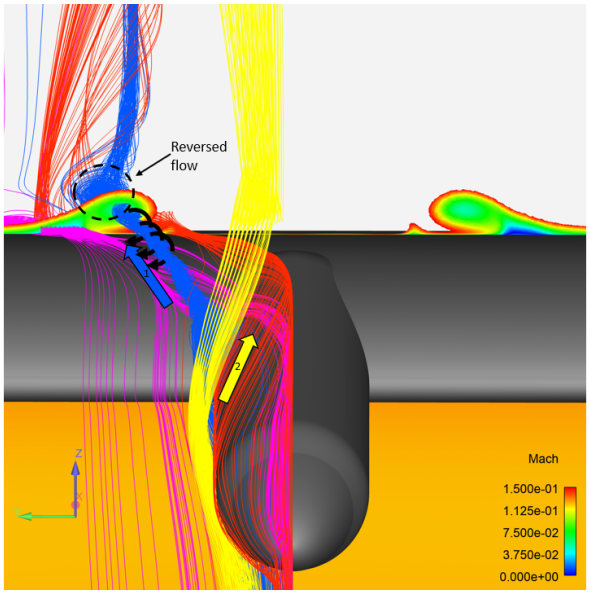

(a) Flow streamlines, colored by regions of interest. Note the significant vortex from the nacelle-wing intersection, the divergent flow pattern near the surface and the convergent flow pattern downstream of the nacelle away from the surface.

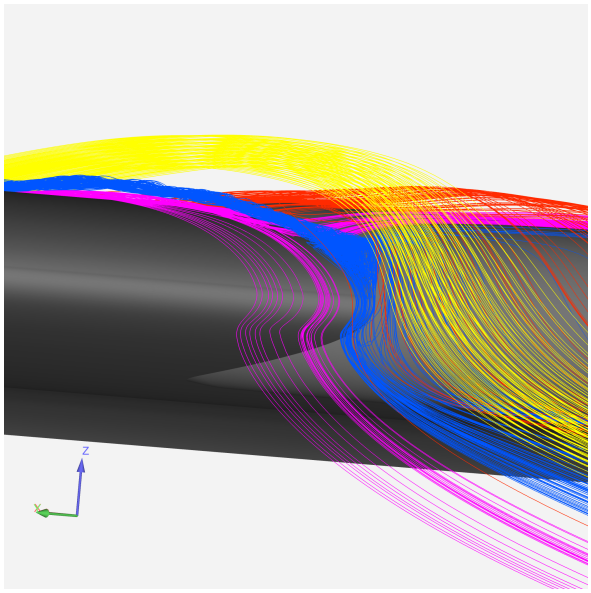

(b) Zoom-in nacelle-wing intersection. Note the leading-edge separated flow region, corresponding to the red sections in Figure 8.2b

Figure 8.4: Case 1b, $\alpha = 8.3°$, streamlines and shear LIC and single mach-contour plot near main wing trailing edge.

8.2. Angle of attack 11 degrees

The time-accurate flow field of the URANS simulation at α=$11°$ is visualized in Figure 8.5 by surface shear lines, reversed flow regions and the normalized Q-criterion to visualise vortical structures. The surfaces shear lines show an overall similar pattern as at α=$8.3°$, although slightly more chaotic due to the time-accurate visualisation. For example, Figure 8.5a suggests that the separated flow cell at the wing leading edge - nacelle intersection, as a result of the local pressure peak followed by a high adverse pressure gradient, is moving downstream and diverging away from the nacelle centerline in a

periodic manner. The reversed flow areas near the wing trailing edge, marked by the red-dotted lines, show signs to extend all the way to the main wing trailing edge in a wedge-shaped pattern, which is not seen in the RANS $8.3°$ solution but clearly present in the $10°$ experimental results of Duivenvoorden in Figure 7.11 at starboard side.
Note that the areas of separated flow are outboard of the vortical structures. The orientation of the vortex rotation leads to high momentum flow being transported to the area downstream of the nacelle, and low momentum flow downstream of the nacelle being transported outboard to the upwash side of the vortices as also discussed in the previous section.

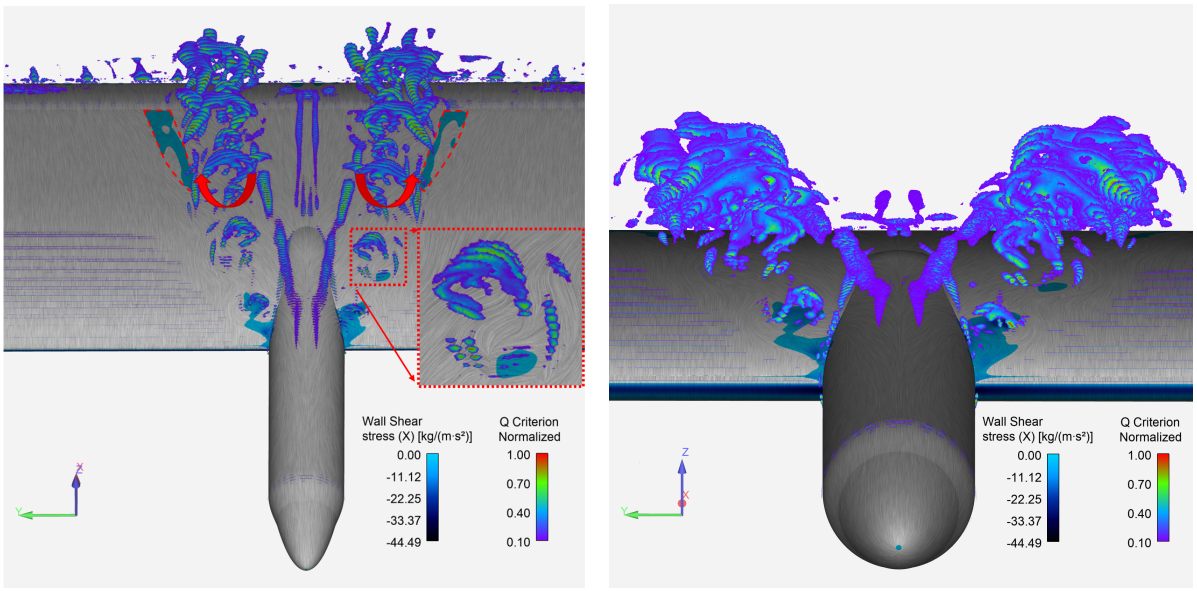

(a) **(b)**

Figure 8.5: Case 1b, $\alpha = 11°$, time-accurate flow field at $t = 0.4[s]$, shear LIC with reversed flow regions ($-x$) colored by blue, and chordwise clip-planes of normalized Q criterion to visualize vortices. Red arrows denote rotation direction of vortices.

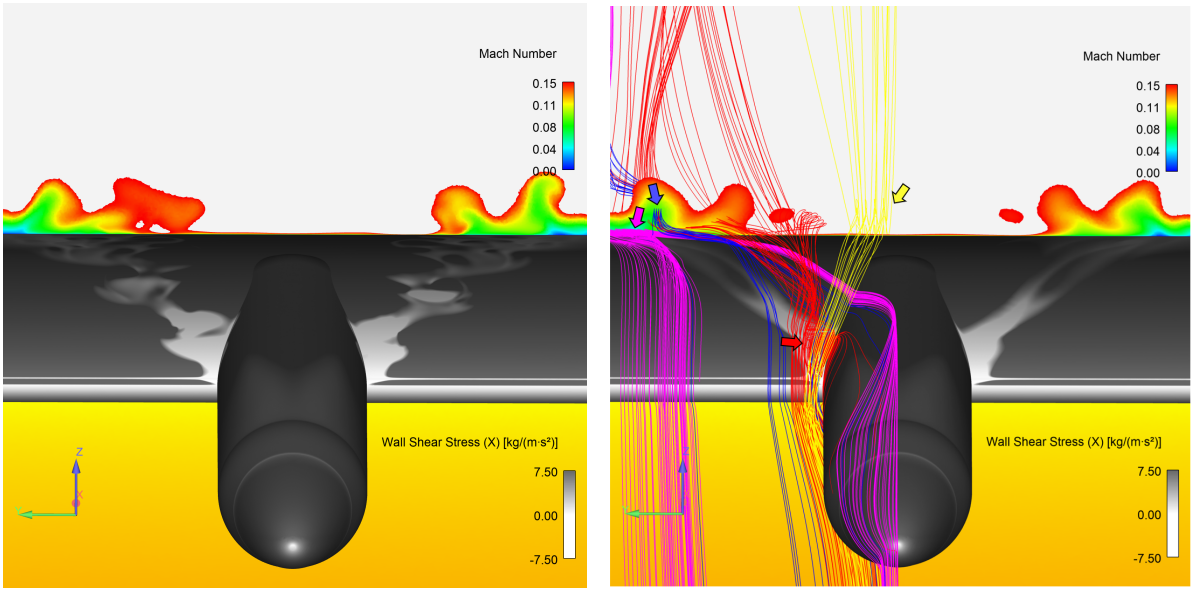

(a) Time-accurate mach clip-plane, clipped to free-stream $M = 0.15$.

(b) Time-averaged mach clip-plane, clipped to free-stream $M = 0.15$, and streamlines colored by regions of interest.

Figure 8.6: Case 1b, $\alpha = 11°$, comparison between time-accurate flow field and time-averaged flow field. Time-accurate flow shown at $t = 0.415[s]$. Time-averaged flow is sampled from $t = 0.4[s]$ to $t = 0.415[s]$ in time steps of $\Delta t = 2.5e\text{-}4$.

The mach clip-plane in Figure 8.6b is more chaotic compared to the 8.3° result in Figure 8.4, making it more difficult to identify the individual nacelle-wing interaction flow phenomena. This is confirmed by emitting streamlines from regions of interest, identified by the arrows. Although the streamlines follow the same trends as the RANS 8.3° solution, Figure 8.4a, some key flow phenomena are less clear. The vortex originating from the nacelle-wing intersection, for example, is indistinct. This contributes to the earlier mentioned smaller reverse flow regions on the wing surface in Figure 7.13d and it is expected that this is due to the averaging of the periodic vorticity shedding. Averaging the flow leads to less spanwise movement of low momentum flow, postponing separation.

9

Results of the Propeller-Wing-Flap Case

The validation results of case 2 showed many complex flow phenomena, but respective chapter primarily focused on comparing occurring flow phenomena with experimental and CFD results. Current chapter provides a closer look to propeller-wing-flap flow phenomena, with a focus on the time-dependent variation of the 3D flow field and its effect on the PWF surfaces. Time-averaged flow quantities are sampled by averaging the flow field of 3 propeller rotations.

Section 9.1 discusses the flow field up to the trailing edge of the main wing. The findings in this section shape the answer to the first sub-question. Section 9.2 provides a close look at the complex flow field of the flap to answer the remaining sub-questions.

9.1. Propeller, nacelle and main wing flow

Chapter 7 already discussed some results that will be referred to in current section, for example the surface C_p time-averaged, -accurate and -fluctuations of Figure 7.23 and side view Q-criterion iso-surfaces in Figure 7.20. This section continues with discussing observed flow phenomena, starting with identifying individual vortices and its influence on the main wing surface flow field.

9.1.1. Identification, origin and effects of vortex systems

The propeller slipstream is initially examined by Figure 9.1. The geometry is colored by wing shear, with regions of (approaching, see legend,) flow reversal colored by red, and regions of high downstream shear grey. Iso-surfaces of positive Q-criterion are shown, colored by x-vorticity to identify the rotational direction of shed vorticity. Note how this Figure 9.1 shows positive Q-criterion at the wing leading edge outside of the propeller slipstream region. The Q-criterion method is known to be limited w.r.t. filtering out the wing shear layer. The Q-criterion iso-surface value should be balanced to minimize the visualisation of the wing shear layer while maintaining the actual coherent vortical structures [36].
In this figure multiple vortex systems are clearly visible, such as the propeller tip vortex, near-root vorticity and the vortex systems originating from the wing-slipstream intersection. However, utilizing this visualisation approach makes it challenging to concentrate on specific elements of the flow or examine the interior of the propeller slipstream.

A low total pressure coefficient could indicate the presence of a vortex core. The viscosity in the vortex core dissipates energy, reducing C_{p_t}. streamlines are released in the downstream and upstream directions in regions of low C_{p_t} to identify the path and origin of the respective vortices. Figure 9.2a shows contours of total pressure coefficient at the main wing trailing edge suction side at the upper half of the figure, while the lower half shows C_{p_t} contours just upstream of the cove area at its pressure side. A total of six bundles of streamlines are released from low-C_{p_t} regions, as shown in Figures 9.2b and 9.2c. Just as in case 1b, nacelle-wing-flap, a large surface-normal variation in velocity vector is seen

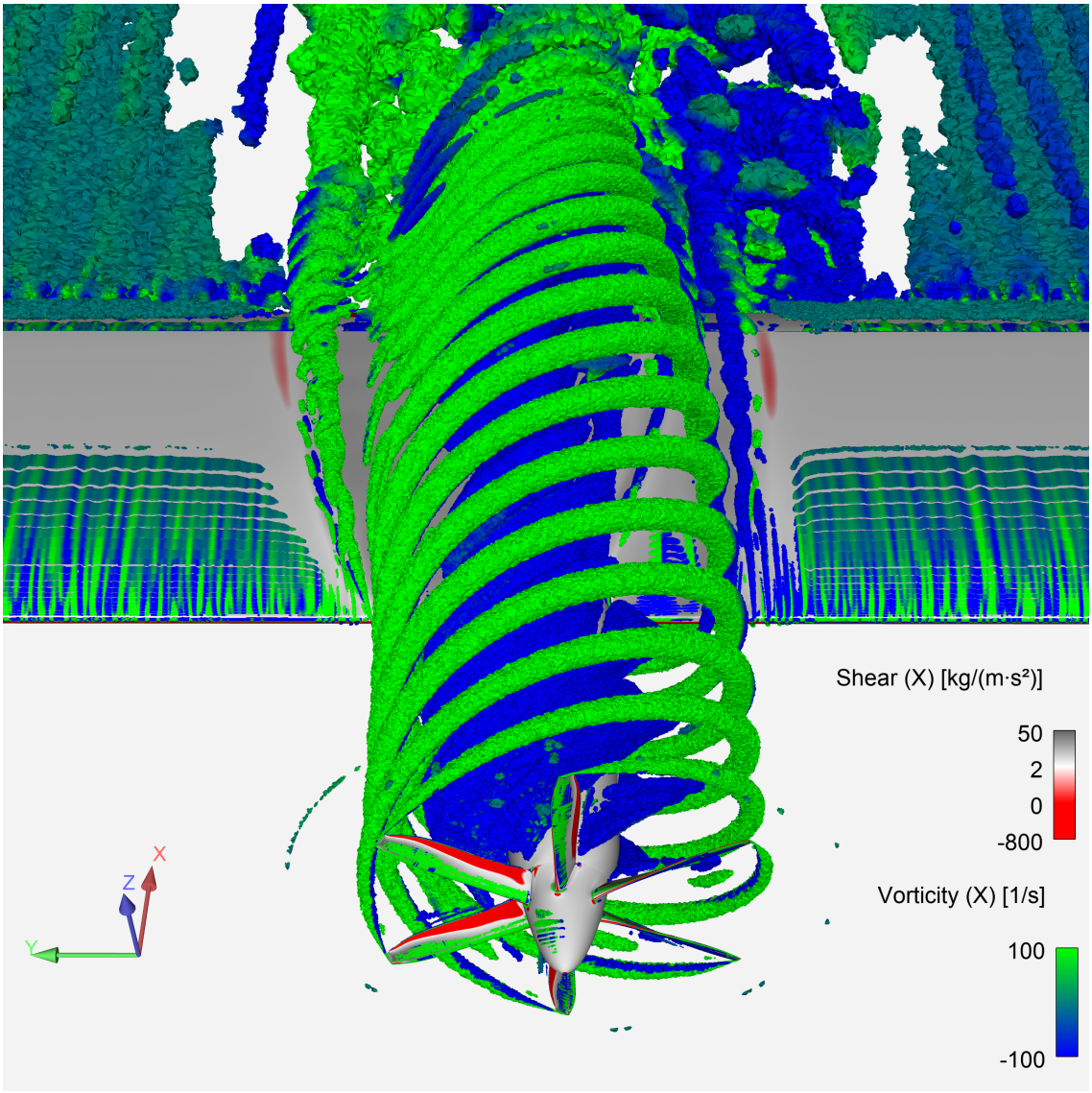

Figure 9.1: Case 2, general impression of 3D flow field by positive normalized 0.001 Q-criterion iso-surface, colored by x-vorticity, and surface shear stress in upstream x-direction. Red areas indicates areas of (approaching, see legend,) flow reversal.

near the nacelle centerline (red, green and cyan streamlines).

The red streamlines originate from the blade-up side propeller root sections and are seen to cluster to a condensed counterclockwise (negative x-vorticity) oriented vortex in Figure 9.3. The counterclockwise rotation of this vortex is believed to induce a local spanwise flow component to the blade-up side, denoted by the green streamlines in Figure 9.2b. At the pressure side a similar roll-up of flow to a vortex is seen for the purple streamlines, although these streamlines pass through the midsections of the propeller disk instead of the blade roots. The orientation of this vortex is the same as the one corresponding to the red streamlines, but being on the lower side of the wing it imposes a spanwise flow component to the nacelle centerline. This flow passes through the cove area to flap suction side and will be discussed in detail in Section 9.2.

The yellow streamlines correspond to a clockwise-oriented positive x-vorticity vortex, originating from the blade-down side propeller slipstream edge interaction with the main wing. The vortex imposes an spanwise up-flow at the outboard, low momentum, wing boundary layer as seen in Figure 9.2a and further illustrated by the black arrows in Figure 9.5. This leads to boundary layer thickening, accel-

erating flow separation as seen by the approaching stall region. The yellow vortex orientation could be connected to the increased angle of attack at the wing leading edge outside of the propeller slipstream as shown in Figure 9.4. This increased local angle of attack might also contribute to the flow separation regions. Furthermore, the spanwise $c \cdot C_l$ distribution discussed earlier (Figure 7.17) shows increased lift near the edges of the propeller slipstream corresponding to the mean-C_p offset (delayed downstream C_p increase), directly below the yellow streamlines as a result of the high rotational speed and low static pressure of the vortex core itself. Reduction of the surface C_p near off-the-surface vortices is also seen at the blade-up side, as well as on the wing pressure side (Figure 7.23d) near the purple streamlines of Figure 9.2c and the edges of the slipstream. The blade-up side flow separation zone is more forward and more intense compared to the blade-down side. A possible explanation is the upwash of the propeller blade-up side, leading to overall higher leading edge angle of attack compared to the blade-down side, as shown in Figure 9.4.

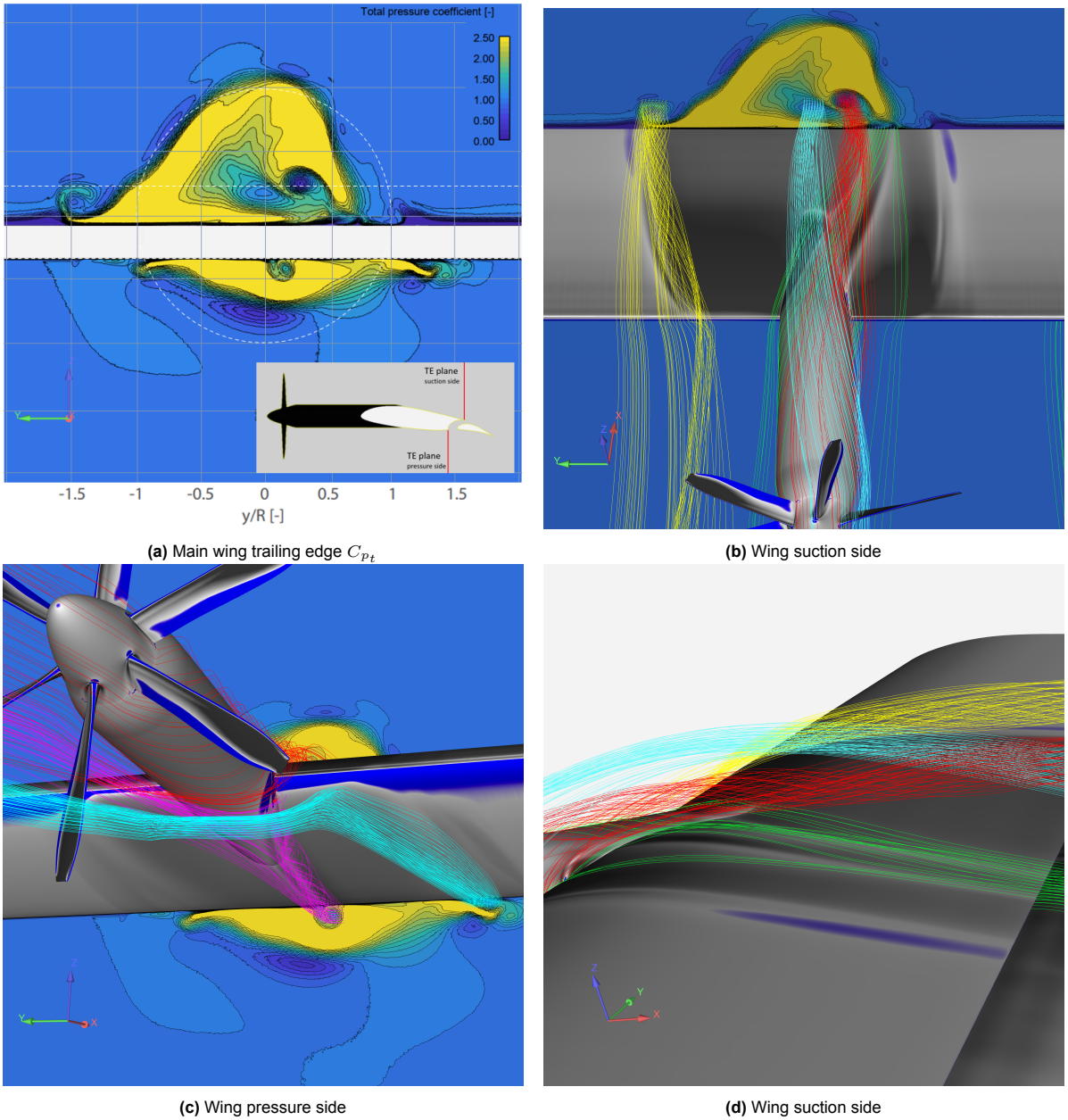

(a) Main wing trailing edge C_{p_t}

(b) Wing suction side

(c) Wing pressure side

(d) Wing suction side

Figure 9.2: mean-streamlines colored by region of release. Streamlines released (in downstream and upstream direction) from total pressure coefficient contour at main wing trailing edge.

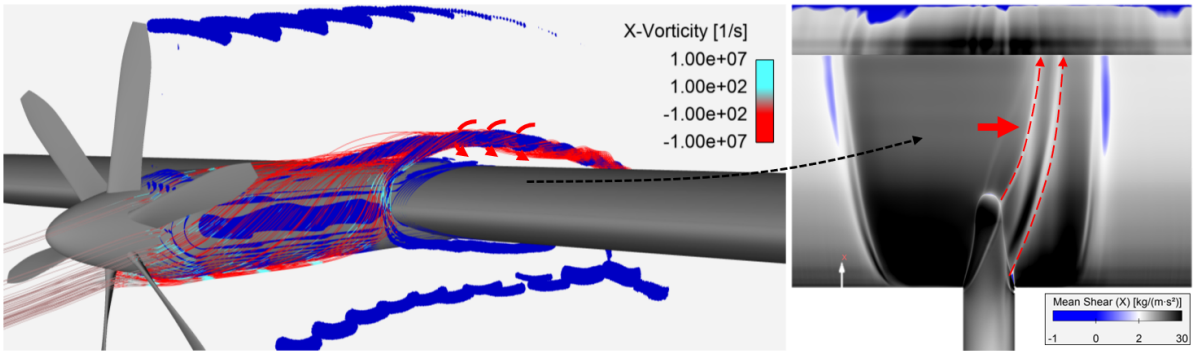

Figure 9.3: Visualisation of streamlines, colored by x-vorticity, shaping propeller-nacelle-wing interaction vortices. In 3D volume clip-planes of positive Q-criterion.

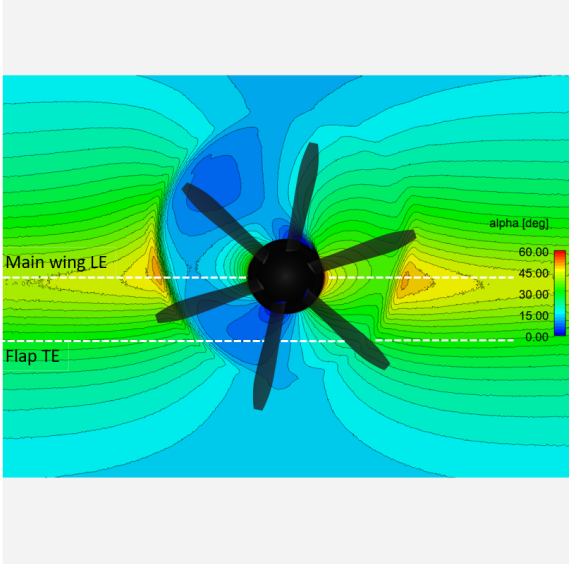

Figure 9.4: Local mean angle of attack contours at $0.1\ x/c$ upstream of main wing leading edge, defined as $\alpha_{local} = \arctan(\overline{U_z}/\overline{U_x}) + 5°$

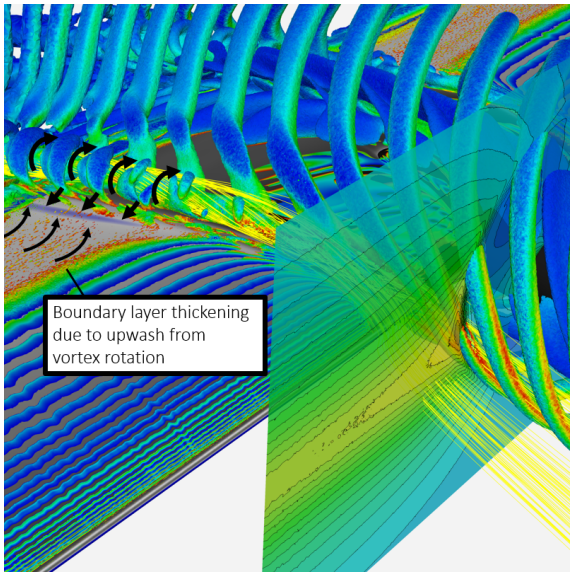

Figure 9.5: Visualisation of streamlines in yellow, shaping propeller-wing interaction vortices at propeller slipstream - wing leading edge intersection. In 3D volume Q-criterion iso-surfaces.

9.1.2. Propeller slipstream trajectory and propeller tip vortex interaction

The on-surface time-averaged slipstream edges are visualised by high contrast surface x-shear contours in Figures 9.6 and 9.7, depicted by a sudden spanwise transition from high surface shear (black colored) to low surface shear (grey and white colored).
On the suction side, the blade-down side shows the largest spanwise slipstream divergence, while on the pressure side the blade-up side shows the largest spanwise extent of the slipstream, leading to a spanwise misalignment between the upper and lower halves of the propeller slipstream. This misalignment is clearly visible in the C_{p_t} contour of Figure 9.2a and in Figure 9.8a, tThe latter displays iso-surfaces of the total pressure coefficient, revealing the flow transition from the wing's pressure side to the upper surface of the flap.
Figures 9.6 and 9.7 show four identified factors from current simulation that contribute to the deformation of the slipstream:

- Leading edge propeller tip vortex interaction
- Nacelle pressure gradient
- Slipstream edge pressure gradient
- Resulting trailing vorticity

Each factor is discussed in the following paragraphs.

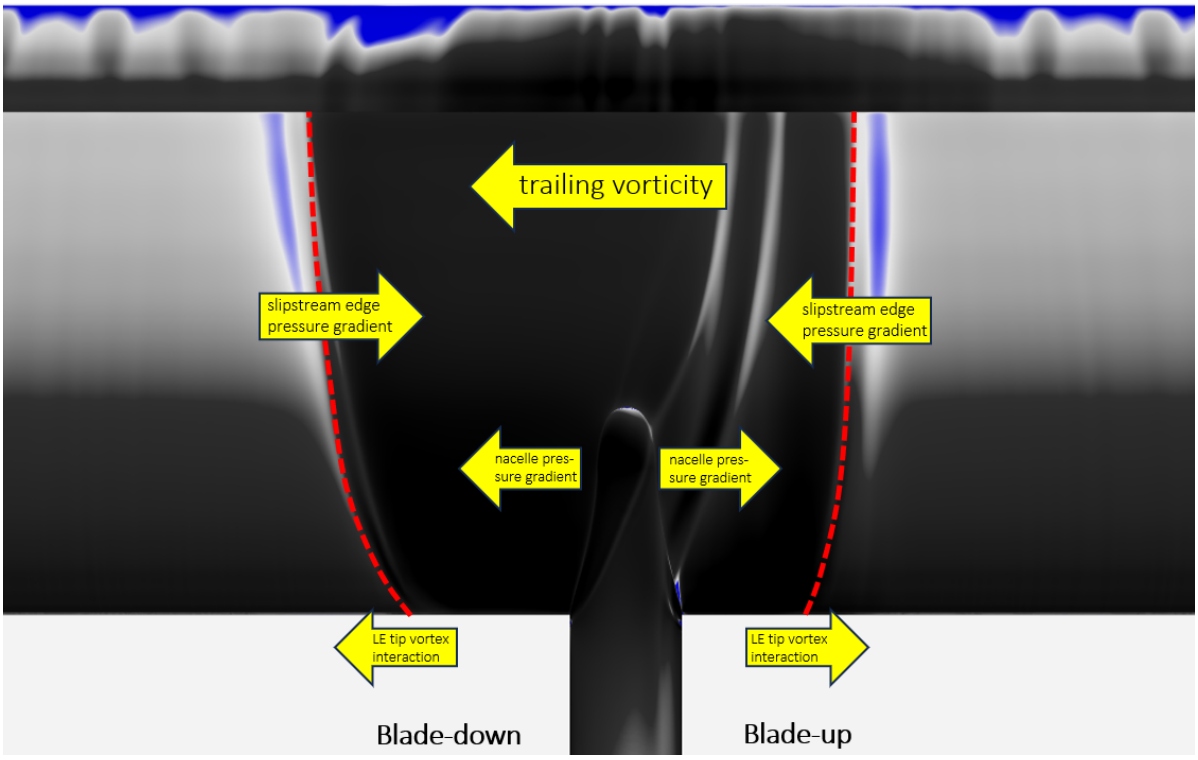

Figure 9.6: Contributing factors influencing spanwise slipstream displacement. Arrows depict effect of each factor on slipstream deformation. Wing suction side.

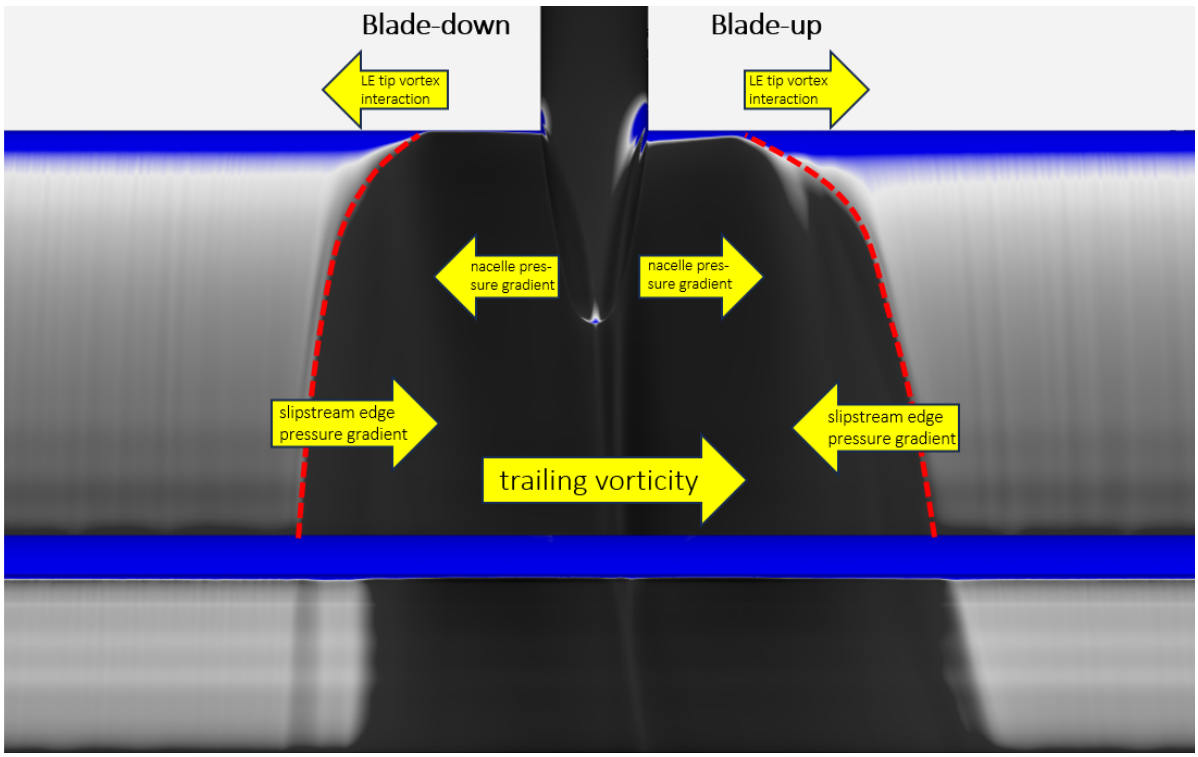

Figure 9.7: Contributing factors influencing spanwise slipstream displacement. Arrows depict effect of each factor on slipstream deformation. Wing pressure side.

Leading edge propeller tip vortex interaction
The wrapping of the tip vortices around the leading edge, visualised in Figure 9.8b and as earlier briefly described in Section 7.3, plays a large role in the slipstream divergence near the main wing leading edge. As described by Felli [91], the vortex orientation and corresponding image vortex (located 'in' the wing) effect lead directly to spanwise divergence of the tip vortices near the leading edge of the wing. The suction- and pressure-side vortex branches remain connected by a stretched vortex filament, shown in Figure 9.8b. Weakening of this filament reduces the rate of spanwise stretching [74, 91, 92]. Furthermore, slightly before the tip vortex reaches the leading edge of the main wing, the vortex begins to bend already to a kink section. This bending and kink formation is the result of the chordwise velocity field - increasing flow velocity (and thus vortex convection) at the wing upper side, and reducing flow velocity on the wing pressure side, which starts to shape prior to the wing leading edge.

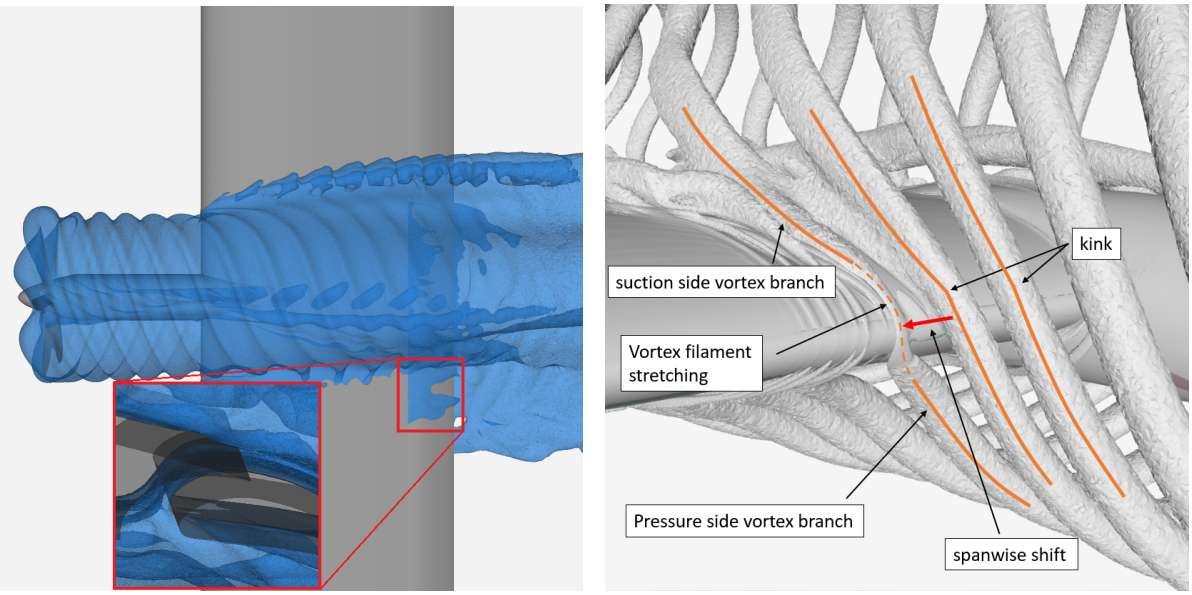

(a) Total pressure coefficient 1.2 [-] iso-surface to illustrate main wing pressure side slipstream flow moving to flap suction side.

(b) Negative $\lambda 2$ iso-surface at blade-down main wing leading edge to visualise tip vortex wrapping.

Figure 9.8: Total pressure coefficient and $\lambda 2$ iso-surfaces.

Nacelle pressure gradient, slipstream edge pressure gradient and resulting trailing vorticity
After the initial slipstream widening, the vortex filaments lose strength and the slipstream deformation can be primarily explained by considering the variation in spanwise circulation and secondary by spanwise pressure gradients at the nacelle and slipstream edge regions.

The spanwise trailing vorticity distribution can be derived by the spanwise lift distribution, shown in Figure 9.10. Based on this figure the blade-up side of the main wing indeed generates more lift than the blade-down side. In line with Veldhuis's reinterpretation of resulting trailing vorticity of Section 2.3.3 this is expected to explain the main slipstream deformation.

Figure 9.9 shows the spanwise pressure gradient at various positions. The spanwise pressure gradient on the slipstream edges is pointed inboard at both the blade-up and blade-down wing suction sides. The nacelle adds a fourth spanwise force component to the surface flow: the nacelle suppresses the suction peak otherwise found at its position, leading to a high-pressure region directly downstream of the nacelle. The local high-pressure imposes a spanwise pressure gradient outboard.

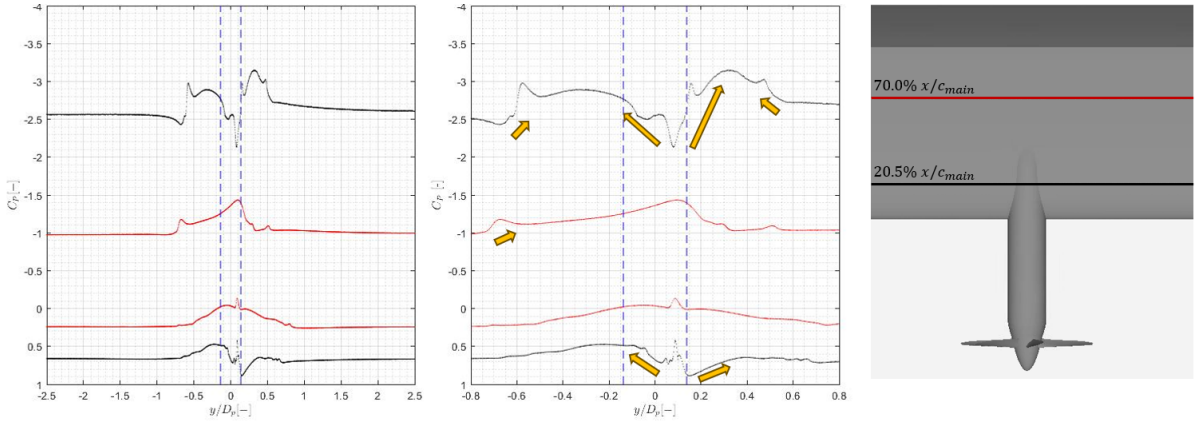

Figure 9.9: Spanwise C_P distributions of main wing pressure and suction sides at two chordwise locations, shown in right figure. Yellow arrows depict direction of spanwise pressure gradient. Dotted blue lines indicate diameter of nacelle.

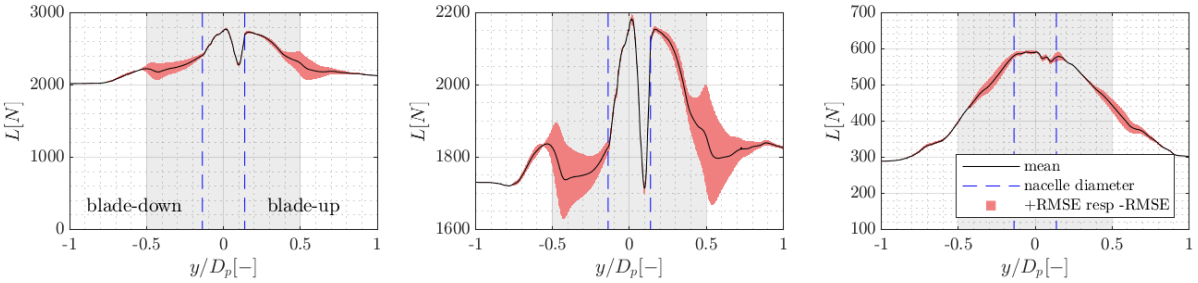

Figure 9.10: Spanwise lift distributions and RMSE. **left:** spinner,nacelle,main wing and flap **center:** spinner,nacelle,main wing only. **right:** flap only.

9.1.3. Unsteadiness of the flow field

The wake of the propeller generates an unsteady flow. This flow is characterized by a periodic change in the velocity and pressure fields. As a result, the spanwise lift distribution, Figure 9.10, shows varying lift forces along the span. The largest variations in lift, up to +/- 7.4% Root Mean Square Error (RMSE), are seen at the slipstream edges due to the tip vortex interaction with the main wing. Near the centerline of the nacelle +/- r_n only minimal variations are observed. To further explore the origins of these fluctuations, multiple chordwise contours of velocity ($\bar{U}_x/U_\infty$) and it's fluctuation relative to the mean velocity ($U'_x/\bar{U}_x$) are shown in Figure 9.12 for spanwise blade-down positions and Figure 9.13 for spanwise blade-up positions. The spanwise locations of these contours are based on interesting locations of the surface x-shear contours of Figure 9.11.
At the blade-up propeller slipstream edge, y/D_p=1.0, the main wing element experiences almost no flow fluctuations as depicted in Figures 9.13g and 9.13h. Some unsteadiness is observed in the vicinity of the cove, which is caused by the local separated flow. The flap's trailing edge shows a large unsteady region due to local flow separation on its trailing edge suction side, but unsteady flow is also observed on its pressure side due to the propeller slipstream, as is identified by the x-shear contours of Figure 9.11.

At y/D_p=-0.37, Figure 9.12e, a high propeller slipstream velocity is observed compared to other spanwise locations. This is believed to be a result of the increased axial velocity in the upper left quarter of the propeller disk due to the non-uniform inflow (Figure 7.19b).

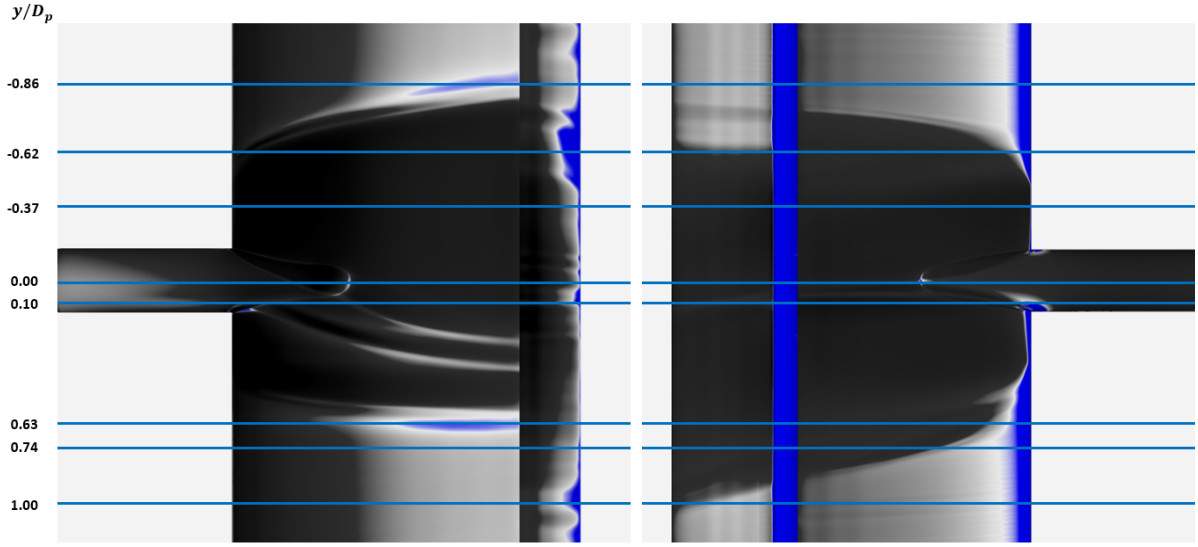

Figure 9.11: Spanwise locations of velocity contours corresponding to Figures 9.12 and 9.13. Time-averaged high contrast surface x-shear, to identify propeller slipstream spanwise extent. Black indicates high downstream shear, blue indicates (approaching) flow reversal regions. Left: suction side. Right: pressure side.

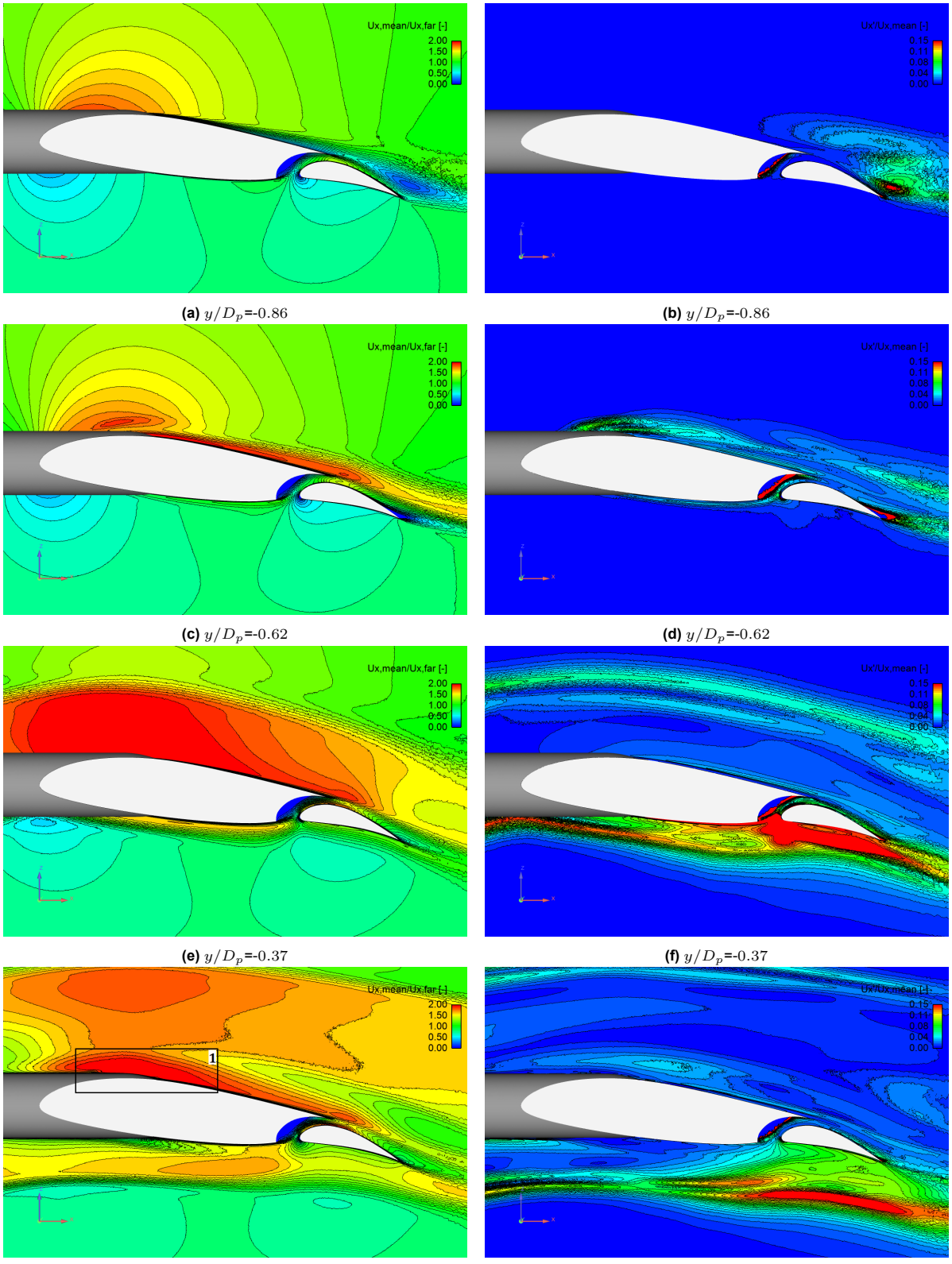

(a) y/D_p=-0.86 **(b)** y/D_p=-0.86

(c) y/D_p=-0.62 **(d)** y/D_p=-0.62

(e) y/D_p=-0.37 **(f)** y/D_p=-0.37

(g) centerline,y/D_p=0 **(h)** centerline,y/D_p=0

Figure 9.12: Mean velocity and fluctuations at various blade-down y/D_p. Left: mean x-velocity divided by far stream x-velocity $\bar{U}_x/U_\infty$. Right: RMSE x-velocity divided by mean x-velocity $U'_x/\bar{U}_x$

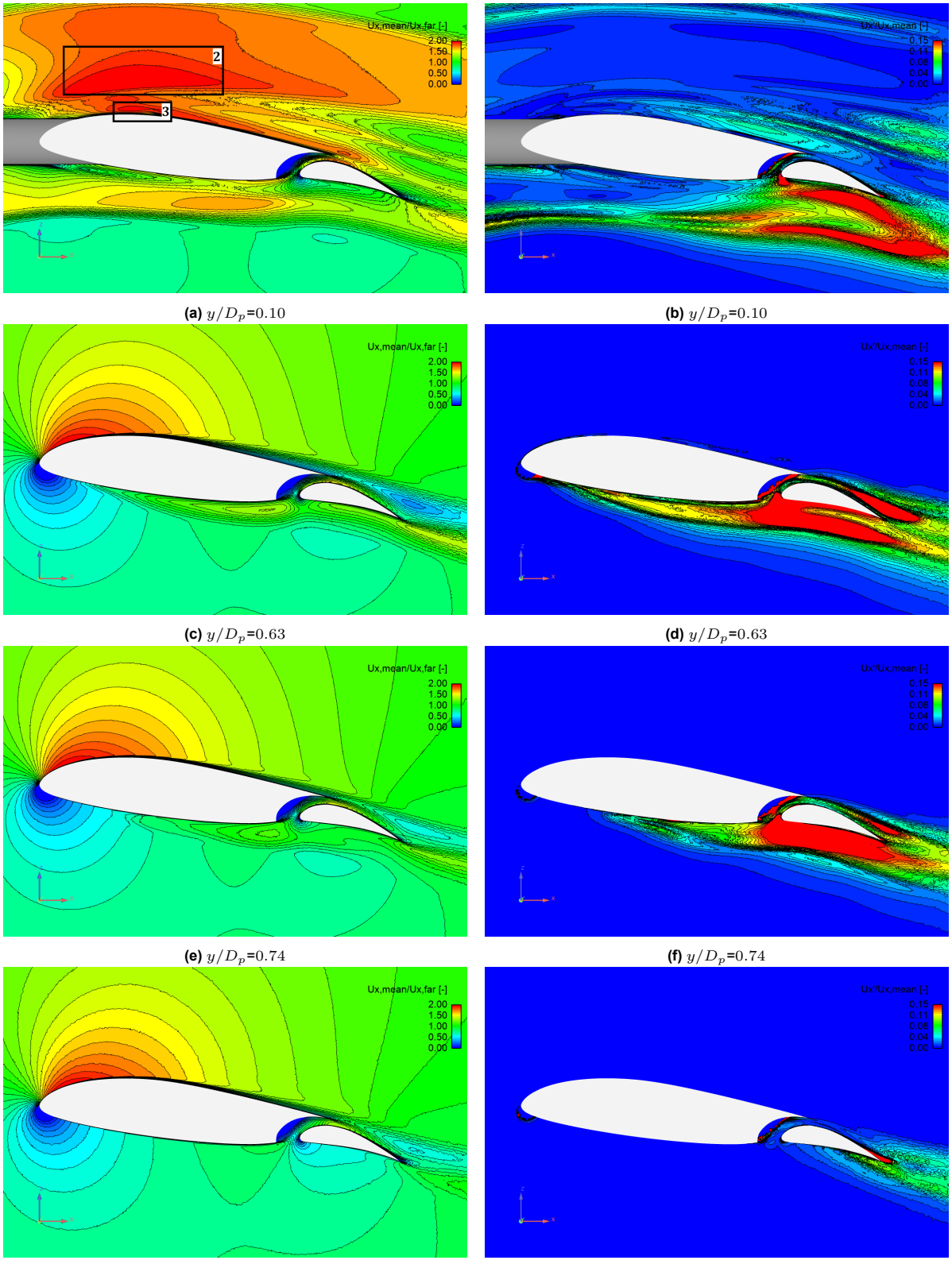

(a) y/D_p=0.10 **(b)** y/D_p=0.10

(c) y/D_p=0.63 **(d)** y/D_p=0.63

(e) y/D_p=0.74 **(f)** y/D_p=0.74

(g) y/D_p=1.0 **(h)** y/D_p=1.0

Figure 9.13: Mean velocity and fluctuations at various blade-up y/D_p. Left: mean x-velocity divided by far stream x-velocity $\bar{U}_x/U_\infty$. Right: RMSE x-velocity divided by mean x-velocity $U'_x/\bar{U}_x$

Near the nacelle centerline, at y/D_p=0 and 0.10 (Figures 9.12g, 9.12h, 9.13a, 9.13b), an increase in flow velocity is observed just above the nacelle up to the main wing trailing edge, depicted as regions 1, 2 and 3. The cause of these locally high velocities is further examined by streamlines and spanwise x-velocity clip-planes in Figure 9.14.

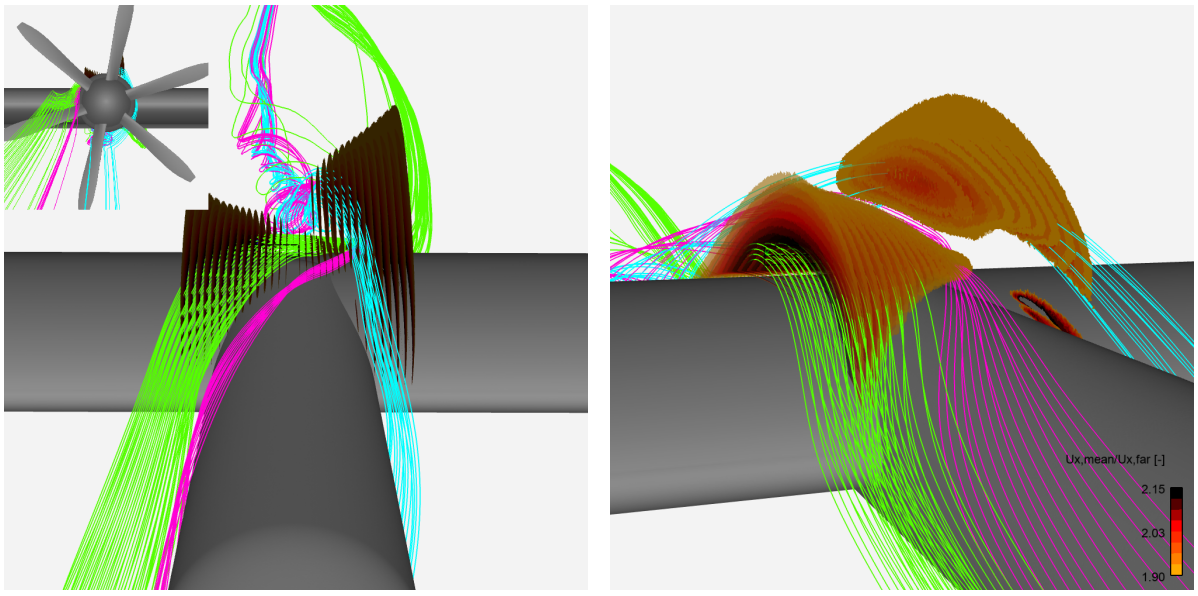

(a) Frontal view **(b)** Side view

Figure 9.14: Mean streamlines released from near-nacelle high x-velocity regions, identified by spanwise contours of $1.90<\bar{U}_x/U_\infty<2.15$.

In this figure, the cyan streamlines correspond to region 2. These streamlines originate from the lower part of the propeller disk and experience an upward flow due to the high angle of attack and propeller swirl orientation. The increased velocity corresponds to the local suction peak at the nacelle-wing intersection, just as the high velocity in region 3. Note that the figures show $\bar{U}_x$, not $\bar{U}$, which explains why this increase in velocity is not seen to extend all the way to the leading edge.
The purple streamlines are released from region 1 and originate from the blade-down propeller side blade root sections. Previously, it was shown that flow in these regions has negative x-vorticity, explaining the movement of the flow to the blade-up side opposite to the propeller rotation by considering an image vortex. The cyan and purple streamlines rotate around the nacelle vortex system.
The green streamlines originate from propeller root- up to mid-blade sections, the latter with less vorticity, hence less spanwise movement.

At the blade-down side, just outside of the propeller slipstream (see Figures 9.12a and 9.12b), the main source of the observed unsteady flow is the wake of the main wing. The velocity fluctuations do not reach the flap surface. In fact, flow and fluctuations from the main wing upper side do not induce unsteadiness in the flap upper side boundary layer along the wing span. The main reason of flow fluctuations on the flap is unsteadiness at the main wing pressure sides. This is clearly shown at spanwise location y/D_p=0.63 (see Figures 9.13c and 9.13d). This location is outside of the main wing suction side propeller slipstream, but inside the slipstream at the main wing pressure side. Unsteadiness due to the slipstream transitions through the cove area to the upper side of the flap, further illustrated by velocity Line Integral Convolution (LIC) in Figure 9.15. The passage of propeller slipstream flow from the main wing pressure side to the flap suction side via the cove area is further visualized by total pressure coefficient iso-surfaces in Figure 9.8a, clearly showing this transition along the flap span.

Note that the fluctuations at the pressure side are larger compared to the fluctuations at the wing suction side overall. This is due to the closer proximity of the propeller tip vortices to the pressure side compared to the suction side due to the high angle of attack setting, as shown in Figure 7.20d and reflected by the high fluctuations in C_p in Figure 7.23f

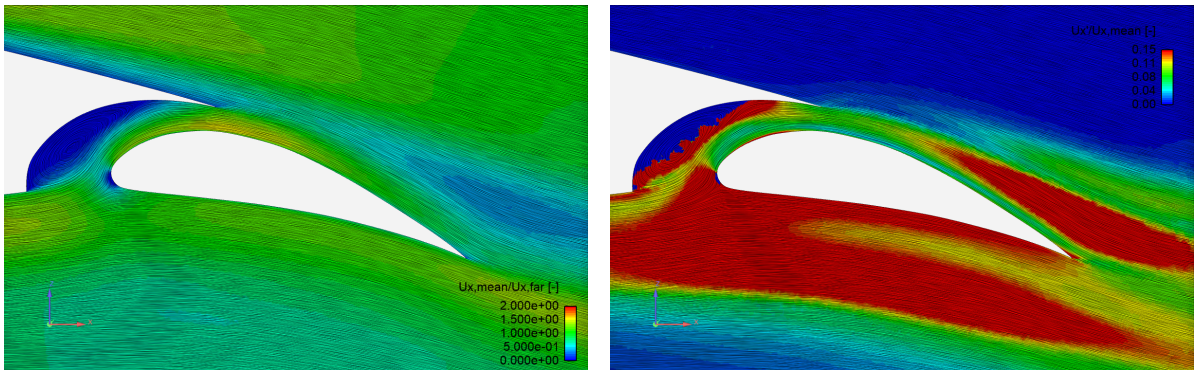

(a) $\bar{U}_x/U_\infty$ **(b)** $U'_x/\bar{U}_x$

Figure 9.15: Zoom-in at y/D_p=0.63 of mean velocity and fluctuations, including mean velocity LIC.

9.2. Flap flow

The complex flow due to propeller, nacelle and main wing interaction transfers downstream to the flap region. The interaction between the main element and flap was already observed to be complex based on the chordwise pressure distributions of Case 1a (see Section 7.1). Interaction effects at the flap are different compared to the main wing. For example due to the fact that the propeller tip vortical structures do not reach the flap suction side no leading edge tip-vortex interaction will occur (in addition to the fact that the flap leading edge is 'covered' by the main wing trailing edge due to the δ_f=15° setting).

The unsteadiness of the flap flow is further quantified by the surface friction coefficient and it's RMSE fluctuations in Section 9.2.1. The findings are coupled to surface-normal velocity profiles. Two interesting locations of separated flow are further investigated to expose the underlying flow mechanisms in Section 9.2.2. It will be shown that the origin of local flow separation regions at the flap can be linked to the root sections of the propeller blades.

9.2.1. Assessment of flap flow unsteadiness

The chordwise velocity contours of Figures 9.12 and 9.13 show that unsteady flow from the main wing pressure side transfers through the cove area to the flap suction side. The influence of this unsteadiness on the spanwise surface friction coefficient in downstream direction $C_{f,x}$ [-] is shown in Figure 9.16. The first row of this figure shows main wing spanwise $C_{f,x}$, slightly upstream of the cove area. The next 4 rows show flap spanwise $C_{f,x}$ near its leading edge, 31.3%, 65.39% x/c_{flap} and near its trailing edge. The following observations are made:

At the main wing, the pressure side shows significant variation in $C_{f,x}$, while the suction side only shows marginal variations. It has been discussed and shown earlier that most vortical structures on the suction side are relatively far from the surface, while the pressure side experiences large flow variations due to the close proximity of the vortical structures. Near the nacelle centerline only small fluctuations occur, comparable to the small fluctuations in the earlier shown spanwise lift distribution of Figure 9.10.

Both the flap suction and pressure sides show large fluctuations in $C_{f,x}$. The fluctuations at the main wing pressure side transfer to the flap upper and lower surfaces, leading to large fluctuations at the flap. The fluctuations are seen to reduce downstream on the suction side, while the lower surface shows fairly constant fluctuation magnitude up to the trailing edge.

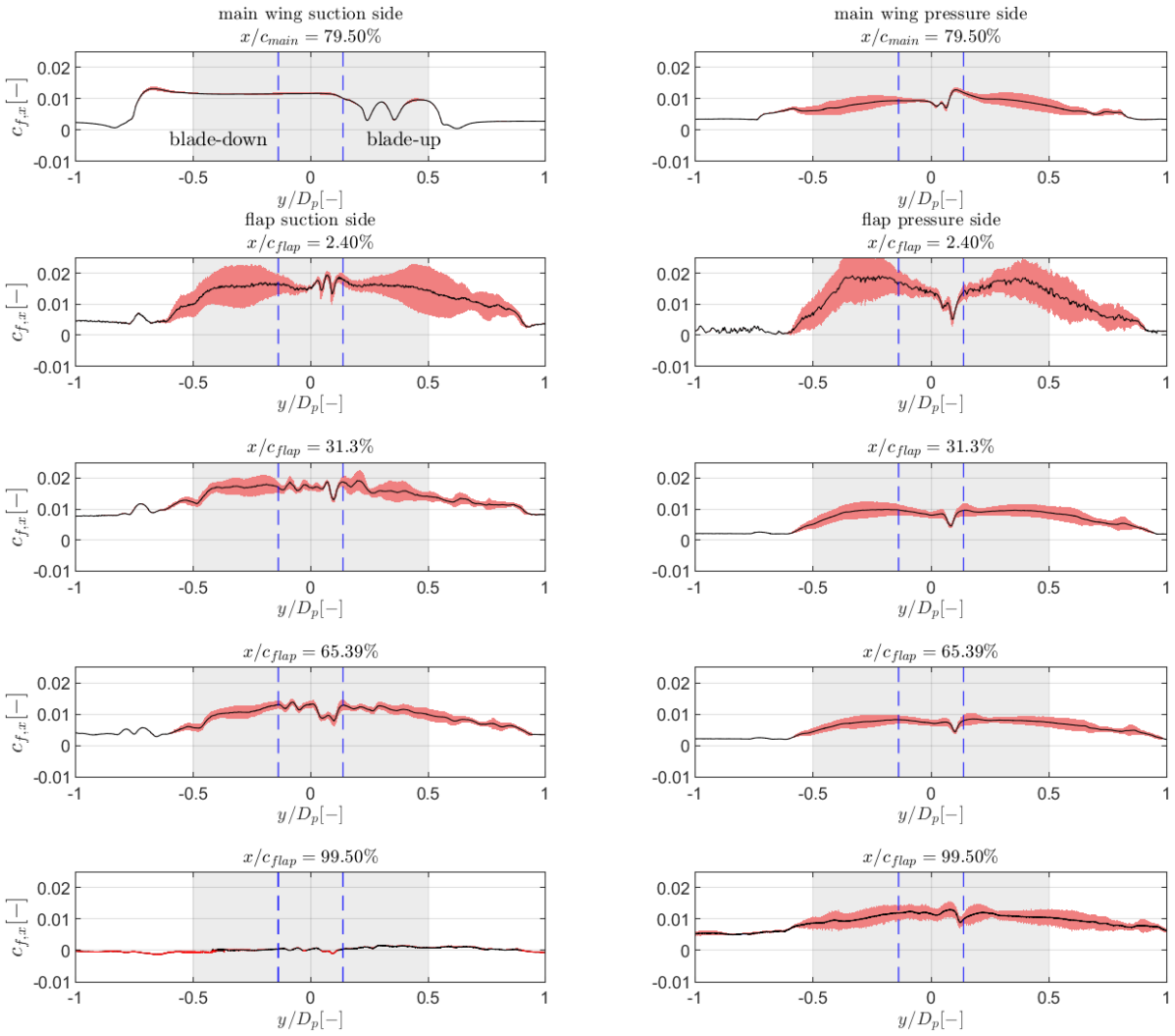

Figure 9.16: Spanwise surface friction coefficient variation and RMSE at main wing (top row) and flap (4 last rows) suction and pressure sides. Rose colored areas indicate the magnitude of the fluctuations by RMSE. Red mean flow areas indicate separated areas at the last row flap suction side.

At four spanwise locations also absolute flow velocity and its fluctuations are plotted in surface-normal direction in Figure 9.17 at flap x/c_{flap}=31.3% and 99.5%, corresponding to the third and fifth row of Figure 9.16. The selected spanwise locations correspond to interesting locations with flap flow separation as shown in the surface shear distributions of Figure 9.11, at the nacelle centerline and outside the propeller slipstream.
Figure 9.17a corresponds to the major flow separation region at the blade-down side. Figure 9.17b shows the velocity profiles at the nacelle centerline. The velocity profiles of the minor flap separation region near the nacelle centerline are shown in Figure 9.17c. Figure 9.17d shows respective profiles at 1 D_p to the blade-up side. The following observations are made:

The velocity profiles at the flap suction sides are overlapped with the velocity profiles of case 1a. At $y/D_p = 1.0$, case 2a shows slightly higher velocities at x/c_{flap}=31.3%, with practical no fluctuations. This position is still close to the propeller slipstream, so slight deviations compared to case 1a can occur. Near the trailing edge the velocity fluctuations increase due to a separated flow region at the flap. Away from the surface the velocity distribution is shown to be rather crude due to the required local mesh coarsening of the propeller wake to stay within computational resource limits.

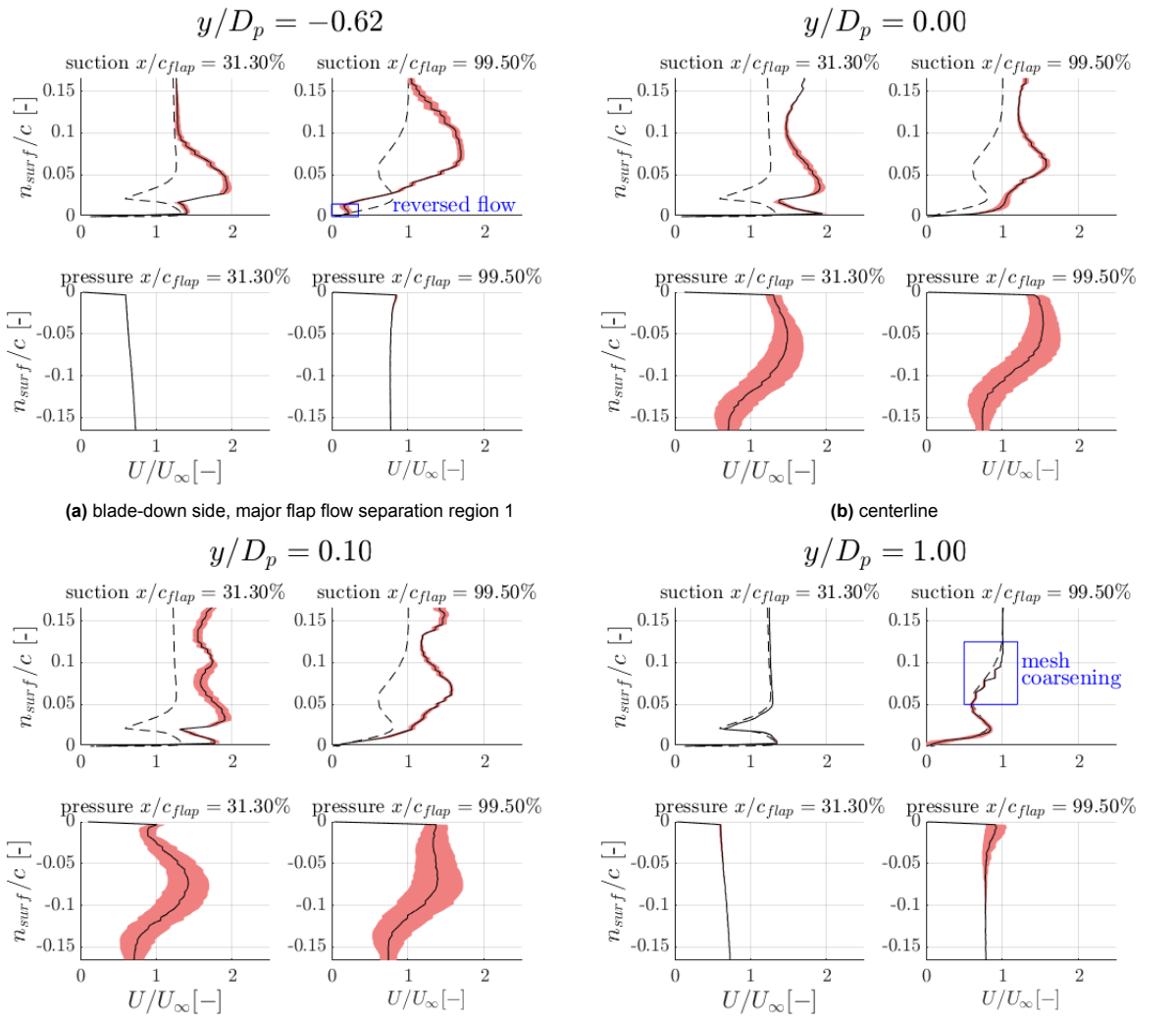

(a) blade-down side, major flap flow separation region 1

(b) centerline

(c) blade-up side, minor flap flow separation region 2

(d) blade-up side, propeller slipstream edge at flap pressure side

Figure 9.17: Flap absolute velocity profiles at 4 spanwise locations, both suction and pressure sides. Black lines indicate mean velocity, rose colored areas indicate velocity RMSE, dashed black lines indicate case 1a (wing-flap only) RANS velocity profiles, see Figure 7.6

At y/D_p=0.0 and 0.1 the pressure sides show large variations in velocity, being in the center of the propeller slipstream and close proximity of the various vortices. Just at the edges (y/D_p=-0.62 and 1.0) of the propeller slipstream only little variations occur. Within the slipstream, the pressure side velocity profiles show the gradual increase and reduction of velocity due to the propeller slipstream induced axial velocity.

The suction side at $y/D_p = 0.0$ shows a rapid increase and succeeding reduction of velocity between $n_{surf}/c = 0$ to 0.02 at 31.30% chord. Thereafter the velocity rapidly increases and reduces between $n_{surf}/c = 0.02$ to 0.1 due to the propeller-nacelle-wing interaction, i.e. the green streamlines in Figure 9.14. At $n_{surf}/c > 0.1$ velocity increases due to the propeller wake.

The spanwise skin friction coefficient distributions of the earlier discussed Figure 9.16 also shows that flap flow inside the propeller slipstream is less likely to separate compared to outside the propeller slipstream. This is explained by the high wall-normal velocity gradients. For example, at $x/c_{flap} = 99.5\%$ at the nacelle centerline it is observed that the wall-normal velocity gradient is higher compared to outside the slipstream at $y/D_p = 1.0$. The surface skin friction coefficient follows from the wall-normal

velocity gradient, according to the general definition of wall shear stress :

$$\tau_w = \mu \frac{\partial u}{\partial y} \mid_{y=0} \tag{9.1}$$

and

$$C_f = \frac{\tau_w}{0.5 \rho_\infty U_\infty^2} \tag{9.2}$$

In which μ is dynamic viscosity, u local flow velocity and y wall distance. High-momentum flow of the propeller slipstream at the pressure side passes through the cove area, increasing the wall-normal velocity gradient, postponing stall. This explains the in general reduced flap trailing edge flow separation in the present case compared to flap regions outside of the propeller slipstream. However, the flap also shows some areas with flow separation within the propeller slipstream. The discussion of the span- and chordwise extend of flow separation on the flap suction side is continued in the next section.

9.2.2. Flap flow separation regions

As this sections aims to provide a close view to the origin of separated regions, the discussion of flap flow separation regions should be accompanied by a word of caution. (Unsteady) RANS simulations are not known for their accurate prediction of flow separation. Furthermore, vortices will be shown to play a role in the origin of separated flow regions at the flap, while the SA turbulence model used is known for premature diffusion of vortex cores. The high-resolution mesh and second order discretization minimizes CFD errors, but the current CFD setup might cloud the actual physics of the stalled areas.

The increase of flow momentum due to the propeller slipstream has, in general, reduces flow separation on the flap. However, two distinct flow separation regions within the propeller slipstream affected region are observed in current results, as shown in Figure 9.18: a major flow separation region at the blade-down side slipstream edge, depicted by number 1, and a minor flow separation region near the nacelle centerline, depicted by number 2.

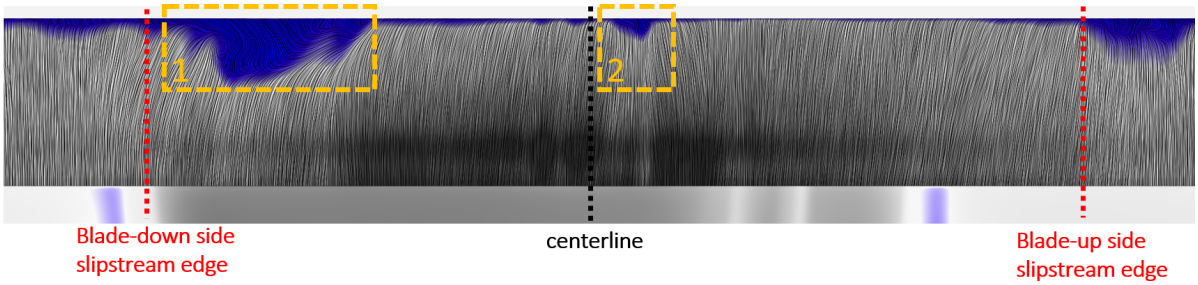

Figure 9.18: Distinct flap separation regions within propeller slipstream

The time-dependent behavior of these regions is further explored in Figure 9.19. The spanwise $c_{f,x}$ distribution shows a chaotic trend of spanwise $c_{f,x}$ RMSE. At $y/D_p \approx -0.5$ large variations occur, corresponding to the large chordwise variation of flow separation of region 1. Locally the chordwise flow separation position varies at this position between $x/c_{flap} = 83.3\%$ up to 98.0. Also between $y/D_p \approx -0.4$ up to -0.25 above average RMSE values are seen, but as this region fluctuates around $c_{f,x}$=0 the effects of these fluctuations are not clearly visible in the bottom figure of Figure 9.19.
Although the two selected flow separation regions are most noticeable at current operating conditions, an increase in angle of attack will likely show more distinct separated regions due to increased adverse pressure gradients between $y/D_p \approx -0.4$ up to -0.25 and at $y/D_p \approx -0.1, -0.04, 0.26$ and near the blade-up side slipstream edge, for example, based on the local dips in $c_{f,x}$. However, current research will focus only on the two distinct regions, given the high computational costs of post-processing, time constraints, and current very limited knowledge from literature on observed flow. The following sections further elaborate on the two reversed flow regions.

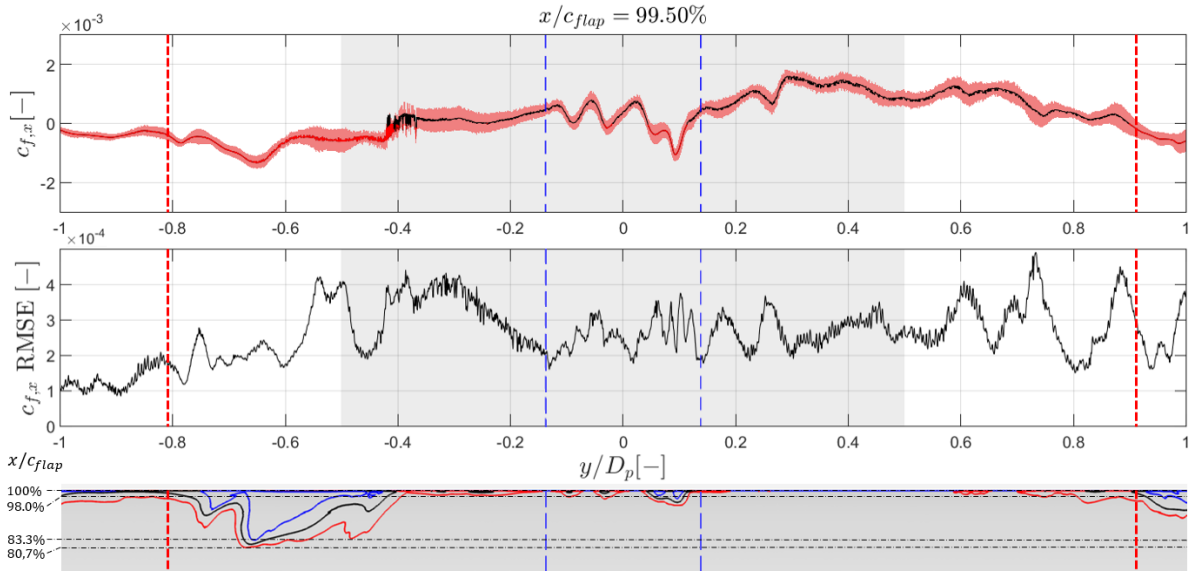

Figure 9.19: Flap suction side trailing edge spanwise variation of $c_{f,x}$ and chordwise separation. **Top row:** spanwise $c_{f,x}$ variation overlayed with $c_{f,x}$ RMSE variation. Red mean flow areas indicate separated areas. Dashed blue lines indicate nacelle diameter. **Middle row:** Spanwise $c_{f,x}$ RMSE. **Bottom row:** spanwise variation in chordwise separation x/c at flap suction side. Red lines show the most forward x/c at which separation occurs, blue lines the most backward x/c. Black lines show the mean x/c separation position.

Minor flap separation region

Streamlines corresponding to the trailing edge downstream of the minor flow separation region are shown in Figure 9.20. The flow corresponding to the stalled region is seen to originate from the main wing pressure side vortex, discussed earlier in Section 9.1.1 and by Figure 9.21.

Vortex flow is seen to transfer in its entirety through the cove area to the flap suction side, although the actual vortex disintegrates from the cove onward based on lacking Q-criterion iso-surfaces in the cove-area. The vortex is positioned relatively far from the lower main wing surface compared to how close the streamlines are to the flap suction side surface, as shown in Figure 9.20c.

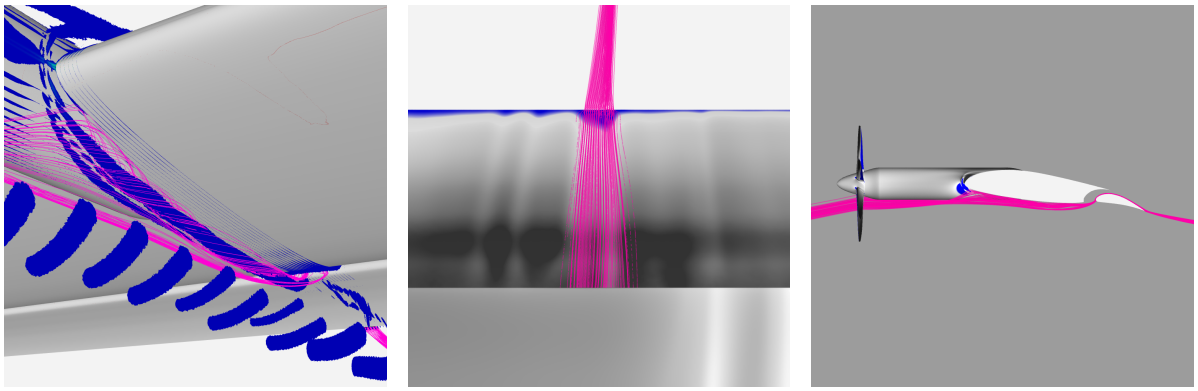

(a) Zoom-in pressure side. Streamlines and Q-criterion iso-surface

(b) Zoom-in flap suction side. Streamlines and surface shear.

(c) Side view

Figure 9.20: streamlines trajectory to minor flap suction side separated flow region at y/Dp=0.1, originating from pressure-side vortex system (purple streamlines) in Figure 9.21

The flow corresponding to the vortex shows a low total pressure coefficient at the main wing trailing edge in Figure 9.21. The author believes that the low-energetic (due to internal viscosity) vortex flow, just upstream of the main wing pressure-side cove area, weakens the flap boundary layer through the transfer of this flow through the cove area, consequently inducing flow separation.

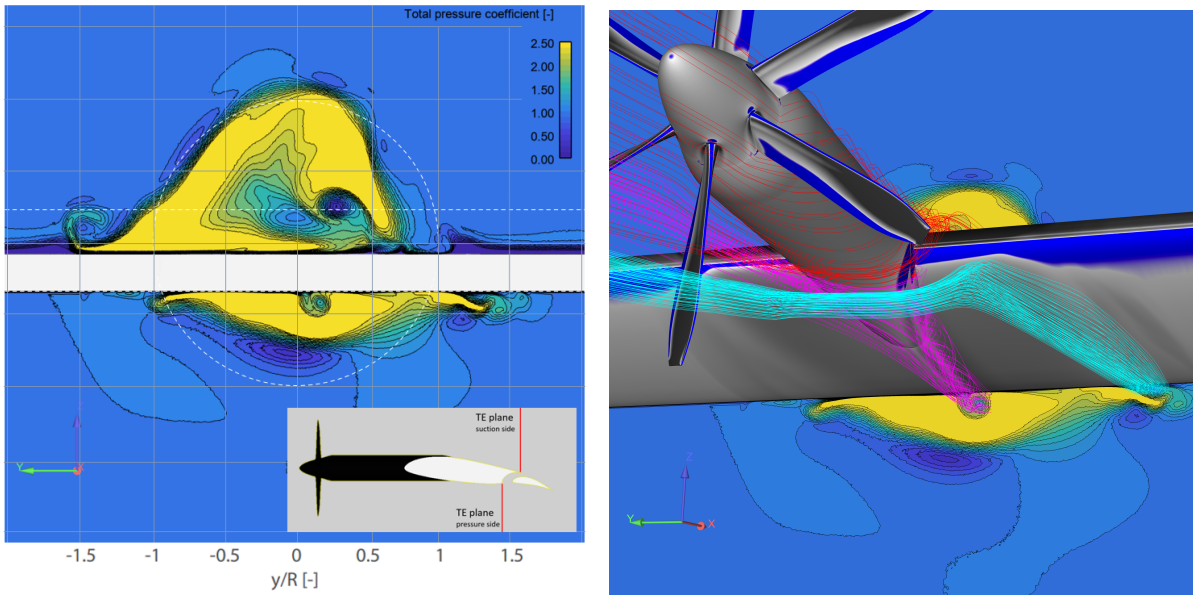

(a) Main wing trailing edge C_{p_t}

(b) Wing pressure side

Figure 9.21: Streamlines colored by region of interest and total pressure coefficient contour

However, this negative effect on high-lift performance should be placed in context: the velocity profile at y/D_p=0.1, Figure 9.17c, still shows a slightly steeper wall velocity gradient compared to regions outside of the propeller slipstream. So although local performance is negatively affected due to the low-energetic flow, the flow still contains slightly more energy compared to non-slipstream flow and local flap lift performance is still ≈ 1.9 higher compared to outside the slipstream, as shown in the spanwise lift distribution of Figure 9.10. The spanwise lift distribution clearly shows the negative effect of the local flow separation. If the local dip in lift can be avoided in future aircraft design, the expected increase in lift of the slipstream affected flap region is only an insignificant ≈ 0.15% based on integrating the spanwise flap lift distribution.

Major flap separation region

A similar approach is applied to investigate the origin of the major flow separation. Streamlines are calculated downstream of the separated flow region, shown in Figure 9.22b. Also this flow originates from the main wing pressure side. C_p contours of Figure 9.23a reveal a low pressure region at the middle of the flap, caused by the slipstream high-momentum flow. This low pressure area imposes a spanwise inboard pressure gradient, which strengthens the spanwise deflection of the shear lines next to the overall flap slipstream shift to the blade-up side. These mutually reinforcing factors play a role in the significant inboard deflection of the shear lines when approaching the stalled region compared to other spanwise flap locations. The deflection of the streamlines increases the distance traveled along the surface and move the flow to an area with increased adverse pressure gradient, leading to increased thickness of the local boundary layer.
Furthermore, the purple streamlines are more separation-sensitive due to their relative low energy compared to other slipstream flow, as observed by Figure 9.23b by total pressure coefficient contours.

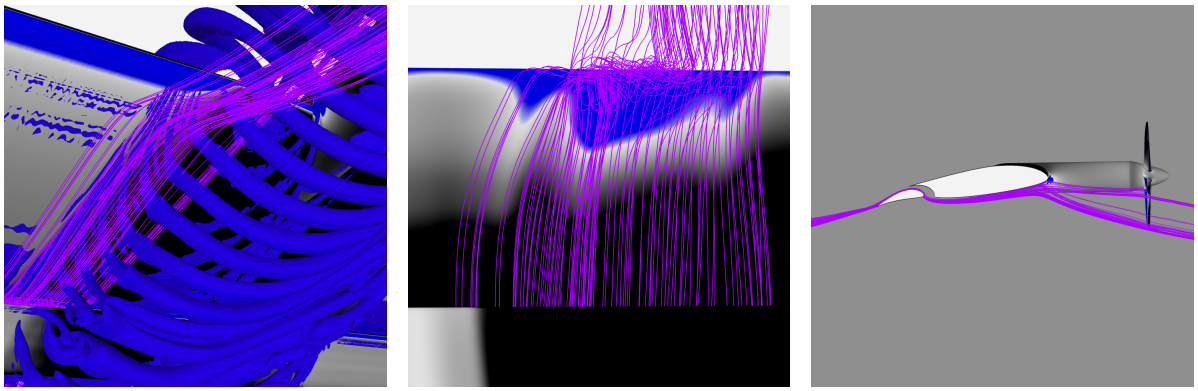

(a) Zoom-in pressure side **(b)** Zoom-in flap suction side **(c)** Side view

Figure 9.22: streamlines trajectory to major flap suction side separated flow region at y/Dp=-0.62.

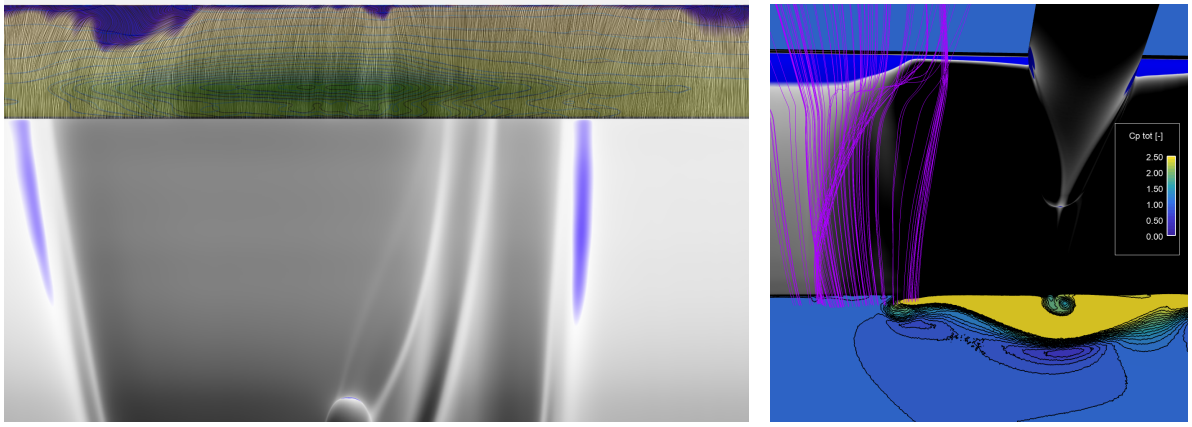

(a) Main wing and flap suction side, colored by x-shear. In addition, the flap shows shear LIC and an overlapped contour of mean surface C_p of Figure 7.23b.

(b) streamlines and total pressure coefficient contour.

Figure 9.23

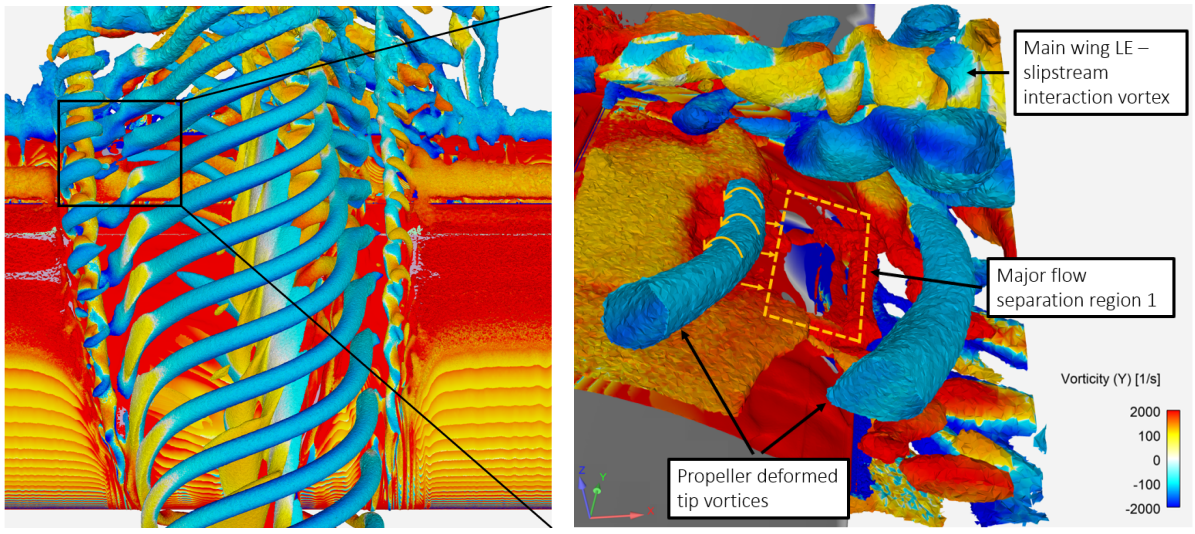

(a) top view **(b)** Zoom-in flap suction side, major flow separation region

Figure 9.24: $\lambda 2$ iso-surface, colored by y- vorticity.

The origin of the flow separation region is further examined by considering the suction side vortex systems in Figure 9.24, originating from the propeller tip vortices and main wing - slipstream intersection. The deformed propeller tip vortices do not reach the flap surface as shown in Figure **??**, but, if they impose any effect on the flap surface, it should be positive due to y-vorticity. The vortex originating from the main wing leading edge - slipstream intersection has positive x-vorticity (see Figure 9.1) and should impose a flow outboard, contrary to the actual surface flow direction according to Figure 9.23a.

In this chapter it is proven that the overall flap surface flow field is dominated by the main wing pressure side flow field. The flow corresponding to the major flow separation is low energetic and originates from the propeller slipstream edge. The vortex system originating from the main wing suction side has several favorable effects on the flap, next to the high momentum flow of the propeller slipstream. However, the flap boundary layer still separates, underlining that the flap boundary layer is dominated by the main wing pressure side flow field and spanwise flow variations imposed by the slipstream deformation, affecting flap performance. The major flap flow separation region is shown to be complex and not easy to decompose and a complete insight is not achieved in this report. Additional research is necessary to comprehensively analyze the flow and its interaction effects before a definitive conclusion can be reached.

10

Conclusion and Recommendations

10.1. Conclusion

Based on the current literature, there is a knowledge gap on a detailed understanding of flap flow in a propeller-wing-flap system, whereas a thorough understanding of flap flow subjected to a propeller slipstream is of interest to maximize high-lift performance in future DEP systems. Optimal high-lift performance is most important during the critical phases of flight, such as take-off and go-around conditions. This led to the following main research question: What are the flap boundary layer characteristics of a propeller-wing-flap system at high-lift conditions?

To answer the main research question, an unsteady RANS simulation with the Spalart-Allmaras turbulence model is performed at a chordwise Reynolds number of 2 million, a six-bladed propeller advance ratio of 0.765 and a single slotted flap deflection angle of 15° at an angle of attack of 8.3°.
The flow field that the flap experiences is heavily influenced by the propeller, nacelle and wing. These interactions are therefore analysed in detail, leading to the answer of the first sub-question on which aerodynamic interactions shape the flow field at the trailing edge of the main wing.

The propeller slipstream at the main wing suction side shifts to the blade-down side, while the pressure side shifts to the blade-up side. The dominant factor behind slipstream deformation on the wing surface is the distribution of spanwise trailing vorticity, accompanied by three other contributing factors.
Firstly, at the main wing leading edge the slipstream diverges on the blade-down as well as the blade-up side due to propeller tip vortex orientation.
Secondly, the nacelle locally suppresses the main wing leading edge suction peak, leading to a high pressure region downstream of the nacelle, leading to additional slipstream expansion.
Lastly, at the slipstream edge a spanwise pressure gradient imposes an inboard convergent force to the slipstream.

Two distinct vortex cores are identified. The first vortex core is located above the surface of the wing suction side near the nacelle centerline and originates from the blade-up side propeller root sections. Streamlines originating from these sections converge to form a compact, counterclockwise-oriented vortex, influenced by the upwash of the nacelle. The orientation of this vortex imposes a spanwise flow component to the blade-up side on the wing surface, opposite to the propeller swirl and slipstream shift. The second vortex core is positioned beneath the surface of the wing's pressure side. Originating from the lower section of the propeller disk, this flow creates a vortex similar as the first vortex. Although its orientation remains the same, being situated on the lower side of the wing introduces a spanwise flow component towards the nacelle centerline.

At the edges of the slipstream vortices exist originating from tip vortex - wing leading edge interaction. The vortices, due to its orientating, are believed to lead to boundary layer thickening just outside the slipstream on the main wing suction side, accelerating flow separation. This flow separation is further facilitated by an increased angle of attack at the blade-up side due to propeller upwash. Hence, the flow

is more prone to separate just outside of the blade-up side slipstream compared to the blade-down side.

Surface pressure coefficient contours and chordwise pressure coefficient distributions of the wing and flap show large time-dependent variation in pressure coefficient. As a result, the spanwise lift distribution shows variations up to +/- 7.4% RMSE, especially near the slipstream edges due to the interaction of the propeller tip vortex with the wing boundary layer. In general, flow fluctuations on the pressure side (exceeding 100% C_p RMSE) exceed those on the wing suction side ($\approx$ 10% C_p RMSE). This is attributed to the various vortex systems being in closer proximity to the pressure side, a direct consequence of the high angle of attack setting pushing the flow towards the pressure side.

It is proven that the overall flap surface flow field is dominated by the main wing pressure side flow field. Iso-surfaces of the total pressure coefficient reveal that part of the propeller slipstream transfers from the main wing's pressure side, (including the fluctuations exceeding 100% C_p RMSE), to the suction side of the flap, traversing through the cove area. The influence of this flow on the flap is examined to address the sub-questions regarding the interaction of vortices with the flap boundary layer and the variations in the chord- and spanwise flow fields of the flap.

Spanwise surface friction coefficient C_f distributions show high unsteadiness in C_f at the flap leading edge, originating from the wing pressure side. It is noted that the flow and fluctuations originating from the upper side of the main wing are not seen to cause instability in the boundary layer on the upper side of the flap across the span of the wing in present work. Propeller tip vortices do not reach the flap upper surface and the vortices originating from the main wing leading edge pass well over it. They do approach close to the lower surface, maintaining fluctuations in C_f and velocity at a relative constant level in downstream direction.

In general, the high momentum slipstream flow delays separation by increasing the wall-normal velocity gradient. However, two distinct flow separation regions within the propeller slipstream affected region are observed in current results.

A small flow separation region occurs near the nacelle centerline, reducing flap lift by an estimated 0.15% when considering the flap surface within the propeller slipstream. Streamlines reveal that flow in this region originates from the main wing pressure side vortex - the second vortex core discussed above. The vortex flow is seen to transfer in its entirety through the cove area to the flap suction side, although the actual vortex breaks apart from the cove onward. The low-energetic (due to internal viscosity) vortex flow weakens the flap boundary layer, consequently inducing flow separation.

A large flow separation region occurs inboard of the blade-down slipstream edge. Locally the chordwise flow separation position varies at this position between $x/c_{flap} = 83.3$% up to 98.0%. The flow corresponding to the major flow separation is low energetic and originates from the propeller slipstream edge. At the flap near the separated flow region an inboard spanwise pressure gradient exists due to local low C_p at the flap, next to the overall slipstream shift to the blade-up side. The vortex system originating from the main wing suction side has several favorable effects on the flap, next to the high momentum flow of the propeller slipstream. However, the flap boundary layer still separates, underlining that the flap boundary layer is dominated by the main wing pressure side flow field and spanwise flow variations imposed by the slipstream deformation, affecting flap performance. This flap flow separation region is shown to be complex and not easy to decompose. A complete insight is not achieved in this report. Additional research is necessary to comprehensively analyze the flow and its interaction effects before a definitive conclusion can be reached.

10.2. Recommendations

The following recommendations for continued work on this subject are identified:

- Most important is the lack of validation data of current setup. Present propeller-wing-flap results have been verified qualitatively and good agreement is observed, but quantitative data is not available. This limits the assessment of, for example, numerical dissipation of vortices. On that topic:
- Validation data is also valuable to select an appropriate turbulence model for further research. The used SA model is known to predict too high levels of viscosity in vortex cores, leading to its premature dissipation [25]. Experimental validation data can help to select the best suited turbulence model for current setup.
- Solving the final simulation of present work required 82.000 CPU hours, a huge burden on the available computational capacity. Although it is believed that current results show that this time is not wasted, simulation time and/or required resources can potentially be reduced by considering:
  - a structured mesh, reducing both solving time and RAM requirements, or,
  - adaptive meshing. A reoccurring statement of current publications is the requirement to have a sufficient grid resolution in key areas of the flow field. ANSYS Fluent is able to identify these key areas, such as vortices and wakes, and locally increase grid resolution, while resolution in areas with low flow gradients is reduced. The results of the high-lift prediction workshop of 2022 have recently been published and include results which used adaptive meshing, outperforming fixed-grid RANS SA results [93].
- To continue on the topic of meshing: no mesh refinement study is performed in current work due to the too high computational costs. As such, the mesh dependency of the results is unclear. A mesh dependency study helps in evaluating the accuracy of the simulation results and identifying the optimum mesh resolution to avoid excessive computational requirements.
- To further improve results, one can consider to include a transition model. The wing-flap setup already showed a complex chordwise pressure distribution. Small deviations w.r.t. the work of Boermans et al. are observed which originate from assuming fully turbulent flow, as proposed by Ribeiro [74]. Also Rumsey stresses on the importance of including transition in high-lift simulations [93]. The author recommends the report of Halila et. al. [44] as introduction on effects of boundary layer transition on the aerodynamic analysis of high-lift systems.
- The present report has presented findings exclusively from a single angle of attack setting. To comprehensively explore interactions among the propeller-wing-flap system, it is recommended to perform simulations across various angles of attack. This approach will help to identify trends and differentiate effects that consistently occur from those specific to high-lift conditions.

Bibliography

[1] S. Biser, G. Atanasov, M. Hepperle, M. Filipenko, D. Keller, D. Vechtel, M. Boll, N. Kastner, and M. Noe. Design space exploration study and optimization of a distributed turbo-electric propulsion system for a regional passenger aircraft. *AIAA Propulsion and Energy 2020 Forum*, August 2020.

[2] D. Keller. Towards higher aerodynamic efficiency of propeller-driven aircraft with distributed propulsion. *CEAS Aeronautical Journal*, 12(4):777–791, August 2021.

[3] A.M.O. Smith. High-lift aerodynamics. *Journal of Aircraft*, 12(6):501–530, 1975.

[4] W. Khan and M. Nahon. Development and validation of a propeller slipstream model for unmanned aerial vehicles. *Journal of Aircraft*, 52(6):1985–1994, November 2015.

[5] L.L.M. Veldhuis. *Propeller Wing Aerodynamic Interference*. Ph.D. dissertation, Delft University of Technology, The Netherlands, June 2005.

[6] Y. Qiu, J. Bai, and L. Qiao. Aerodynamic effects of wing-mounted engine nacelle on high-lift configuration of turboprop airliner. *Journal of Aircraft*, 55(3):1–8, October 2017.

[7] N. Van Arnhem. *Unconventional Propeller-Airframe Integration for Transport Aircraft Configurations*. Ph.D. dissertation, Delft University of Technology, The Netherlands, March 2022.

[8] F. Catalano. On the effects of an installed propeller slipstream on wing aerodynamic characteristics. *Acta Polytechnica*, 44(3):8–14, 01 2004.

[9] R. T. Johnston and J. P. Sullivan. Unsteady wing surface pressures in the wake of a propeller. *Journal of Aircraft*, 30(5):644–651, 1993.

[10] R.R. Duivenvoorden, N. Suard, T. Sinnige, and L.L.M. Veldhuis. Experimental investigation of aerodynamic interactions of a wing with deployed fowler flap under influence of a propeller slipstream. *AIAA AVIATION 2022 Forum, San Diego, California*, July 2022.

[11] A. Stuermer. Unsteady cfd simulations of propeller installation effects. In *42nd AIAA/ASME/SAE/ASEE Joint Propulsion Conference, Sacramento, California*, July 2006.

[12] E.W.M. Roosenboom, A. Stürmer, and A. Schröder. Advanced experimental and numerical validation and analysis of propeller slipstream flows. *Journal of Aircraft*, 47(1):284–291, 2010.

[13] T. Stokkermans, N. van Arnhem, T. Sinnige, and L. Veldhuis. Validation and comparison of rans propeller modeling methods for tip-mounted applications. *AIAA Journal*, 57(2):566–580, February 2019.

[14] J.H. Ferziger and M. Peric. *Computational Methods for Fluid Dynamics*. Springer, Berlin, 3 edition, 2002.

[15] C.L. Rumsey, J.P. Slotnick, M. Long, R.A. Stuever, and T.R. Wayman. Summary of the first aiaa cfd high-lift prediction workshop. *Journal of Aircraft*, 48(6):2068–2079, November 2011.

[16] C.L. Rumsey and J.P. Slotnick. Overview and summary of the second aiaa high lift prediction workshop (invited). *Journal of Aircraft*, 52(4):1006–1025, August 2014.

[17] C.L. Rumsey and J.P. Slotnick. Overview and summary of the third aiaa high lift prediction workshop. *Journal of Aircraft*, 56(2):621–644, March 2019.

[18] LEAP CFD TEAM. 2022, tutorial leap australia: Part 2 – resolving each region of the boundary layer. <*https://www.computationalfluiddynamics.com.au/y-plus_part2_resolving-each-region-of-the-boundary-layer/*>. (accessed: 13.09.2022).

[19] T. Sinnige. Tud-xprop-s performance discription, reference data (internally distributed, unpublished). 2021.

[20] L.M.M. Boermans and P.B. Rutten. Tu delft internal report lsw 95-3, two-dimensional aerodynamic characteristics of airfoil nlf-mod22 with fowler flap. June 1995.

[21] L. Müller, D. Kozulovic, and J. Friedrichs. Unsteady flow simulations of an over-the-wing propeller configuration. *50th AIAA/ASME/SAE/ASEE Joint Propulsion Conference, Cleveland, Ohio*, July 2014.

[22] K. Deere, S. Viken, M. Carter, J. Viken, M. Wiese, and N. Farr. Computational analysis of powered lift augmentation for the leaptech distributed electric propulsion wing. *35th AIAA Applied Aerodynamics Conference, Denver, Colorado*, June 2017.

[23] X. Gou. eflight journal, dlr, airbus, rolls-royce and bauhaus luftfahrt jointly developing 100-seat hybrid-electric aircraft concept, https://news.e-flight-journal.com/?p=591, accessed on 12-9-2023.

[24] E. Roosenboom, A. Heider, and A. Schröder. Propeller slipstream development. *25th IAA Applied Aerodynamics Conference, Miami, Florida*, 1:1–9, June 2007.

[25] E. Roosenboom, A. Heider, and A. Schröder. Comparison of piv measurements with unsteady rans calculations in a propeller slipstream. *27th AIAA Applied Aerodynamics Conference, San Antonio, Texas*, pages 1–13, June 2009.

[26] D. Bongen, M.F. Beckers, M. Schollenberger, D.P. Bergmann, T. Lutz, A. Gothow, M. Saeed, J. Weiss, A. Bardenhagen, and R. Radespiel. Simulation of a distributed propulsion system in a wind tunnel. *AIAA AVIATION 2022 Forum, San Diego, California*, July 2022.

[27] S. Bölk, R. de Vries, N. van Arnhem, and L. Veldhuis. Numerical investigation of propeller–flap interaction in inclined over-the-wing distributed-propulsion systems. *AIAA Scitech 2021 Forum, virtual event*, January 2021.

[28] Nayler, Stedman, and Stern. Experiments on an aerofoil having a hinged rear portion. *British Reports and Memoranda No. 110*, 1914.

[29] A.D. Young. The aerodynamic characteristics of flaps. *British Reports and Memoranda No. 2622*, 1954.

[30] A.M.O. Smith. Stratford's turbulent separation criterion for axially-symmetric flows. *Zeitschrift für angewandte Mathematik und Physik (ZAMP)*, 28(5):929–939, 1977.

[31] B.W. Pomeroy and M.S. Selig. Design of airfoils to mitigate wake bursting. In *55th AIAA Aerospace Sciences Meeting, Grapevine, Texas*, January 2017.

[32] I. Gartshore. Predictions of the blowing required to suppress separation from high-lift aerofoils. In *Meeting on the Prospects for Improvement in Efficiency of Flight, Toronto, Canada*, page 872, 1970.

[33] T.C.A. Stokkermans. *Aerodynamics of Propellers in Interaction Dominated Flowfields: An Application to Novel Aerospace Vehicles*. Ph.D. dissertation, Delft University of Technology, The Netherlands, November 2020.

[34] M.K. Rwigema. Propeller blade element momentum theory with vortex wake deflection. *27th Congress of the International Council of the Aeronautical Sciences 2010, ICAS 2010, Nice, France*, September 2010.

[35] Y. Levy, D. David, and A. Seginer. Graphical visualization of vortical flows by means of helicity. *AIAA*, 28(8):1347–1352, August 1990.

[36] Y. Liu, W. Zhong, and Y. Tang. On the relationships between different vortex identification methods based on local trace criterion. *Physics of Fluids*, 33(10):105–116, October 2021.

[37] H. Himmelskamp. *Profile Investigations on a Rotating Airscrew*. Ph.D. dissertation, Gottingen, Germany, 1945.

[38] J.Goyal, T.Sinnige, F. Avallone, and C. Ferreira. Aerodynamic and aeroacoustic characteristics of an isolated propeller at positive and negative thrust. *AIAA Aviation 2021 Forumn, Virtual Event*, August 2021.

[39] L.L.M. Veldhuis, M. Kotsonis, and E. Berkel. Non-uniform inflow effects on propeller performance. *31st AIAA Applied Aerodynamics Conference, San Diego, California*, June 2013.

[40] D.P. Witkowski, A.K.H Lee, and J.P. Sullivan. Aerodynamic interaction between propellers and wings. *Journal of Aircraft*, 26(9):829–836, 1989.

[41] P. Aref, M. Ghoreyshi, A. Jirasek, M. Satchell, and K. Bergeron. Computational study of propeller–wing aerodynamic interaction. *2018 AIAA Aerospace Sciences Meeting, Kissimmee, Florida*, July 2018.

[42] N.T. Suard. *Improving High Angle of Attack Performance of an Aircraft With Leading Edge Mounted Propellers Through Nacelle and Leading Edge Modification*. MSc. Thesis, Delft University of Technology, The Netherlands, June 2022.

[43] S. Taniguchi and A. Oyama. Numerical analysis of propeller mounting position effects on aerodynamic propeller/wing interaction. *AIAA SCITECH 2022 Forum, San Diego, California*, January 2022.

[44] G.L.O. Halila, A.P. Antunes, Galdino R., and Azevedo J.L.F. Effects of boundary layer transition on the aerodynamic analysis of high-lift systems. *Aerospace Science and Technology*, 90:233–245, 2019.

[45] D. Keller, Y. J. Hasan, and R Rudnik. Nacelle strake design for short takeoff and landing configuration with turboprop engines. *Journal of Aircraft*, 55(6):2444–2453, 2018.

[46] R.E. Kuhn. Semiempirical procedure for estimating lift and drag characteristics of propeller-wing-flap configurations for vertical-and short-take-off-and-landing airplanes. *NASA Momorandum 1-16-59L*, February 1959.

[47] P.D. Pernas. *Effect of Flap Position on Propeller-Wing-Flap Aerodynamic Interaction for Distributed Propulsion Systesms - An experimental approach*. MSc. Thesis, Delft University of Technology, The Netherlands, February 2022.

[48] X. Fei, B. German, and M. Patterson. Exploring the effects of installation geometry in high-lift propeller systems. *AIAA SciTech Forum, Kissimmee, Florida*, January 2018.

[49] M.J.T. Schroijen, L.L.M. Veldhuis, and R. Slingerland. Propeller slipstream investigation using the fokker f27 wind tunnel model with flaps deflected. *26th Congress of the International Council of the Aeronautical Sciences 2008, ICAS 2008, Anchorage, Alaska*, September 2008.

[50] S. De Lucas Bodas, J. Narbona Gonzalez, V. Ossorio Contreras, J.J. Guerra Crespo, D.E. Funes Sebastian, and L.P. Ruiz Calavera. Experimental validation of numerical prediction of wing-propeller aerodynamic interaction. *32th Congress of the International Council of the Aeronautical Sciences 201, ICAS 2021, Montréal, Québec*, September 2021.

[51] C.L. Rumsey and S.X. Ying. Prediction of high lift: review of present cfd capability. *Progress in Aerospace Sciences*, 38(2):145–180, February 2002.

[52] S. Benhamadouche and D. Laurence. Les, coarse les, and transient rans comparisons on the flow across a tube bundle. *International Journal of Heat and Fluid Flow*, 24(4):470–479, August 2003.

[53] F. Moens and P. Gardarein. Numerical simulation of the propeller/wing interactions for transport aircraft. In *19th AIAA Applied Aerodynamics Conference, Anaheim, California*, June 2001.

[54] ANSYS. Ansys fluent documentation, sliding mesh theory. *URL:https://www.afs.enea.it/project/neptunius/docs/fluent/html/th/node37.htm*. (accessed: 12.09.2022).

[55] L. L. M. Veldhuis, T.C.A. Stokkermans, T. Sinnige, and G. Eitelberg. Analysis of swirl recovery vanes for increased propulsive efficiency in tractor propeller aircraft. *30th Congress of the International Council of the Aeronautical Sciences 2016, ICAS 2016, Daejeon, South Korea*, September 2016.

[56] J.A. Ekaterinaris. High-order accurate, low numerical diffusion methods for aerodynamics. *Progress in Aerospace Sciences*, 5(3):192–300, August 2005.

[57] J. W. van der Burg and M. Luehmann. *Simulation of Maximum Lift Using URANS for a High-Lift Transport Configuration*, pages 75–88. Springer Berlin Heidelberg, 2013.

[58] R. Balin and K. Jansen. A comparison of rans, urans, and ddes for high lift systems from hiliftpw-3. *2018 AIAA Aerospace Sciences Meeting, Kissimmee, Florida,*, January.

[59] R. Balin and K. Jansen. Presentation of: A comparison of rans, urans, and ddes for high lift systems from hiliftpw-3. January 2018.

[60] D.C. Wilcox. *Turbulence Modeling for CFD*. DCW Industries, Inc., La Canada, California, 1 edition, November 2006.

[61] ANSYS FLUENT USER SERVICES CENTER. Introductory fluent notes. *<http://www.southampton.ac.uk/ nwb/lectures/GoodPracticeCFD/Articles/Turbulence_Notes _Fluent-v6.3.06.pdf>*. (accessed: 13.09.2022).

[62] R. Amraoui, H. Mghari, M. Obounou, M. Kaddiri, M. Mouqallid, E. Affad, A. Msaad, and D. Garreton. First and second order turbulence modeling for flows with recirculation zone: Validity of gradient transport hypothesis. *Journal of Materials and Environmental Sciences*, 8(3):1103–1115, January 2017.

[63] B. Launder and D.B. Spalding. The numerical computation of turbulent flow computer methods. *Computer Methods in Applied Mechanics and Engineering*, 3(2):269–289, March 1974.

[64] D.C. Wilcox. Reassessment of the scale-determining equation for advanced turbulence models. *AIAA Journal*, 26(11):1299–1310, 1988.

[65] P. Spalart and S. Allmaras. A one-equation turbulence model for aerodynamic flows. *30th AIAA Aerospace Sciences Meeting, Reno, Nevada*, 439, January 1992.

[66] F. R. Menter. Two-equation eddy-viscosity turbulence models for engineering applications. *AIAA Journal*, 32(8):1598–1605, 1994.

[67] M.F. Beckers, M. Schollenberger, T. Lutz, D. Bongen, R. Radespiel, J.L. Florenciano, and D.E. Funes-Sebastian. Cfd investigation of high-lift propeller positions for a distributed propulsion system. *AIAA AVIATION 2022 Forum, San Diego, California*, July 2022.

[68] Nasa langley research center - turbulence modeling resource - the spalart-allmaras turbulence model, https://turbmodels.larc.nasa.gov/spalart.html, accessed on 12-9-2023.

[69] M. Murayama, Y. Yokokawa, and K. Yamamoto. Validation study of cfd analysis for high-lift systems. *25th Congress of the International Council of the Aeronautical Sciences 2006, ICAS 2006, Hamburg, Germany*, September 2006.

[70] F.R. Menter and R. Lechner. *Best Practice: RANS Turbulence Modeling in Ansys CFD*. Ansys Germany GmBH, 2021.

[71] Ansys. *ANSYS Fluent User's Guide*. ANSYS, inc., Canonsburg, PA, 2021 r1 edition.

[72] E. Roosenboom, A. Heider, and A. Schröder. Investigation of the propeller slipstream with particle image velocimetry. *Journal of Aircraft*, 46(2):442–449, March 2009.

[73] T. Alasdair and D. Karthik. Computational investigation of unsteadiness in propeller wake–wing interactions. *Journal of Aircraft*, 50(3):985–988, May 2013.

[74] A.F. Ribeiro, R. Duivenvoorden, and D. Martins. High-fidelity simulations of propeller-wing interactions in high-lift conditions. *AIAA AVIATION 2023 Forum, San Diego, California*, June 2023.

[75] J.B. Barlow, H.R. William, and A. Pope. *Low-Speed Wind Tunnel Testing*. Wiley, 3th edition, 1999.

[76] R. Vos and S. Farokhi. *Introduction to Transonic Aerodynamics*. Springer Dordrecht, 1th edition, 2015.

[77] F. Götten, D. Finger, M. Marino, C. Bil, M. Havermann, and C. Braun. A review of guidelines and best practices for subsonic aerodynamic simulations using rans cfd. *Asia-Pacific International Symposium on Aerospace Technology (APISAT)*, December 2019.

[78] P. Spalart and C. Rumsey. Effective inflow conditions for turbulence models in aerodynamic calculations. *AIAA Journal*, 45(10):2544–2553, Oktober 2007.

[79] C. Abdessemed, A. Bouferrouk, and Y. Yao. Effects of an unsteady morphing wing with seamless side-edge transition on aerodynamic performance. *Energies*, 15(3), 2022.

[80] A. Abdel Gawad. Numerical simulation of the effect of leading-edge tubercles on the flow characteristics around an airfoil. *Proceedings of the ASME 2012 International Mechanical Engineering Congress Exposition, Houston, Texas*, November 2012.

[81] J. P. Eastwood and J. P. Jarrett. Toward designing with three-dimensional bumps for lift/drag improvement and buffet alleviation. *AIAA Journal*, 50(12):2882–2898, 2012.

[82] K. Zore, G. Parkhi, B. Sasanapuri, and A. Varghese. Ansys mosai poly-hexcore mesh for high-lift aircraft configuration. *21th Annual CFD Symposium, Bangalore, India*, August 2019.

[83] Guide for the verification and validation of computational fluid dynamics simulations, aiaa-g-077-1998. 2002.

[84] R.H. Bush, T. Chyczewski, J. Duraisamy, B. Eisfeld, C.L. Rumsey, and B.R. Smith. Recommendations for future efforts in rans modeling and simulations. *AIAA Scitech 2019 Forum, San Diego, California*, January 2019.

[85] R. Vinuesa, P.S. Negi, M. Atzori, A. Hanifi, D.S. Henningson, and P. Schlatter. Turbulent boundary layers around wing sections up to rec=1,000,000. *International Journal of Heat and Fluid Flow*, 72:86–99, 2018.

[86] Y. Maciel, M. Simens, and A. Gungor. Coherent structures in a non-equilibrium large-velocity-defect turbulent boundary layer. *Flow, Turbulence and Combustion*, 98, January 2017.

[87] E. Obert, R. Slingerland, D.J.W. Leusink, T. Van den Berg, and J.H. Koning. *Aerodynamic Design of Transport Aircraft*. Ios Press, Delft, 1th edition, 2009.

[88] F.O. Thomas, R.C. Nelson, and X. Liu. Experimental investigation of the confluent boundary layer of a high-lift system. *AIAA*, 38(6):978–988, 2000.

[89] M.F. Kerho and M.B. Bragg. Airfoil boundary-layer development and transition with large leading-edge roughness. *AIAA*, 35(1):75–84, January 1997.

[90] R. de Vries, N. van Arnhem, T. Sinnige, R. Vos, and L. Veldhuis. Aerodynamic performance of an aircraft equipped with horizontal tail-mounted propeller. *AIAA Aviation Forum, Dallas, Texas*, June 2019.

[91] M. Felli. Underlying mechanisms of propeller wake interaction with a wing. *Journal of Fluid Mechanics*, 908, February 2021.

[92] X. Liu and J. S. Marshall. Blade penetration into a vortex core with and without axial core flow. *Journal of Fluid Mechanics*, 519:81–103, 2004.

[93] C.L. Rumsey, J.P. Slotnick, and C.D. Woeber. Fourth high-lift prediction/third geometry and mesh generation workshops: Overview and summary. *Journal of Aircraft*, 60(4):1160–1177, July 2023.